Computational modeling of photoactive materials and heterointerfaces for solar energy conversion

Alekos Segalina

Université de Lorraine - École doctorale C2MP

Thèse

présentée pour obtenir le grade de

Docteur en Chimie

par

Alekos Segalina

LPCT - Université de Lorraine, Nancy

Computational modeling of photoactive materials and heterointerfaces for solar energy conversion

Membres du Jury:

Rapporteurs :	
David Beljonne,	University of Mons, Mons
Elise Dumont,	École normale supérieure de Lyon, Lyon
Examinateurs :	
Yannick J. Dappe,	SPEC - Université Paris-Saclay, Saclay
Sébastien Lebegue,	LPCT - Université de Lorraine, Nancy
Invité:	
Antonio Monari,	LPCT - Université de Lorraine, Nancy
Directeur de Thèse :	
Mariachiara Pastore,	LPCT - Université de Lorraine, Nancy

Nancy Décembre 17, 2020

The sciences do not try to explain, they hardly even try to interpret, they mainly make models. By a model is meant a mathematical construct which, with the addition of certain verbal interpretations, describes observed phenomena. The justification of such a mathematical construct is solely and precisely that it is expected to work.

JOHN VON NEUMANN

Contents

Acknowledgments

First of all, I would like to warmly thank Mariachiara for her guidance and her support during the development of the thesis. I especially thank you for having enlarged my scientific background, for all the opportunities, for believing in me, and for introducing me to your scientific network. A special thanks also go to Xavier for the valuable discussions and for supervising me in the first part of my PhD. On the same footing, I am sincerely thankful to Antonio Monari, Dario Rocca, Fabrizio Santoro, Giacomo Prampolini, Sébastien Lebegue, and Simone Piccinin, who taught me a lot with a lot of patience and dedication and who I consider as fully-fledged co-directors of this thesis. I am thankful to David Beljonne and Elise Dumont for their role of rapporteurs on the manuscript and to Yannick Dappe, and Sébastien Lebegue for agreeing to be part of the thesis committee. I would like to thank all the PhD students, researchers, professors, and staff members of the LPCT for making me feel an active part of the lab right from the beginning, for never denying me support, and for having enriched my stay in Nancy. I want to thank all my friends, who are certainly too many to list here, and who have contributed to the growth of my person and have helped to keep my enthusiasm and curiosity always alive. In fact, I believe that your support, albeit indirect, has been fundamental to achieve this goal. I am thankful to my present/former roommates with whom I shared good times during my stay in Nancy. Last but not least, I want to thank my whole family, especially my parents and my grandparents, who have always believed in my abilities and have always supported and respected my choices.

Acronyms

1TDM one-particle Transition Density Matrix
ACN Acetonitrile
ACPYPE AnteChamber PYthon Parser interfacE
$\boldsymbol{Ad-MD|gVH}$ Adiabatic Molecular Dynamics generalized Vertical Hessian
AFII type-II Antiferromagnetic Phase
AIMD Ab Initio Molecular Dynamics
AMBER Assisted Model Building with Energy Refinement
ATO Sb-doped SnO_2
B3LYP Becke, 3-parameter, Lee–Yang–Parr
BISp Bremsstrahlung-Isochromat Spectroscopy
BOMD Born-Oppenheimer Molecular Dynamics
C-PCM Conductor-like Polarizable Continuum Model
C343 Coumarin 343
CAM-B3LYP Coulomb-Attenuating Method-Becke, 3-parameter, Lee–Yang–Parr
CAS Complete Active Space
CB Conduction Band
CBM Conduction Band Minimum
CEA-VE Classical Ensemble Average of Vertical Excitations
CHARMM Chemistry at Harvard Macromolecular Mechanics
CL Classical
COSMO Conductor-like Screening Model
CT Charge Transfer
DFT Density Functional Theory
DFT-D Dispersion-Corrected Density Functional Theory
DoF Degrees of Freedom
DOS Density Of States
DSPEC Dye-Sensitized Photoelectrochemical Cell
DSSC Dye-Sensitized Solar Cell
e-ph electron-phonon
EA Electron Affinity
EELS Electron Energy Loss Spectroscopy

EEpc Electronic Embedding point-charges
evGW partially self consistent GW
FCI Full Configuration Interaction
FF Force Field
fwhm full width at half-maximum
GAFF Generalized AMBER Force Field
GGA Generalized Gradient Approximation
GP Gas Phase
GPU Graphics Processing Unit
GS Ground State
GTH Goedecker-Teter-Hutter
gVH Generalized Vertical Hessian
HF Hartree-Fock method
HOMO Highest Occupied Molecular Orbital
HSE Heyd–Scuseria–Ernzerhof
IC Internal Coordinate
IP Ionization Potential
IPES Inverse Photoemission Spectroscopy
KS Kohn Sham
LDA Local Density Approximation
LJ Lennard-Jones
LUMO Lowest Unoccupied Molecular Orbital
M06-2X Minnesota 06, Global hybrid functional with 54% HF exchange
MBPT Many Body Perturbation Theory
MCSCF Multiconfiguration Self-Consistent Field
MD Molecular Dynamics
MM Molecular Mechanics
MPW1K Modified Perdew-Wang exchange function with gradient correction developed to optimize the reaction and activation energies of free radical reactions
MQC Mixed Quantum-Classical
NPT Isothermal–Isobaric
NVT Canonical
OFET Organic Field Effect Transistors

OLED Organic Light Emitting Diode
ONIOM Our own N-layered Integrated molecular Orbital molecular Mechanics
OPLS Optimized Potentials for Liquid Simulations
PAW Projector Augmented Wave Method
PBC Periodic Boundary Conditions
PBE Perdew–Burke-Ernzerhof
PCE Power Conversion Efficiency
PCM Polarizable Continuum Model
PDI Perylene Diimide
PDOS Projected Density Of States
PES Potential Energy Surfaces
PESp Photoemission Spectroscopy
PR Participation Ratio
QM Quantum Mechanics
QM/EE Quantum Mechanics/Electronic Embedding
QM/MM/EE Quantum Mechanics/Molecular Mechanics/Electronic Embedding
QMD-FF Quantum-Mechanically Derived Force Field
qp quasi-particle
r-PBE revised Perdew–Burke-Ernzerhof
RESP Restricted Electrostatic Potential
RMSD Root Mean Square Deviations
RPA Random Phase Approximation
SC Semiconductor
SO Spin-Orbit
TD-DFT Time-Dependent Density Functional Theory
TDA Tamm-Dancoff Approximation
TheoDORE Theoretical Density, Orbital Relaxation and Exciton analysis
TIP3P Transferable Intermolecular Potential with 3 Points
UPS Ultraviolet Photoelectron Spectroscopy
VB Valence Band
VBM Valence Band Maximum
VH Vertical Hessian
XAS X-Ray Absorption

XES X-Ray Emission

List of publications

- **Computational Modeling of Exciton Localization in Self-Assembled Perylene Helices: Effects of Thermal Motion and Aggregate Size** A. Segalina, X. Assfeld, A. Monari and M. Pastore, J. Phys. Chem. C. **2019**, 123, 6427–6437.

- **Accounting for vibronic features through a mixed quantum-classical scheme: structure, dynamics and absorption spectrum of a perylene diimide dye in solution** A. Segalina, J. Cerezo, G. Prampolini, F. Santoro and M. Pastore, J. Chem. Theory Comput. **2020**, 10.1021/acs.jctc.0c00919.

- **Structure and Energetics of Dye-Sensitized NiO Interfaces in Water from AIMD and GW Calculations** A. Segalina, S. Lebegue, D. Rocca, S. Piccinin and M. Pastore, In preparation

Other works:

- **Conical intersection properties unraveled by the position spread tensor** A. Segalina, A. Francés-Monerris, M. Pastore, T. Leininger, S. Evangelisti and A. Monari, Theor. Chem. Acc. **2018**, 137, 163.

- **Dynamical and Environmental Effects on the Optical Properties of an Heteroleptic Ru(II)–Polypyridine Complex: A Multilevel Approach Combining Accurate Ground and Excited State QM-Derived Force Fields, MD and TD-DFT** G. Prampolini, F. Ingrosso, A. Segalina, S. Caramori, P. Foggi and M. Pastore, J. Chem. Theory Comput. **2019**, 15, 529–545.

Abstract

In this thesis we have dealt with the computational modeling of materials and molecular systems that are used in dye-sensitized solar cells (DSSCs) and dye-sensitized photoelectrosynthetic cells (DSPECs). In particular, we have addressed the study of the elements composing these devices, i.e. dyes, semiconductors and interfaces, by means of computational chemistry techniques, paying special attention to the modeling of the dynamical, optical and electronic structure properties. The complexity of the systems and the physical processes involved requires the combined use of different theoretical methodologies, as detailed below. A perylene diimide (PDI) dye in solution has been investigated by combining Density Functional Theory based methods and classical molecular dynamics (MD) simulations. In particular, we focused on the excited state properties of its aggregates and on the simulation of its electronic absorption spectrum by taking into account vibronic effects. In this context, to have a reliable description of the potential energy surface we made use of a specifically parameterized Quantum-Mechanically Derived Force Field (QMD-FF). Regarding the semiconductors, we have studied different phases of WO_3, that is an n-type semiconductor, using methods based on the Green's Functions in order to rationalize the role of the crystal lattice distortion on the band structure and on the electronic and optical properties. Lastly, we have studied a simplified, albeit realistic model, of a dye-sensitized NiO interface (C343@NiO(100)) by combining ab initio molecular dynamic (AIMD) and GW calculations to describe the role of thermal effects and of the environmental solvent molecules on the interfacial energy-level alignment.

Résumé

Dans cette thése, nous avons traité de la modélisation computationnelle des matériaux et des systèmes moléculaires utilisés dans les cellules solaires à colorant (DSSC) et les cellules photoélectrosynthétiques à colorant (DSPEC). En particulier, nous avons abordé l'étude des éléments composant ces dispositifs, à savoir les colorants, les semi-conducteurs et les interfaces au moyen de techniques de chimie computationnelle en accordant une attention particulière à la modélisation des propriétés de la structure dynamique, optique et électronique. La complexité des systèmes et des processus physiques impliqués nécessite la combinaison de différentes méthodologies théoriques, comme détaillé ci-dessous. Un diimide de pérylène (PDI) en solution a été étudié en combinant des méthodes basées sur la théorie de la fonctionnelle de la densité et des simulations de dynamique moléculaire (MD) classiques. En particulier, nous nous sommes concentrés sur les propriétés d'état excité de ses agrégats et sur la simulation de son spectre d'absorption électronique en prenant en compte les effets vibroniques. Dans ce contexte, pour avoir une description fiable de la surface d'énergie potentielle, nous avons utilisé un champ de force dérivé quantique-mécanique (QMD-FF) spécifiquement paramétré. Concernant les semi-conducteurs, nous avons étudié différentes phases de WO_3, c'est-à-dire un semi-conducteur de type n, en utilisant des méthodes basées sur les fonctions de Green afin de rationaliser le rôle de la distorsion du réseau cristallin sur la structure de bande et sur les propriétés électroniques et optiques. Enfin, nous avons étudié un modèle simplifié, quoique réaliste, d'une interface NiO sensibilisée aux colorants (C343@NiO(100)) en combinant des calculs de dynamique moléculaire ab initio (AIMD) et de GW pour décrire le rôle des effets thermiques et des molécules du solvant environnemental sur l'alignement interfacial du niveau d'énergie.

Introduction

The world in which we live in is characterized by an incessant technological advance that affects every aspect of our society. The progress made in computer science, in transport and in medicine promoted, in fact, a radical change in our life. This progress, however, required an enormous amount of energy and non-renewable resources. As a matter of fact, in line with the technological progress, the consumption and the production of energy is constantly growing, favoring, among other things, many diseases and climate change.[1, 2] However, the energy production coming from renewable sources is also constantly growing and is now accounting for about 10% of the global energy requirement.[1] Among renewable energy sources, solar energy is one of the most fascinating, promising and exploited ones. In fact, about 14900 PW of solar power is in principle available for photovoltaics every year.[3] It follows that, if only 1% of this power being converted into consumable energy, it would meet the whole global energy demand.[3] In this field, most widespread devices still rely on silicon-based solar panels. These devices, though having rather high efficiencies, are based on pure monocrystalline silicon whose production requires an enormous amount of energy and is not free from environmental impacts.[4] On the other hand, last decades have been marked by an exceptional development in this field leading to the development of alternative solar energy conversion devices like for instance, Dye-Sensitized Solar Cell (DSSCs),[5] perovskite solar cells[6] and Dye-Sensitized Photoelectrochemical Cell (DSPECs)[7, 8] which make use of hybrid organic-inorganic materials. The research in this field is thriving more than ever and aims at reach or even surpass the performances of silicon-based solar cells, at the same time, decreasing the cost and the environmental impact linked to production of this type of devices. However, despite substantial efforts, these devices are often plagued by low efficiency, due to competitive recombination processes and by stability issues, leaving plenty of room for investigation, understanding and optimization. The design of new optimized materials and molecular systems to be used in solar energy conversion devices involves both experimental and theoretical scientists. Indeed, the

complex structure and functioning of these devices is often undetectable by solely experimental techniques. On the other hand, the theoretical and computational methods based on Quantum Mechanics and Molecular Mechanics may help to unravel the mechanisms governing the functioning. The computational modeling of such systems is however far from trivial. The complexity of the molecular and solid-state systems and the physical processes involved require the combined use of different theoretical methods. In this thesis, we address the study of the elements composing DSSCs and DSPECs, namely dyes, semiconductors and interfaces by means of computational chemistry techniques paying special attention to the modeling of the optical and electronic structure properties. In particular, we studied the Ground States and Excited States properties of dyes, semiconductors and of dye/semiconductor interfaces including also dynamical and environmental effects in their description.

The outline of the thesis is as follows. In Chapter 1 we present an overview of the theoretical methods that we use in our works to describe molecular and solid state systems both in the ground and in the excited state. Chapter 2 describes the work on Perylene Diimides dyes for which we modeled the excited state properties for both the monomeric and the aggregated form accounting for dynamical, solvent, excitonic, and vibronic effects. In Chapter 3 we address the study of a dye-sensitized NiO interface in water solution, for which we analyzed the role of finite temperature effects and electronic correlation effects on the interfacial energetics. Finally, Chapter 4 reports the work on semiconductors, in particular, we describe, by considering different crystal phases, the role of crystal lattice distortions on optical and electronic structure properties of WO_3.

Bibliography

[1] I. E. Agency, Key World Energy Statistics 2019, **2019**, p. 81.

[2] L. Curtis, W. Rea, P. Smith-Willis, E. Fenyves, Y. Pan, *Environ. Int.* **2006**, *32*, 815–830.

[3] M. Z. Jacobson, *Energy Environ. Sci.* **2009**, *2*, 148–173.

[4] D. Turney, V. Fthenakis, *Renew. Sust. Energ. Rev.* **2011**, *15*, 3261–3270.

[5] B. O'Regan, M. Grätzel, *Nature* **1991**, *353*, 737–740.

[6] W.-J. Yin, J.-H. Yang, J. Kang, Y. Yan, S.-H. Wei, *J. Mater. Chem. A* **2015**, *3*, 8926–8942.

[7] M. Pastore, F. De Angelis, *J. Am. Chem. Soc.* **2015**, *137*, 5798–5809.

[8] W. J. Youngblood, S.-H. A. Lee, Y. Kobayashi, E. A. Hernandez-Pagan, P. G. Hoertz, T. A. Moore, A. L. Moore, D. Gust, T. E. Mallouk, *J. Am. Chem. Soc.* **2009**, *131*, 926–927.

Chapter 1
Theoretical Frameworks

During the last decades, the extraordinary development in computer hardware and algorithms has elevated computational and theoretical chemistry methods to a predictive tool regularly applied to condensed matter physics and chemistry. In fact, the synergy between computational modeling and experiments has been shown to be crucial to improve the fundamental comprehension behind the physical phenomena at work to then use this knowledge for the development of new optimized materials, nanostructures, drugs etc.[1] Unfortunately, the complexity of the systems and phenomena under investigation often requires merging and applying different computational approaches and techniques developed to investigate different physical properties of the matter. For example, finite temperature effects are accounted for by means of ab initio or classical Molecular Dynamics (MD) simulations depending on the size of the system and timescale of the process under investigation.

Electronic properties of Ground and Excited States are investigated by means electronic structure methods. As for the MD, the accuracy and the choice of the method depend on the size of the investigated system. If on one hand, Density Functional Theory can handle big molecular systems it is sometimes inaccurate, e.g. in the case of charge transfer Excited States, problems of a clear multireference nature or systems characterized by strong Van der Waals interactions.[2–5] On the other hand, more refined wave function based methods and Green's function approaches are still limited to the study of smaller systems.

All these methods can be formulated to handle either periodic systems through the use of Periodic Boundary Conditions (PBCs) or isolated systems. In this thesis, we will deal with both isolated molecular systems and periodic condensed matter systems making use of both MD simulations and electronic structure methods. In fact, we have made extensive use of combined approaches demonstrating the necessity to merge various theoretical methods in order to capture different physical effects that together describe complex physical processes. In this Chapter we will discuss the main concepts, potentials and limitations of the theoretical methodologies used throughout this work.

1.1 Born-Oppenheimer approximation

Quantum chemistry is a powerful tool for the theoretical study of chemical systems. It aims, in principle, to solve the Schrödinger equation that remains analytically unsolvable for many electron systems. For a given molecule the time independent non-relativistic Schrödinger equation provides all possible energies and stationary states:[6, 7]

$$\hat{H}|\Psi_{(x,Q)}\rangle = E_{tot}|\Psi_{(x,Q)}\rangle \tag{1.1}$$

In equation 1.1 $\hat{H}$ is the Hamiltonian operator and $\Psi_{(x,Q)}$ is the wave function, where the nuclear and electronic coordinates are indicated collectively with Q and x, respectively. The Hamiltonian within the coulombic approximation reads:

$$\hat{H} = \hat{T}_n + \hat{T}_e + \hat{V}_{en} + \hat{V}_{nn} + \hat{V}_{ee} \tag{1.2}$$

and the elements in Eq 1.2 are defined as follows:

$$\begin{aligned}
\hat{T}_e &= \sum_i \frac{p_i^2}{2m} \\
\hat{T}_n &= \sum_\alpha \frac{p_\alpha^2}{2M_\alpha} \\
\hat{V}_{ee} &= \sum_{i<j} \frac{e^2}{r_{ij}} \\
\hat{V}_{nn} &= \sum_{\alpha<\beta} \frac{Z_\alpha Z_\beta e^2}{r_{\alpha\beta}} \\
\hat{V}_{en} &= -\sum_i \sum_\alpha \frac{Z_\alpha e^2}{r_{i\alpha}}
\end{aligned} \tag{1.3}$$

here the index i refers to the electrons (e), α to the nuclei (n) and Z_α is the nuclear charge of nucleus α. The first two terms in Eq. 1.2 are the kinetic energy of the electrons and the kinetic energy of the nuclei, respectively; the last three terms are the potential energy between the electrons, between the nuclei and between the electron and the nuclei, respectively.[6]

One key concept underlying the description of the quantum states of molecules is

the Born-Oppenheimer approximation.[8] This approximation permits to decouple the motion of the nuclei and the motion of the electrons due to the big difference between electronic and nuclear masses $\left(m_n \approx\ 1840 m_e\right)$. The above consideration allows one to define the electronic Hamiltonian as:

$$\hat{H}_e = \hat{T}_e + \hat{V}_{en} + \hat{V}_{ee} + \hat{V}_{nn} \tag{1.4}$$

where the kinetic energy of the nuclei is absent. Born and Oppenheimer then approximated the wave function as a product of the nuclear wave function and the electronic wave function.

$$|\Psi_{tot}\rangle \approx \chi_{(Q)}\Psi_{(x;Q)} \tag{1.5}$$

Applying the electronic Hamiltonian to the wave function in Eq. 1.5 one has:

$$\hat{H}_e\Psi_{(x;Q)} = E_e(Q)\Psi_{(x;Q)} \tag{1.6}$$

In Eq. 1.6 the nuclear wave function can be elided because in H_e the terms containing derivatives with respect to the nuclear coordinates are absent. However, one can note that nuclear coordinates are still present in the electronic wave function and also in the electronic energy but they are in the form of parameters (multiplicative variables). The application of the Hamiltonian, in the form of $\hat{H} = \hat{H}_e + \hat{T}_n$, to the wave function in Eq 1.5 gives:

$$\begin{aligned} \left(\hat{H}_e + \hat{T}_n\right)\chi_{(Q)}\Psi_{(x;Q)} &= E\chi_{(Q)}\Psi_{(x;Q)} \\ \left(E_e(Q) + \hat{T}_n\right)\chi_{(Q)} &= E\chi_{(Q)} \end{aligned} \tag{1.7}$$

where the last expression in Eq.1.7 is the Schrödinger equation for the nuclei and states that $\chi_{(Q)}$ is eigenfunction of the operator $\left(E_e(Q) + \hat{T}_n\right)$ where $E_e(Q)$ here plays the role of a potential energy.

The Born-Oppenheimer approximation represents a keystone in quantum chemistry and is valid for modeling most of physical and chemical phenomena that occur in molecular systems; however, in many other important cases this approximation breaks down. As a matter of fact, polyatomic molecules possessing potential energy surfaces that are nearly-degenerate or degenerate for specific nuclear coordinates

give rise to Conical Intersections.[9] In these regions the non-adiabatic couplings are not negligible and consequently the Born–Oppenheimer approximation does not hold anymore. Conical intersections hence provide pathways for important non-adiabatic photochemical process named internal conversions.[10] Moreover, the coupling terms between the electronic and vibrational quantum states are also fundamental to simulate the absorption spectra of some molecules that present a well-resolved vibronic structure. The couplings describing the so called vibronic effects in some molecular systems dominate the band shapes and cannot be neglected.[11, 12] These effects will be described in detail in Chapter 2 where we will tackle the problem of the calculation of the perylene's absorption spectra with its vibronic progression.

1.2 Electronic structure methods

In this Section we discuss the main concepts of the methods used to investigate the electronic structure. The electronic structure methods can be grouped in two main categories: the wavefunction methods and the Density Functional Theory (DFT) methods and in both cases these are here discussed within the Born-Oppenheimer approximation.

The wavefunction methods are based on different approximations aimed at simplifying the Schrödinger equation, but, their applicability to big molecular systems is still limited. Indeed, the solutions of the time-independent Schrödinger equation, i.e., the eigenfunctions, are functions of the electron coordinates (3N-dimensions), which therefore increase rapidly with the increase of the size of molecular systems. On the other hand, to handle with larger and more realistic systems, Density Functional Theory (DFT) based methods are the most appropriate choice. This approach, based on the electron density instead on the wavefunction, reduces the 3N-dimensional problem, represented by the solution of the Schrödinger equation, to a 3-dimensional one.[13–15] DFT methods are very popular in solid state physics, where the electronic structure of crystals is investigated making use of Bloch wavefunctions and then making use of Periodic Boundary Conditions (Born-von Karman).[16] Furthermore, unlike the isolated molecular systems, which make

use of all-electron approach and localized basis set, periodic crystal systems generally rely on plane wave basis set and make use of pseudopotentials.[17–19] The combined use of pseudopotentials and plane wave basis set is necessary for different reasons but it is mainly related to the need to decrease the computational cost. As a matter of fact, the systems investigated in solid state physics are often composed of heavy atoms, e.g. transition metals, and therefore hold a large number of electrons. The use of pseudopotential thus permits to consider the core electrons as frozen and to account for them only via an effective potential (pseudopotential). Moreover, this approach not only reduces the electronic degrees of freedom but also the number of plane waves necessary to converge the electronic properties. Indeed, the core states, that are no longer explicitly calculated, have a localized nature and would require an huge number of plane waves to be properly described.[16–19]

A Subsection for both DFT methods and Wavefunction methods is given below, where we try to elucidate the main concepts at the basis of these approaches. An alternative formulation to study of the electronic structure of solids and molecules is based on many body perturbation theory within the Green's function formalism and this will be discuss in Subsection 1.2.3.

1.2.1 Wavefunction methods

The electronic wave function for a many-electron system can be expressed by the product of monoelectronic wave functions (spin-orbitals). However, this product must satisfy the Pauli exclusion principle, for which two particle cannot occupy the same quantum state, and the antisymmetry principle for fermions. The latter states that the electronic wave function must change in sign when an even number of transpositions of the spin coordinates of the electrons are made:

$$\Psi_n\big(1,2,\ldots,i,\ldots,j,\ldots,n\big) = -\Psi_n\big(1,2,\ldots,j,\ldots,i,\ldots,n\big) \tag{1.8}$$

Following these principles, it is possible to write the product of spin-orbitals into

a determinant form, i.e. the so-called Slater determinant:

$$\Phi(1,2,...,n) = \frac{1}{\sqrt{n!}} \begin{bmatrix} \psi_{k1}(1) & \psi_{k2}(1) & \dots & \psi_{kn}(1) \\ \psi_{k1}(2) & \psi_{k2}(2) & \dots & \psi_{kn}(2) \\ \vdots & \vdots & \ddots & \vdots \\ \psi_{k1}(n) & \psi_{k2}(n) & \dots & \psi_{kn}(n) \end{bmatrix} \tag{1.9}$$

where n is the number of electron and the ψ_{ki} is the i^{th} spin-orbital. The Slater determinant represents a single electronic configuration, namely a possible way of distributing the electrons over the spin-orbitals. However, a many-electron system is often poorly described by a single electronic configuration. To improve the wave function description one should take into account for several electronic configurations. In fact, it is always possible to expand Ψ_n over a complete set of n electron functions which satisfy the Pauli exclusion principle and the antisymmetry principle, e.g. a complete set of Slater determinants. The wave function expanded over a complete set of Slater determinants is expressed as a linear combination of Slater determinants.

The simplest approximation to the electronic wave function is known as the Hartree-Fock method (HF), developed in the late 1920s: the electronic wavefunction is expressed as a single Slater determinant, with the electrons treated as independent particles moving in the mean field generated by the other N-1 particles.[6] HF is based on a set of non-linear single-particle equations (canonical Hartree–Fock equations):

$$(\hat{h}(\mathbf{r_1}) + \hat{J}(\mathbf{r_1}) - \hat{K}(\mathbf{r_1}))\phi(\mathbf{r_1})_{HF} = \epsilon_{HF}\phi(\mathbf{r_1})_{HF} \tag{1.10}$$

where the $\phi(\mathbf{r_1})_{HF}$ and ϵ_{HF} are the single particle HF orbitals and energies respectively, the $\hat{h}(\mathbf{r_1})$ term bears the kinetic energy operator and the nuclei-electrons interaction, and the $\hat{J}(\mathbf{r_1})$ and $\hat{K}(\mathbf{r_1})$ terms are the so-called Coulombic and Exchange operator respectively. Since, the Coulombic and the Exchange operators depend explicitly on the HF orbitals, these equations must be solved iteratively (self-consistently). The solution of the HF equations provides the best approximation to the wavefunction of the electronic Ground State into single Slater determinant form.[6, 7] The HF method, however, is not able to properly treats

the electron-electron interactions, namely, it does not account for the correlation effects.

The electronic correlation is usually partitioned in static, arising from the presence of degenerate or quasi-degenerate electronic configurations, and dynamic that is more strictly related to the correlated motions of the electrons and the short distance electron-electron repulsion.[4, 20] This classification provides, however, a too simplified picture, since a very poor description of dynamic correlation effects can induce an unphysical near degeneracy between different electronic configurations. One possible strategy to account for all these effects is represented by the Full Configuration Interaction (FCI) method, where the electronic wavefunction is expanded over all possible Slater determinants which can be constructed from a given orbital basis set. However, this method can only be applied to small systems due to its tremendous computational cost.[21, 22]

An intermediate approach between HF and FCI methods is represented by the Multiconfiguration Self-Consistent Field (MCSCF) method which aims at performing a FCI expansion only for a limited number of electronic configurations, optimizing self consistently both the coefficients of the expansion and the orbitals.[7] As a matter of fact, accounting for many electronic configurations is essential to describe the formation or the breaking of bonds, Conical Intersections or other process which are inherently multi configurationals.[23]

In the MCSCF method one should establish, based on physical considerations, which are the configurations to include in the wavefunction expansion. One of the most popular approaches is represented by the Complete Active Space (CAS) method, where the spin-orbitals are divided in three categories:

- Core spin orbitals that are all occupied.
- Active spin orbitals, which have all the possible occupation.
- Virtual spin orbitals which are always not occupied.

Thus, considering the space spanned by the determinants generated by distributing the active electrons among the active orbitals, and optimizing simultaneously orbitals and coefficients, gives the CASSCF wavefunction and energies.[24] However, also the CASSCF remains applicable only to relative small systems; the limit

for CASSCF calculation is in fact 20 active electrons in 20 orbitals as shown in a recent publication.[21] Since the CASSCF variational space, as stated, is usually rather limited, only a negligible fraction of electronic (dynamical) correlation is retrieved, being definitely inadequate, for example, for accurate calculations of the electronic excitation energies. Thus, perturbative corrections on the CASSCF wavefunction, are usually employed, making use of multireference perturbation methods.[24–26]

Different correlated wavefunction based methods, however, have been developed, but a review of these methods is beyond our scope here and can be found elsewhere.[4, 27, 28]

1.2.2 DFT methods

The DFT is an exact theory relying on the Hohenberg and Khon theorems that prove the one-to-one correspondence between the GS electron density distribution ($\rho(r)$) of a many electron system and an external potential $V_{ext}(r)$.[13] Being possible to derive all the electronic properties directly from the $\rho(r)$, by applying the variational principle and with a suitable functional, one can obtain the GS total energy of an electronic systems just knowing its electronic density.[13, 15] Though, the original DFT formulation was orbital free the most common applications of DFT are based on its orbital formulation[14] that gives rise to the well known Khon Sham (KS) equations:

$$\begin{aligned} \big[-\frac{1}{2}\nabla^2 + V_{KS}(r)\big]\phi_i^{KS} &= \epsilon_i^{KS}\phi_i^{KS} \\ V_{KS}\big(r\big) &= \int dr^{'}\,\frac{\rho\big(r^{'}\big)}{r-r^{'}} + V_{xc}[\rho](r) + V_{ext}(r) \end{aligned} \tag{1.11}$$

where the integral is the Hartree potential, the $V_{ext}(r)$ represents the electron-nuclei interaction and the $V_{xc}[\rho](r)$ the exchange-correlation potential. These equations differ from the HF ones only for the presence of the $V_{xc}[\rho](r)$ term incorporating all the exchange-correlation effects, and, as for the HF case, they form a set of non-linear single-particle equations that must be solved self-consistently. It is important to stress out that, although the KS theory is based on a set of single particle

equations, this is an exact theory, as the original formulation based on Hohenberg and Khon theorems, and its only limits consists in the necessary approximations of the $V_{xc}[\rho](r)$ term.[13, 14] In this regard, many approximations have been formulated in the last decades (figure 1.1) varying from the simplest Local Density Approximation (LDA),[14] that treats the $V_{xc}[\rho](r)$ operator as local, to the Generalized Gradient Approximation (GGA),[29, 30] where the functional relies on both the electron density and its gradient, to the more recent hybrid functionals, which includes a certain percentages of the non-local HF exchange.[30]

Although in solid state physics the LDA and the GGA functionals are commonly employed in predicting GS properties (e.g. crystal structure), these are often inadequate to treat the electronic structure of the molecules, especially for the Excited States, for which the hybrid functionals are generally preferred. Among the hybrid functional methods, one of the most common ones is the B3LYP functional[30] that includes a 20% of exact Hartree Fock exchange, even if it often shows poor performance in describing the Rydberg and the Charge Transfer (CT) states.[2, 3] In order to correct the hybrid functional drawback in the description of CT states, it is possible to increase the percentage of Hartree Fock exchange and many functionals have been developed within this framework.[31] Another possible strategy to deal with CT states, is represented by the range separated functionals, which use a different percentage of the Hartree Fock exchange according to the electron-electron distance. Within this context, the long range-corrected hybrid functionals, e.g. CAM-B3LYP, are particularly accurate for the description of CT states, which make use of a higher Hartree Fock exchange percentage for the long range electron-electron interaction compared to the short distance one.[32, 33] This approach helps to fix the DFT drawback in the description of CT states that is usually ascribed to the incorrect exchange-correlation potential ($V_{xc}[\rho](r)$) asymptotic behaviour, resulting in a "badly underestimated"[34] long-range charge transfer energy.

Hybrid functionals, however, are still underutilized in the solid state physics. The reasons for this are twofold: i) the high computational cost involved in the evaluation of the long-range exchange functional with plane wave basis set; ii) the exchange interaction at large interelectronic distance are attenuated by correlation effects of the condensed matter.[35–37] However, functionals using the above

discussed range separated exchange term have been developed in order to solve these issues. In solid state calculations, the range separated functionals, make use of a Hartree Fock exchange term that goes rapidly to zero at large interelectronic distance. Even though the range separated functionals based methods reduce the computational cost linked to the evaluation of the Hartree Fock exchange term, they remain extremely costly compared to LDA or GGA approaches.[38] Thus, a very popular and cheap approach is correcting LDA or GGA by accounting for the correlation effects of the most localized electrons (strongly correlated), with the so-called "+U" term.[39, 40] This method, developed from the Hubbard model, enforces the intra-atomic Coulomb interaction on selected atom-like orbitals (e.g. d orbitals and f orbitals) with an additional U_{eff} term that represent the strength of this correction. The U_{eff} term, that is equal to the difference between the intra-atomic Coulomb and exchange (U-J), can be extracted from ab-initio calculations, but usually is fitted against experimental data.[39] Even though DFT+U approach may be less accurate compared to the aforementioned hybrid approaches, this turns out to be a good compromise between the computational cost and the quality of the electronic structure for the strong-correlated materials.[41]

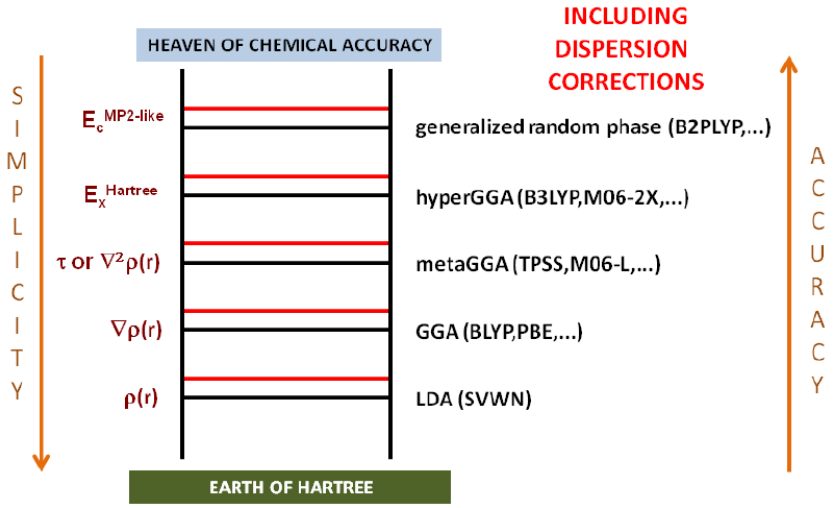

Figure 1.1: Jacob's ladder of density functionals

Time-Dependent extension of Density Functional Theory (TD-DFT), which is an formally exact approach to the time-dependent many-body problem, is widely

used to calculate the excitation energies.[42] The TD-DFT relies on the Runge-Gross theorem, being the time-dependent analogue of the Hohenberg and Khon theorem, Runge and Gross prove the one-to-one correspondence between the time-dependent external potential, $v(r,t)$, and the time-dependent electron density, $\rho(r,t)$, for a many electron system evolving from a fixed initial state.[43] In most cases, TD-DFT, is applied in the context of the linear response theory, where the excitation energies are obtained as the poles of the linear response function.[34] Considering the electron-hole representation (Casida's approach), still within the linear response theory, the excitation energies (ω) are the solutions of the non-Hermitian eigenvalue problem:[34, 44]

$$\begin{bmatrix} \mathbf{A} & \mathbf{B} \\ \mathbf{B}^* & \mathbf{A}^* \end{bmatrix} \begin{bmatrix} \mathbf{X} \\ \mathbf{Y} \end{bmatrix} = \omega \begin{bmatrix} 1 & 0 \\ 0 & -1 \end{bmatrix} \begin{bmatrix} \mathbf{X} \\ \mathbf{Y} \end{bmatrix} \tag{1.12}$$

and the elements of the **A** and **B** matrices are:

$$\begin{aligned} A_{iajb} &= \delta_{ij}\delta_{ab}(\epsilon_a - \epsilon_i) + \big(ia|f_h + f_{ex}|jb\big) \\ B_{iajb} &= \big(ia|f_h + f_{ex}|bj\big) \end{aligned} \tag{1.13}$$

where ϵ_a, ϵ_i are the KS energies and the two particle integrals, written in chemical notation ($\big(ia|f_h + f_{ex}|jb\big)$) represent the expectation value of the Hartree potential and the time-dependent exchange-correlation kernel that, as for the DFT case, must be approximated. The advent of TD-DFT in Quantum Chemistry allowed to handle big molecular systems that remains unaffordable with the wavefunction methods, however, in some cases, TD-DFT is still too expansive and many efforts have been done in order to reduce its computational cost.[45, 46] For example, within the Casida approach, the Tamm-Dancoff Approximation (TDA) enforces the Hermiticity of equation 1.12 by imposing the **B** matrices equal to 0;[46] and this approximation, in many cases, leads to results of comparable accuracy and, sometimes even higher, with respect to full TD-DFT calculations.[47]

1.2.3 Green's function based methods

The application of TD-DFT to solid state systems is rather limited since in the most common implementations it deals only with LDA and GGA functionals which perform rather poorly in the case of Semiconductors and insulators.[45, 48] As a matter of fact, however, TD-DFT implementations combined with hybrid functional even if still limited, have been recently reported.[49, 50]

On the other hand, Excited State properties of these systems can be modeled by Many Body Perturbation Theory (MBPT) and the Green's function formalism.[51] In particular, the one-particle Green's function is used to calculate the photoemission and inverse photoemission processes, whereas, the two-particle Green's function is employed for the optical absorption spectra.[52]

The one-particle Green's function can be interpreted as a dynamical one-particle density matrix and is defined as:

$$G^1(1,2) = -i\langle N|\hat{T}\hat{\psi}(1)\hat{\psi}^\dagger(2)|N\rangle \tag{1.14}$$

where N is the normalized many-body GS wavefunction, 1 and 2 are the shorthand notations for the position (r) and time (t), $\hat{\psi}$ and $\hat{\psi}^\dagger$ represent, respectively, the annihilation and creation field operators within the Heisenberg notation and $\hat{T}$ is the Wick's time-ordering operator. In 1.14, if $t1 > t2$ the one-particle Green's function describes the probability to find an electron in position-time 1 when an electron was added at 2. Conversely, when $t1 < t2$, the one-particle Green's function describe the probability to find a hole in 2 when an electron has been removed in 1.[52] Key concepts in one-particle Green's function theory are the quasiparticles, that can be interpreted as elementary excitations behaving like particles, and the self-energy operator that include all the correlation effects.

The fundamental equation that allows us to calculate the interacting Green's function, given a good approximation of self-energy, is the so-called Dyson equation:[4, 51]

$$G^1(1,2) = G_0^1(1,2) + \int G_0^1(1,3)\Sigma(3,4)G^1(4,2)d(34) \tag{1.15}$$

where the Green's function with the subscript zero represent the non-interacting Green's function and the Σ the self-energy. Hence, it is possible to recast equation 1.15 into a set of single-particle eigenvalue equations, by exploiting the so-called Lehmann representation of the Green's function.[52] Therefore, after introducing the independent single particle hamiltonian as $\hat{H}^{ind} = -\frac{1}{2}\nabla^2 + \hat{V_{ext}} + \hat{V_H}$ the Dyson equation reads:

$$\hat{H}^{ind}(r_1)\phi(r_1) + \int dr_2 \Sigma(r_1, r_2, \epsilon)\phi(r_2) = \epsilon\phi(r_1) \tag{1.16}$$

where the $\phi(r_1)$ and the ϵ are the quasiparticle orbitals and energies, respectively.

However, in spite of the appearance of single-particle form in equation 1.16, the solution of the Dyson equation is far from trivial. In fact, the self-energy is a non-Hermitian and non-local operator that depends on the quasiparticle's ϵ and, as a result, equation 1.16 must be solved self-consistently. Moreover, the exact form of the self-energy, as the exact form of the $V_{xc}[\rho](r)$ within the DFT approach, is unknown, thus, it must be approximated.[53] For example, if one consider the exchange self-energy in 1.16 the HF equations are recovered. On the other hand, the most common approach to treat the self-energy arises from Hedin's GW approximation that introduces the dynamically screened potential W, which describes the Coulomb potential attenuated by all the other electrons in the system.[54] Hence, considering the first-order perturbative expansion in power of W, the self-energy within the GW picture reads:

$$\Sigma(1,2) = iG^1(1,2)W(1,2) \tag{1.17}$$

Within the GW approximation, equations 1.15-1.16 have a simplified form but still, they must be solved self-consistently because both the $G^1(1,2)$ and the $W(1,2)$ terms depend explicitly on the quasiparticle energies and orbitals. However, in practical applications the GW calculations are carried out by approximating the Green's function and the GW self-energy using the KS orbitals and energies.[55] Also, in many cases the self-consistent procedure is avoided and only a single-shot GW calculation (G_0W_0) is performed.[55] For the former approach the choice of the functional turns out to be crucial because the quality of the quasiparticle energies

depend heavily on the DFT starting point.[56]

As pointed out above, the single-particle Green's functions are used to model the charged electronic excitations, as the quasi-particle energies are directly linked to the photoemission and inverse photoemission processes. On the other hand, to model the optical absorption spectra, where two particles are involved one must consider the two-particle Green's function:[57]

$$G^2(1,2;1^{'},2^{'}) = -\langle N|\hat{T}\hat{\psi}(1)\hat{\psi}(2)\hat{\psi}^{\dagger}(2^{'})\hat{\psi}^{\dagger}(1^{'})|N\rangle \tag{1.18}$$

that, similarly to the single-particle case, can be interpreted as the propagation of two quasiparticles (e.g. an electron-hole pair) at the same time.

$$\begin{aligned} L(1,2;1^{'},2^{'}) &= -G^2(1,2;1^{'},2^{'}) + G^1(1,1^{'})G^1(2,2^{'}) \\ L_0(1,2;1^{'},2^{'}) &= G^1(1,1^{'})G^1(2,2^{'}) \end{aligned} \tag{1.19}$$

To compute the optical absorption spectra let us introduce the two-particle correlation function (equation 1.19), defining L_0 as the time-evolution of two independent quasiparticles, which satisfies the following Bethe-Salpeter equation (BSE):[51, 57]

$$L(1,2;1^{'},2^{'}) = L_0(1,2;1^{'},2^{'}) + \int d(3456)L_0(1,4;1^{'},3)\Xi(3,5;4,6)L(6,2;5,2^{'}) \tag{1.20}$$

where the Kernel Ξ is the sum of the derivatives of the Hartree potential and the self-energy (e.g. GW approximation) with respect to a one-particle Green's function. In practical applications, BSE is applied within the linear response approach where the excitation energies correspond to the poles of the two-particle correlation function.[4, 52] Furthermore, the most common implementations of the BSE are based on the electron-hole representation that allows to rewrite equation 1.20 into the following non-Hermitian eigenvalue problems:

$$\hat{H}_{exc}|\lambda\rangle = E_{\lambda}|\lambda\rangle \tag{1.21}$$

that has the same block matrices shape of the TD-DFT equation in the Casida's approach. BSE calculations are generally carried out by reading the GW data as input and hence by adopting the GW approximation to the self-energy and by

solving either the full-BSE problem (equation 1.21) or its TDA.[58, 59] In this thesis we make use of both GW and BSE methods for molecule/Semiconductor interfaces and bulk Semiconductors making use of plane wave basis and pseudopotentials. However, we should mention that GW and BSE start to be popular also for the study of isolated molecular systems where these methods are implemented with localized basis set.[53, 60, 61]

1.3 MD simulations

MD allows to represent the motion of atoms and molecules over time. Also, for long enough simulations, and for systems that obey to ergodic hypothesis, MD can reproduce the macroscopic thermodynamic properties.[62]

MD simulations are carried out by treating the nuclei as classical particles and by using the Newton's Laws of motion to calculate the forces on the atoms for each MD step. The MD trajectory is hence computed by using the forces to propagate the nuclei for another MD step forward in time considering a given time-step and repeating this procedure for the whole MD simulation.[63, 64]

In ab-initio MD (AIMD) simulations, the energy and the forces are calculated at QM level, in general, with any method that provides gradients, or ideally analytical gradients. In most cases, ab-initio MD is carried out by adopting the Born-Oppenheimer approximation (BOMD) and by calculating the energies/forces for each MD step by solving an approximation of equation 1.6.[65, 66] For example, within DFT framework, the BOMD are carried out by solving the KS equations. Clearly, the quality of the DFT MDs depend on the quality of the potential energy surface and hence on the employed functional.

On the other hand, in classical MD, the energy/forces are calculated from Molecular Mechanics (MM), by a defined Force Field (FF) which approximates the potential energy with a series of functionals.[67] In particular, the functionals can be

partitioned into bonded and non-bonded terms:

$$\begin{aligned} E_{FF} &= E_{bonded} + E_{non-bonded} \\ E_{bonded} &= E_{bond} + E_{angle} + E_{torsion} \\ E_{non-bonded} &= E_{electrostatic} + E_{VDW} \end{aligned} \tag{1.22}$$

In most cases, the bonded terms (stretching, bending and torsions) are treated by harmonic or periodic functions whereas the non-bonded part consists of the sum of a Coulombic term, to describe the charge-charge interactions, and a Van Der Walls (VDW) term usually treated with a Lennard-Jones (LJ) potential.[64] In general, the parameters composing these functions are fitted against the QM calculations or the experimental measurements.

The most common FFs used within the MD community are AMBER,[68] OPLS[69] and CHARMM[70] and for all of these the adopted functional form is quite similar. However, these FFs, which are adapted to simulate a wide range of molecular systems, ranging from small organic molecules to large proteins, are not adapted to properly describe any specific molecule. Indeed, the common aspect of these approaches is the use of standard parameters, properly fitted and tested for a series of molecules belonging to a given molecular class (e.g. small organic molecules), to build the FF of any molecule of the same class. The limitations of these methods are also their strength; indeed, the generality and the transferability of these FFs allow to easily simulate any molecules with minimal efforts by the user.

To overcome these limitations, it is possible to parametrize the FF by fitting the parameters of the functions in equation 1.22 against the QM calculations for a specific system. Obviously, this approach allows to have a more accurate description of the potential energy and of the MD trajectory even if it is clearly time-demanding and not transferable like standard FF approaches. Many examples of specifically tuned Force Fields[71–76] have been developed in the last years and we will discuss in detail one of this approach, i.e. JOYCE, in Section 2.3.

It is important to stress that, although the classical MD approach is the only available method able to treat large biomolecules (i.e. proteins) and capable of achieving the millisecond timescale, it remains inherently approximate and unable to describe QM effects.[64] However, it is possible to combine the QM and the

MM approaches within the QM/MM model[77] where a small part of the system (usually the solute or a part of it) is treated at QM level and the remainder classically. In this way, with limited computational effort one could take into account environmental effects (solvent, ions) at MM level and dynamical effects and describing at the same time the solute at QM level.

Bibliography

[1] E. A. Carter, *Science* **2008**, *321*, 800–803.

[2] A. Dreuw, M. Head-Gordon, *J. Am. Chem. Soc.* **2004**, *126*, 4007–4016.

[3] A. Dreuw, J. L. Weisman, M. Head-Gordon, *J. Chem. Phys.* **2003**, *119*, 2943–2946.

[4] S. Ghosh, P. Verma, C. J. Cramer, L. Gagliardi, D. G. Truhlar, *Chem. Rev.* **2018**, *118*, 7249–7292.

[5] K. Berland, V. R. Cooper, K. Lee, E. Schröder, T. Thonhauser, P. Hyldgaard, B. I. Lundqvist, *Rep. Prog. Phys.* **2015**, *78*, 066501.

[6] A. Szabo, N. S. Ostlund, Modern Quantum Chemistry: Introduction to Advanced Electronic Structure Theory, Dover Publications, **1996**.

[7] T. Helgaker, P. Jorgensen, J. Olsen, Molecular Electronic-structure Theory, Wiley, **2008**.

[8] J. M. Combes, P. Duclos, R. Seiler in Rigorous Atomic and Molecular Physics, (Eds.: G. Velo, A. S. Wightman), Springer US, Boston, MA, **1981**, pp. 185–213.

[9] G. A. Worth, L. S. Cederbaum, *Annu. Rev. Phys. Chem.* **2004**, *55*, 127–158.

[10] T. Horio, T. Fuji, Y.-I. Suzuki, T. Suzuki, *J. Am. Chem. Soc.* **2009**, *131*, 10392–10393.

[11] J. Bloino, A. Baiardi, M. Biczysko, *Int. J. Quantum Chem.* **2016**, *116*, 1543–1574.

[12] J. Cerezo, F. J. Avila Ferrer, G. Prampolini, F. Santoro, *J. Chem. Theory Comput.* **2015**, *11*, 5810–5825.

[13] P. Hohenberg, W. Kohn, *Phys. Rev.* **1964**, *136*, B864–B871.

[14] W. Kohn, L. J. Sham, *Phys. Rev.* **1965**, *140*, A1133–A1138.

[15] R. O. Jones, *Rev. Mod. Phys.* **2015**, *87*, 897–923.

[16] N. Ashcroft, N. Mermin, Solid State Physics, Cengage Learning, **2011**.

[17] D. R. Hamann, *Phys. Rev. B* **2013**, *88*, 085117.

[18] V. Heine in (Eds.: H. Ehrenreich, F. Seitz, D. Turnbull), Solid State Physics, Academic Press, **1970**, pp. 1–36.

[19] W. E. Pickett, *Comput. Phys. Rep.* **1989**, *9*, 115–197.

[20] F. A. Evangelista, *J. Chem. Phys.* **2018**, *149*, 030901.

[21] K. D. Vogiatzis, D. Ma, J. Olsen, L. Gagliardi, W. A. de Jong, *J. Chem. Phys.* **2017**, *147*, 184111.

[22] J. Olsen, P. Jørgensen, J. Simons, *Chem. Phys. Lett.* **1990**, *169*, 463–472.

[23] M. Aida, M. Kaneko, M. Dupuis in Computational Molecular Biology, (Ed.: J. Leszczynski), Theoretical and Computational Chemistry, Elsevier, **1999**, pp. 211–243.

[24] J. Olsen, *Int. J. Quantum Chem.* **2011**, *111*, 3267–3272.

[25] C. Angeli, R. Cimiraglia, S. Evangelisti, T. Leininger, J.-P. Malrieu, *J. Chem. Phys.* **2001**, *114*, 10252–10264.

[26] J. Finley, P.-Å. Malmqvist, B. O. Roos, L. Serrano-Andrés, *Chem. Phys. Lett.* **1998**, *288*, 299–306.

[27] P. G. Szalay, T. Müller, G. Gidofalvi, H. Lischka, R. Shepard, *Chem. Rev.* **2012**, *112*, 108–181.

[28] R. J. Bartlett, M. Musiał, *Rev. Mod. Phys.* **2007**, *79*, 291–352.

[29] R. Colle, O. Salvetti, *J. Chem. Phys.* **1983**, *79*, 1404–1407.

[30] C. Lee, W. Yang, R. G. Parr, *Phys. Rev. B* **1988**, *37*, 785–789.

[31] Y. Zhao, D. G. Truhlar, *Acc. Chem. Res.* **2008**, *41*, 157–167.

[32] S. A. Mewes, F. Plasser, A. Krylov, A. Dreuw, *J. Chem. Theory Comput.* **2018**, *14*, 710–725.

[33] T. Yanai, D. P. Tew, N. C. Handy, *Chem. Phys. Lett.* **2004**, *393*, 51–57.

[34] M. Casida, M. Huix-Rotllant, *Annu. Rev. Phys. Chem.* **2012**, *63*, 287–323.

[35] J. Delhalle, J.-L. Calais, *Phys. Rev. B* **1987**, *35*, 9460–9466.

[36] P. Verma, D. G. Truhlar, *Trends Chem.* **2020**, *2*, Special Issue - Laying Groundwork for the Future, 302–318.

[37] L. Zecca, P. Gori-Giorgi, S. Moroni, G. B. Bachelet, *Phys. Rev. B* **2004**, *70*, 205127.

[38] B. G. Janesko, T. M. Henderson, G. E. Scuseria, *Phys. Chem. Chem. Phys.* **2009**, *11*, 443–454.

[39] M. Cococcioni, S. de Gironcoli, *Phys. Rev. B* **2005**, *71*, 035105.

[40] B. Himmetoglu, A. Floris, S. de Gironcoli, M. Cococcioni, *Int. J. Quantum Chem.* **2014**, *114*, 14–49.

[41] A. I. Liechtenstein, V. I. Anisimov, J. Zaanen, *Phys. Rev. B* **1995**, *52*, R5467–R5470.

[42] M. Marques, E. Gross, *Annu. Rev. Phys. Chem.* **2004**, *55*, 427–455.

[43] E. Runge, E. K. U. Gross, *Phys. Rev. Lett.* **1984**, *52*, 997–1000.

[44] M. E. Casida, *J. Mol. Struct.* **2009**, *914*, 3–18.

[45] D. Rocca, R. Gebauer, Y. Saad, S. Baroni, *J. Chem. Phys.* **2008**, *128*, 154105.

[46] S. Hirata, M. Head-Gordon, *Chem. Phys. Lett.* **1999**, *314*, 291–299.

[47] Y. Shao, Y. Mei, D. Sundholm, V. R. I. Kaila, *J. Chem. Theory Comput.* **2020**, *16*, 587–600.

[48] T. Sander, E. Maggio, G. Kresse, *Phys. Rev. B* **2015**, *92*, 045209.

[49] T. D. Kühne, M. Iannuzzi, M. Del Ben, V. V. Rybkin, P. Seewald, F. Stein, T. Laino, R. Z. Khaliullin, O. Schütt, F. Schiffmann, D. Golze, J. Wilhelm, S. Chulkov, M. H. Bani-Hashemian, V. Weber, U. Borstnik, M. Taillefumier, A. S. Jakobovits, A. Lazzaro, H. Pabst, T. Müller, R. Schade, M. Guidon, S. Andermatt, N. Holmberg, G. K. Schenter, A. Hehn, A. Bussy, F. Belleflamme, G. Tabacchi, A. Glöß, M. Lass, I. Bethune, C. J. Mundy, C. Plessl, M. Watkins, J. VandeVondele, M. Krack, J. Hutter, *J. Chem. Phys.* **2020**, *152*, 194103.

[50] S. Refaely-Abramson, M. Jain, S. Sharifzadeh, J. B. Neaton, L. Kronik, *Phys. Rev. B* **2015**, *92*, 081204.

[51] G. Onida, L. Reining, A. Rubio, *Rev. Mod. Phys.* **2002**, *74*, 601–659.

[52] Y. Ping, D. Rocca, G. Galli, *Chem. Soc. Rev.* **2013**, *42*, 2437–2469.

[53] C. Faber, P. Boulanger, C. Attaccalite, I. Duchemin, X. Blase, *Philos. Trans. Royal Soc. A* **2014**, *372*, 20130271.

[54] L. Hedin, *Phys. Rev.* **1965**, *139*, A796–A823.

[55] M. S. Hybertsen, S. G. Louie, *Phys. Rev. B* **1986**, *34*, 5390–5413.

[56] F. Bruneval, M. A. L. Marques, *J. Chem. Theory Comput.* **2013**, *9*, 324–329.

[57] A. L. Fetter, J. D. Walecka, Quantum Theory of Many-Particle Systems, McGraw-Hill, Boston, **1971**.

[58] S. Albrecht, L. Reining, R. Del Sole, G. Onida, *Phys. Rev. Lett.* **1998**, *80*, 4510–4513.

[59] L. X. Benedict, E. L. Shirley, R. B. Bohn, *Phys. Rev. Lett.* **1998**, *80*, 4514–4517.

[60] F. Caruso, P. Rinke, X. Ren, A. Rubio, M. Scheffler, *Phys. Rev. B* **2013**, *88*, 075105.

[61] X. Blase, C. Attaccalite, *Appl. Phys. Lett.* **2011**, *99*, 171909.

[62] M. Karplus, J. A. McCammon, *Nat. Struct. Biol.* **2002**, *9*, 646–652.

[63] B. J. Alder, T. E. Wainwright, *J. Chem. Phys.* **1959**, *31*, 459–466.

[64] S. A. Hollingsworth, R. O. Dror, *Neuron* **2018**, *99*, 1129–1143.

[65] M. C. Childers, V. Daggett, *Mol. Syst. Des. Eng.* **2017**, *2*, 9–33.

[66] R. Iftimie, P. Minary, M. E. Tuckerman, *Proc. Natl. Acad. Sci. USA* **2005**, *102*, 6654–6659.

[67] H. Heinz, T.-J. Lin, R. Kishore Mishra, F. S. Emami, *Langmuir* **2013**, *29*, 1754–1765.

[68] J. Wang, R. M. Wolf, J. W. Caldwell, P. A. Kollman, D. A. Case, *J. Comput. Chem.* **2004**, *25*, 1157–1174.

[69] W. Damm, A. Frontera, J. Tirado Rives, W. L. Jorgensen, *J. Comput. Chem.* **1997**, *18*, 1955–1970.

[70] K. Vanommeslaeghe, E. Hatcher, C. Acharya, S. Kundu, S. Zhong, J. Shim, E. Darian, O. Guvench, P. Lopes, I. Vorobyov, A. D. Mackerell Jr., *J. Comput. Chem.* **2010**, *31*, 671–690.

[71] G. Prampolini, P. R. Livotto, I. Cacelli, *J. Chem. Theory Comput.* **2015**, *11*, 5182–5196.

[72] S. Kraner, G. Prampolini, G. Cuniberti, *J. Phys. Chem. C* **2017**, *121*, 17088–17095.

[73] L. Greff da Silveira, M. Jacobs, G. Prampolini, P. R. Livotto, I. Cacelli, *J. Chem. Theory Comput.* **2018**, *14*, 4884–4900.

[74] G. Belletti, E. Schulte, E. Colombo, W. Schmickler, P. Quaino, *Chem. Phys. Lett.* **2019**, *735*, 136778.

[75] K. Claridge, A. Troisi, *J. Phys. Chem. B* **2019**, *123*, 428–438.

[76] L. Jiang, D. M. Rogers, J. D. Hirst, H. Do, *J. Chem. Theory Comput.* **2020**, *10.1021/acs.jctc.0c00399*.

[77] S. Ahmadi, L. Barrios Herrera, M. Chehelamirani, H. Jiri, S. Jalife, D. R. Salahub, *Int. J. Quantum Chem.* **2018**, *118*, e25558.

Chapter 2
Optical and dynamical properties of Perylene-Diimides-based (PDI) chromophores

The results presented in this chapter have been reproduced from:

- **Computational Modeling of Exciton Localization in Self-Assembled Perylene Helices: Effects of Thermal Motion and Aggregate Size** A. Segalina, X. Assfeld, A. Monari and M. Pastore, J. Phys. Chem. C. **2019**, 123, 6427–6437.[1]
- **Accounting for vibronic features through a mixed quantum-classical scheme: structure, dynamics and absorption spectrum of a perylene diimide dye in solution** A. Segalina, J. Cerezo, G. Prampolini, F. Santoro and M. Pastore, J. Chem. Theory Comput. **2020**, 10.1021/acs.jctc.0c00919.[2]

2.1 Motivation and background

The development of materials based on molecular aggregates of π-conjugated organic molecules is of great and increasing interest for many technological applications,[3] such as Field Effect Transistors (OFETs),[4] photovoltaics and photocatalytic devices,[5, 6] and Light Emitting Diodes (OLEDs).[7] As a matter of fact, the electronic and optical properties of these materials do not depend solely on the properties of the monomeric building blocks but also the structure of their relative aggregates play a fundamental role.[8] Kasha in the 1960's argued for the first time the relation between the optical properties of molecular aggregates and their packing geometries.[9] In particular, within Kasha's model the variation of the photophysical properties of molecular aggregates with respect to the monomer can be predicted based solely on geometric considerations and on the change in the coupling between the respective transition dipole moments. In a simple dimeric aggregate, a blue-shifted absorption maximum and a weaker radiative decay rate compared with the monomer are predicted when the aggregation geometry is "side-by-side" (H aggregate) or conversely, in the case of a "head-to-tail" arrangement (J aggregate), the absorption maximum is red-shifted, and a more important radiative decay rate is obtained.[8]

In many cases the π-conjugated molecules spontaneously form ordered aggregates giving rise to the so-called self-assembled aggregates.[10–12] In particular, the self-assembly process may be helped by the presence of Semiconductor that via non-covalent interactions can stabilize the molecular units on the surface.[5, 11, 13, 14] Surfaces coated with organic molecules have been largely exploited in photocatalysis and photovoltaic devices, as surface functionalization is at the heart of the functioning of Dye-Sensitized photoelectrodes in Grätzel Solar Cells (DSSCs)[15–17] and Photoelectrochemical Cells (DSPECs)[17–19] for water splitting. Dye aggregation on the metal oxide surface is, however, generally regarded as being responsible for low cell efficiencies and thus is prevented by the use of antiaggregation coadsorbents.[20, 21] On the contrary, some examples of beneficial aggregation effects have been reported, including perylene-diimides-based (PDI) aggregates, Figure 2.1 panel a), that have been successfully exploited as photoactive materials in dye-sensitized photoanodes for water oxidation.[5, 22, 23]

In particular, the surface sensitization by hydrophobic PDI aggregates, adsorbed on the surface by electrostatic and dispersion interactions, does not trigger the hydrolytic cleavage[24] generally observed for conventional (carboxylic or phosphonic) anchoring groups.[25, 26]

PDI-based chromophores have been widely employed thanks to their notable chemical, thermal and photochemical stability, wide and intense optical absorption in the visible to near-infrared spectral window and excellent charge transport properties.[5, 22, 23, 27–33] The optical properties of PDI aggregates, in agreement

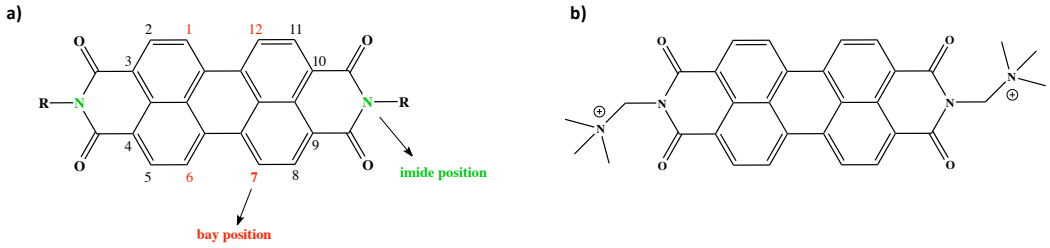

Figure 2.1: a) Chemical structure of a generic PDI sensitizer: the bay and imide positions are evidenced in red and green, respectively. b) N,N′ -bis(2-(trimethylammonium)-ethylene)-perylene-3,4,9,10-tetracarboxylic acid bis-imide PDI molecule investigated in this thesis.

with the Kasha's model, are strongly linked to their aggregates form. The side chains (R substituents at the imide position, see Figure 2.1) control the solubility of PDIs derivatives, and dictate the molecular packing conformation, hence modulating the color and other physico-chemical properties of the aggregates.[34] These side chains, however, do not directly affect the absorption and emission properties, because the HOMO and LUMO orbitals, which describe the $S_0 \rightarrow S_1$ transition in a single particle picture, present nodal planes at the imide nitrogens.[35] On the other hand, the modulation of the optical properties of monomers can be efficiently obtained, when PDIs are substituted at the aromatic core, in the bay positions (1, 6, 7 and 12 evidenced in Figure 2.1a).[34, 36]

The lowest-energy Excited State of a PDI monomer is usually energetically well separated from the other bright transitions and presents an absorption maximum around 530 nm, in ACN solution, with a marked vibronic progression. The formation of PDI aggregates entails a change on the vibronic structure of the absorption spectrum, although it delivers small effects on the spectra position. The inten-

sity reversal between the $0 \rightarrow 0$ and $0 \rightarrow 1$ vibronic bands is in fact generally used as a spectral signature of the formation of PDI-aggregates in solution or on Semiconductor surfaces.[5, 13, 14]

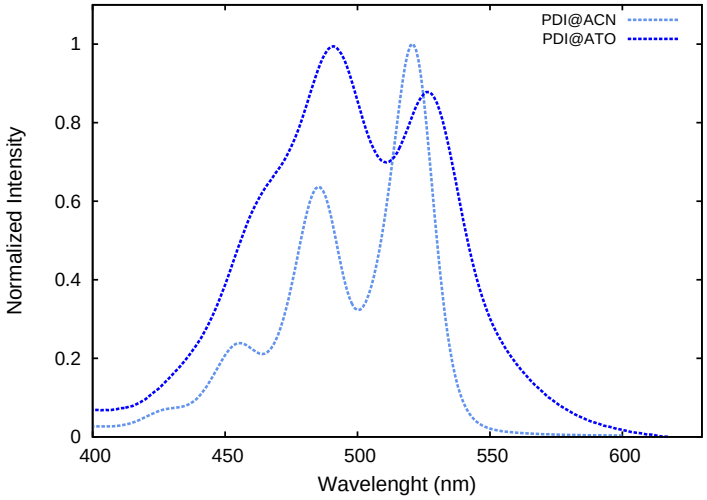

Figure 2.2: Experimental normalized absorption spectra of PDI in ACN solution (PDI@ACN) and PDI aggregates deposited onto ATO (PDI@ATO)

In particular, the N,N′-bis(2-(trimethylammonium)-ethylene)-perylene-3,4,9,10 -tetracarboxylic acid bis-imide (Figure 2.1b), hereafter referred to as PDI, has proved capable to spontaneously form stable face-to-face H-aggregates on several Semiconductor surfaces (i.e. TiO_2, WO_3, ATO and SnO_2) as pointed out by the vibronic signature of its absorption spectra (Figure 2.2).[5, 23] In the context of DSPECs, the PDI demonstrated great capacity to transfer photogenerated holes to sacrificial species in solution and to IrO_2 nanoparticles that act as water oxidation catalysts.[23] The main limitation of PDI-based dye sensitizers, despite their systematic modification with various anchoring and electron donor groups, remains the lack of strongly directional Charge Transfer (CT) from the molecule toward the Semiconductor surface.[37] To optimize the optoelectronic and charge transport properties of ordered aggregates, it is, thus, pivotal to understand how the nature (Frenkel-type or CT-like), localization (i.e. exciton length) and photophysics are modified by the complex network of intermolecular interactions. In fact, the device optical and photophysical response, as well as the efficiency of

the charge transport mechanism, might be remarkably influenced by the packing arrangement, which is in turn driven by the competition among different noncovalent, inter-molecular forces, as for instance hydrogen bonds, cation–π interactions or $\pi - \pi$ stacking.

From a theoretical and computational point of view, the route to an accurate description of the electronic spectra of large-sized molecular aggregates presents a number of challenging tasks: i) the configurational space sampling of the multichromophoric assembly in the Ground electronic State; ii) the treatment of both solute-solute and solute-solvent interactions, which might require to be included explicitly, to account for strong and local phenomena as for instance Hydrogen-bonds; iii) the inclusion of inter- and intra-molecular quantum vibronic effects in the calculation of the absorption spectra; iv) the necessity of considering the coupling between multiple exciton and/or CT quasi-degenerate Excited States, participating in the aggregate's spectrum. However, there is no well established methodology merging all these capabilities in a unique computational protocol and a combination of different methods is hence necessary to account for all these effects.

Tasks i) and ii) can be tackled resorting to a Classical (CL) description of the nuclear dynamics, which allows for the simulation of the wide time and length scale required to observe self-assembly phenomena. Yet, as far as π-conjugated molecules are concerned, care should be taken in selecting a proper Force Field (FF) parameter set, capable to accurately describe both monomer flexibility and intermolecular interactions, eventually leading to a reliable representation of the π-π driven aggregation. This might introduce a further obstacle, which can be overcome by refining or fully re-parameterizing the FF, based on accurate Quantum Mechanical (QM) data, as recently reported by several groups. [38–43] Once the reliability of the classical MD trajectories has been validated, a very convenient method to compute spectra of complex and flexible systems in explicit environments is performing a Classical Ensemble Average of Vertical Excitations (CEA-VE)2.2. Within the CEA-VE framework, the explicit solute-solvent and solute-solute interactions mentioned in ii) can be accounted for straightforwardly, for example with a Quantum Mechanics/Molecular Mechanics (QM/MM) scheme.[44] However, the CEA-VE approach is not able, by definition, to describe the vibronic effects mentioned in

iii), which can only be properly simulated accounting for the quantum nature of nuclear motion. It is worthy to notice that the latter are responsible for the appearance of vibronic progressions, usually observed in experiments as in the case of PDI. In addition, they also impact remarkably structureless bands, modifying the spectral maximum and increasing its width.[45–47] Finally, tackling task iv) to achieve a proper description of the effect of inter-state couplings among quasi-degenerate states requires the adoption of quantum dynamical methods based on wavepacket propagations on the coupled potential surfaces, which, however, we have not addressed in this thesis.

In the first part of this chapter (Section 2.2) we provide an in-depth analysis of the dynamical, optical properties of the PDI aggregates, closely looking at the role played by the thermal fluctuations and the aggregates size on the Excited-State properties. In particular, we make use of the CEA-VE approach for the calculation of the electronic spectra and the Generalized AMBER Force Field (GAFF) for the MD simulations.

In the second part of this chapter (Section 2.3), we refine the classical description of the PDI conformational space, and hence of the MD simulations, through the parametrization of a PDI-specific Quantum-Mechanically Derived Force Field (QMD-FF). In Section 2.3, we also address the calculation of the vibronic spectra of the PDI molecule adopting a Mixed Quantum-Classical (MQC) approach based on an adiabatic separation of soft(CL)/stiff(QM) nuclear Degrees of Freedom. Within the MQC approach the spectrum is obtained as a conformational average (over the soft coordinates) of vibronic spectra (for the stiff coordinates) that are obtained through the Generalized Vertical Hessian (gVH) vibronic approach. In particular, the average has been performed over snapshots extracted from classical Molecular Dynamics (MD) runs, performed with the above mentioned QMD-FF.

2.2 Self-Assembled Perylene Helices

In this section, we model the optical properties of PDI helix-like aggregates of different sizes in solution and at room temperature. Experimental observations reveal moderate delocalization of the Frenkel excitonic state in disordered (“300

K") aggregates, mostly involving three to four units, even in larger helices.[48] As a matter of fact, the PDI aggregates are characterized by a complex photophysics, in particular, some authors have suggested that both localized excimers and low-energy CT states take part to the Excited State relaxation dynamics, with a decisive role of the packing arrangement in driving the process.[49–54] In the last decades, exciton diffusion dynamic, excimer formations and self-trapping processes in ordered perylene aggregates have been largely investigated by both computational and experimental methods.[49, 50, 54–63] In this thesis we have extended the knowledge of these phenomena through a multiscale protocol aims at getting detailed insights into the exciton nature in large PDI aggregates (up to seven units). In particular, we have combined first-principles DFT, TD-DFT, one-particle transition density matrix (1TDM) analysis of the Excited States, and classical MD simulations to rationalize the role of the thermal motion and the aggregate size on the exciton localization. This section is organized as follows: the details of the computational methods are collected in the next subsection, while subsections 2.2.2-2.2.4 collect the core result and the final remarks of this work.

2.2.1 Computational details

Static Quantum-Chemistry Calculations

First, the PDI monomer and the small-size aggregates (up to four units) have been studied using DFT to obtain the GS equilibrium geometry. On top of equilibrium geometries, the absorption spectrum has been simulated at the TD-DFT level of theory. Geometry optimization of the PDI monomer and its aggregates (dimer, trimer, and tetramer) was carried out using the M062X[64]/6-31G* level of calculation coupled to the Conductor-like Polarizable Continuum Model (C-PCM)[65] to take into account the solvation effects (ACN and water were considered). The calculations of the excitation energies for the monomer were carried out by TD-DFT with different functionals (PBE0, B3LYP, MPW1K, CAM-B3LYP) to calibrate the level of calculation by comparison with the available experimental data. In the case of the aggregates, only the hybrid B3LYP and the long-range corrected CAM-B3LYP functionals have been considered. The first 10, 20, 30, 40 and 70

vertical excitation energies have been obtained for the monomer, dimer, trimer, tetramer and heptamer respectively. To allow a better comparison with experimental results, the simulated spectra have been obtained by convoluting the vertical transitions with Gaussian functions having full width at half-maximum (fwhm) of 0.2 eV. All static calculations have been performed using the Guassian09 suite of code.[66]

Molecular Dynamics

Classical Molecular Dynamics (MD) simulations have been performed for both the PDI monomer and the aggregates (4 and 7 units) to explore the conformational space of the Ground State. On top of the MD trajectories, statistically independent snapshots have been extracted to calculate the Excited-State manifold and hence simulate the absorption spectrum as the convolution of the individual vertical transitions. The Generalized AMBER Force Field (GAFF)[67] was used to describe the PDI potential, the point charges have been reparameterized to fit the restricted electrostatic potential (RESP),[68] the solvent molecules have been described by the TIP3P model for water molecules,[69] and two counteranions (Cl^-) were added in the simulation box to ensure electroneutrality. The systems were set up starting from the QM-optimized geometries of the monomers and aggregates, with the exception of the heptamer case, for which the system was built by replicating the QM-optimized geometrical arrangement of the PDI dimer. The simulation boxes were composed of the solute and 2870, 4130, and 5166 water molecules for the PDI monomer, tetramer, and heptamer, respectively. Periodic Boundary Conditions (PBCs) have been used throughout, and all of the simulations have been performed with the AMBER code and its GPU extension.[70] After an initial energy minimization carried out for 10000 cycles to remove bad contacts, followed by equilibration and thermalization, conducted for 0.4 and 0.2 ns, respectively, production runs of 0.2 μs for PDI monomer and 1 μs for PDI aggregates were executed in the NPT ensemble at 1 atm and 300 K. Newton equations of motion were solved considering a time step of 2 fs using the RATTLE algorithm to fix the bond distances involving hydrogen atoms.

CEA-VE Spectra Calculations

From the monomer, tetramer, and heptamer MD trajectories, 100 conformations of the solute were extracted, equally spaced in terms of time, to perform Excited-State calculations using the AMBER/TeraChem interface.[70–73] To save computational time, especially in the case of the large heptamer aggregates, the peripheral trimethylammonium ethylene chains were cut, and the dangling bonds were saturated with a hydrogen atom using the link atom scheme approach. Vertical excitations were obtained at the TD-DFT level of theory using the TDA[74] and a 6-31G* basis set. In the case of the monomer, both B3LYP[75] and CAM-B3LYP[76] functionals have been employed, whereas in the case of the aggregates, only CAMB3LYP has been used to avoid the underestimation of the excitation energy of long-range CT states when using nonlong- range-corrected functionals. Solvation effects (water) were accounted for via a continuum polarization approach, namely, the Conductor-like Screening Model (COSMO)[77], as implemented in TeraChem. The calculated CEA-VE spectra were reproduced through a convolution with Gaussian functions having a fwhm of 0.1 eV.

Excited-State and Exciton Analysis

To unravel the topological characteristics of the different Excited States, we performed a decomposition of the 1TDM following the procedure implemented in the TheoDORE 1.7 package.[78–80] TheoDORE performs a one-to-one mapping of the 1TDM with a general exciton wave function $\chi(r_H, r_E)$, where r_H stands for the position operator of the hole and r_E is that of the electron. Following a preliminary, and, in large measure, arbitrary, partition of the chemical space of the (multi)chromophore systems in terms of monomeric units, it is hence possible to obtain important quantitative indexes describing exciton delocalization and charge separation. In particular, we will define the CT index that may assume values comprised between 0.0, in case of purely local excitation, and 1.0, indicative of important charge separation. Note that because our calculations have been performed in a TD-DFT (TDA) framework and hence only single excitations are taken into account, CT of 1.0 will be representative of a total charge separation with no spatial overlap between the hole and particle densities. In the same way,

the 1TDM may be decomposed in terms of the Participation Ratio (PR) index, that roughly gives the number of monomeric units over which the exciton wave function is delocalized and hence gives a direct measure of the exciton length. For our application, the partition of the chemical space was straightforward, and indeed each PDI monomer has been considered as a monomeric unit. Hence PR will directly give the number of PDI units over which the electronic density is delocalized. If, for simplicity, we consider the dimer case, PR close to 2.0 and CT close to 0.0 will represent a pure Frenkel delocalized exciton.

2.2.2 DFT analysis of the structural and optical properties of PDI aggregates

To preliminarily calibrate the level of calculation, the vertical (E_{max}) and adiabatic ($E_{0\text{-}0}$) excitation energies of the PDI monomer in ACN solution and water were calculated using different exchange and correlation functionals and compared with the experimental values, which were obtained for the PDI in ACN solution. The results are reported in Table 2.1.

FUNCTIONAL	$E_{0\text{-}0}$ ACN (eV)	$E_{0\text{-}0}$ WAT (eV)	E_{MAX} WAT (eV)
B3LYP	2.21	2.21	2.38
PBE0	2.28	2.29	2.45
MPW1K	2.49	2.49	2.64
CAM-B3LYP	2.52	2.52	2.69
EXP (ACN)	2.36		2.38

Table 2.1: Calculated $E_{0\text{-}0}$ and vertical excitation energies in eV for the PDI molecule in Acetonitrile (ACN) and Water (WAT)

As expected, the lowest energy bright state of PDI is described by a single electronic excitation from the HOMO to the LUMO, which is localized on the perylene's conjugate core, and no involvement of the lateral charged chains (trimethylammonium - ethylene) is observed.[81] As a first important point, if we compare the $E_{0\text{-}0}$ energies obtained from the TD-DFT calculations in water and those obtained in ACN, then we can underline the modest or even negligible solvatochromism observed for those systems at C-PCM level. This will, in turn, justify our choice to perform the subsequent calculations involving MD simulations in

water, for which one has well-tested Force Field parameters.

On the contrary, the good agreement between the experimental value of $E_{0\text{-}0}$ and the one calculated with the PBE0 functional also stands out. In the case of vertical excitation energies, B3LYP appears as the outperforming functional; hence globally and, as expected, the hybrid functionals incorporating a moderate fraction of nonlocal exchange are by far the most appropriate ones to model the optical properties of PDI, that is, paradigmatic π-conjugated organic systems.[53] Furthermore, because B3LYP was also performing rather satisfactorily concerning the value obtained for the adiabatic excitation energies, we decided to systematically use this functional for the following study and the topological characterization of the monomers. The ab initio equilibrium geometries obtained for the PDI monomer and dimer are reported in Figure 2.3.

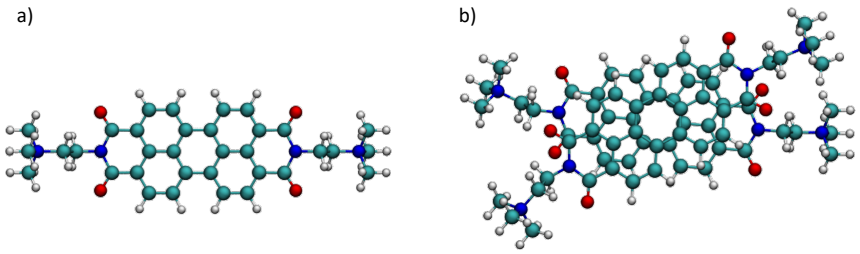

Figure 2.3: Optimized structure of PDI monomer (a) and dimer (b).

To find the most stable dimeric configuration, a relaxed dihedral angle scan between two PDI molecules has also been performed, and, as reported elsewhere for analogous perylenes, the total energy minimum for the stacked PDI dimer was found for a dihedral angle of $\sim 30°$ between the PDI units.[13] Thus the trimer was built starting from the optimized dimer geometry and placing the third unit at 30° or -30° with respect to the adjacent molecule, building the so-called "alternated type" and the "helix-like" aggregate, respectively (Figure 2.4). The two conformations were found to be quasi-degenerate because the "helix-like" structure resulted in being only 0.37 kcal/mol below the "alternated type" one. In the case of the tetramer, the "helix-like" and the "alternated-type" aggregates were manually constructed and then fully optimized; once again, the former conformation

appears to be more stable by ~ 1.52 kcal/ mol. Obviously, this quasi-degeneracy is indicative of a significant Boltzmann population of both states and conformers. However, as we shall discuss later, the coexistence of the two conformations has a negligible influence on the position of the absorption maximum. Finally, the distance between the center of mass of the PDI monomers was calculated to be ca. 3.5 Å, in good agreement with the values expected for π-stacked systems.[13, 82]

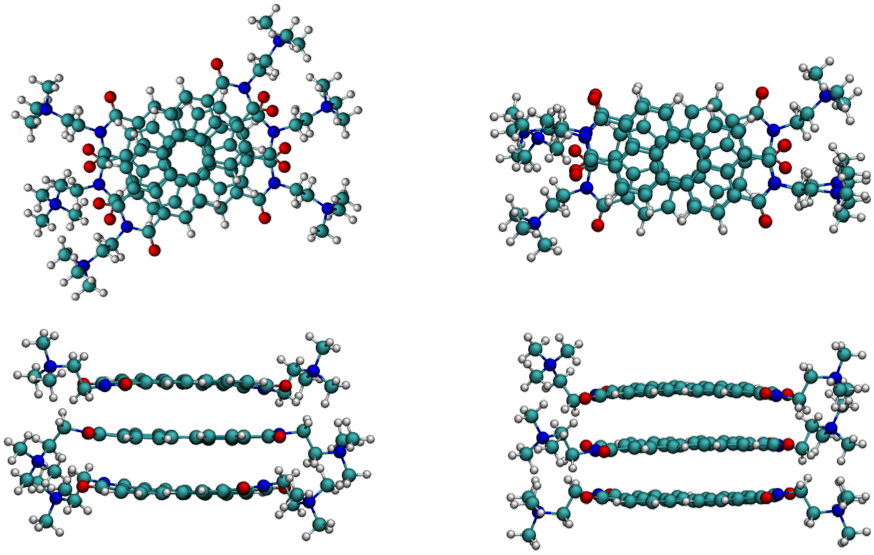

Figure 2.4: PDI trimer in "helix-like" geometry (left) and in "alternated-type" geometry (right).

To quantify the magnitude of the forces leading to self-organization in the GS, the binding energies were calculated for the fully relaxed aggregates in "helix-like" geometries. In Figure 2.5, the normalized binding energy per unit is reported versus the number of monomer. An increase in the normalized binding energy for the larger systems is evident, hence showing a nonadditive and cooperative stabilization, which appears to start reaching a plateau for the tetramer aggregate. The per-unit binding energies are comprised between 14.90 (dimer) and 22.14 kcal/mol (tetramer). From the respective equilibrium geometries, vertical excitation energies were computed for the aggregates, also considering both possible conformations in the case of trimer, tetramer, and heptamer.

The convoluted spectra up to the tetramer are displayed in Figure 3 compared with the experimental ones, whereas the corresponding vertical excitation energies

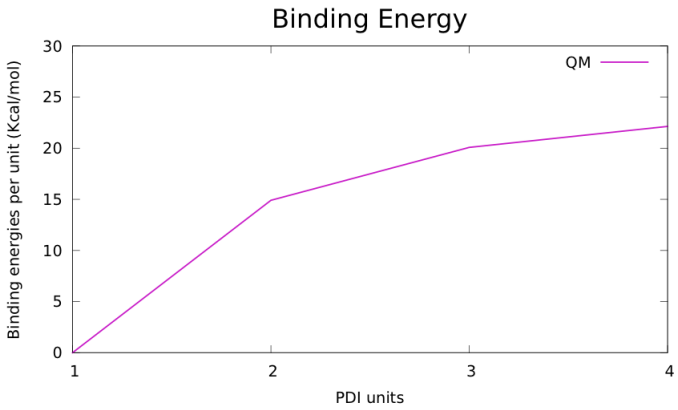

Figure 2.5: Binding energies per unit for the aggregates system obtained at the M062X/6-31G* level of theory in water (C-PCM) considering the DFT optimized geometries (QM).

of the bright states and their oscillator strengths are listed in Table 2.2, along with the experimental absorption maxima and the calculated CT number and PR indices. To check on the convergence of the aggregates' optical properties, we also added to Table 2.2 the calculated vertical excitation energies at the TDA/COSMO level of theory (see Section 2.3) for the heptamer aggregates optimized using the AMBER Force Field (FF).

Note that in Figure 2.6, the "helix-like" geometries for the trimer and tetramer were arbitrarily chosen given the negligible differences in the position of the calculated absorption maxima (Table 2.2), amounting to 0.02 eV at most in the case of the trimer. In Figure 2.6, it is possible to evidence the blue shift and the decrease in the oscillator strength (hypochromism) from the monomer to the larger aggregates, which are typical features observed in the case of H aggregates.[9, 83, 84] Moreover, a good agreement between the absorption maxima of the experimental spectrum of the aggregate (blue dashed line) and those of trimer (violet full line) and tetramer (magenta full line) also appears, as confirmed by the data in Table 2.2. The calculated excitation energies for the two heptamers result in being sizably blue-shifted when compared with the ones obtained on the tetramer. This shift at higher energies comes from the level of calculation employed (TDA) rather than from an electronic effect related to the increased size, as will be discussed in Section 2.2.3.

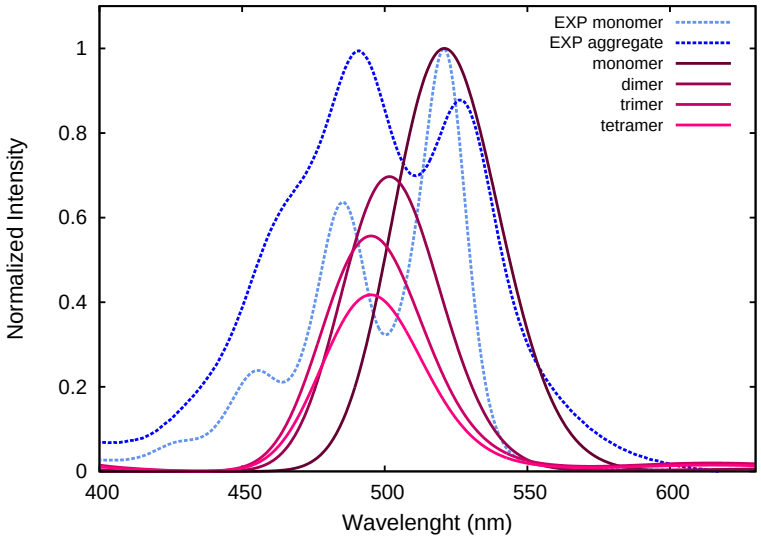

Figure 2.6: Calculated (full lines) and experimental (dashed lines) absorption spectra of the PDI monomer and "helix-like" aggregates. The calculations have been performed at the B3LYP/6-31G* level of theory in implicit (C-PCM) water.

System	E_{MAX} (eV)	oscillator strength	CT numbers	Participation Ratio (PR)
monomer	2.38	0.902		
dimer	2.47	1.340	0.035	2.00
		Helix-Like		
trimer	2.50	1.096	0.216	2.17
tetramer	2.54	1.235	0.236	3.21
heptamer	2.72	3.753	0.125	4.98
	2.77	2.429	0.118	5.76
		Alternated Type		
trimer	2.52	1.667	0.075	2.50
tetramer	2.55	2.127	0.072	3.53
heptamer	2.81	6.147	0.126	6.08
aggregate (exp)	2.53			

Table 2.2: B3LYP Vertical Excitation Energies in eV (E_{MAX}), Oscillator Strengths, CT Numbers, and PR Values computed at B3LYP/6-31G* level for the PDI Monomer and Its Aggregates, Namely, Dimer, Trimer, Tetramer, and Heptamer

Also, the computed oscillator strengths at the TDA level of theory are not comparable to the ones obtained from the TD-DFT, as TDA does not satisfy the Thomas-Reiche-Kuhn sum rule. We thus consider these results on the heptamer aggregates only to gain information about the trend of the CT and PR indices as

the size of the aggregate increases. Concerning the Excited-State topology analysis of the dimer, trimer, tetramer, and heptamer, the CT values are rather low, especially for the dimer, pointing toward localized Frenkel bright states. Even if the excitation energy of the first bright state is scarcely affected from the considered aggregation geometries (namely, the "helix-like" or "alternated-type"), the exciton analysis of the two systems shows relevant differences (Table 2.2). Indeed, when the "alternated-type" geometries are considered, the CT is strongly reduced (lower CT numbers), whereas the delocalization of the excitation involves more fragments (higher PR values), with a maximum of ~ 6 units in the case of the "alternated-type" heptamer. Notably, the PDI heptamer arranged in "helix-like" structure promote the presence of two quasi-degenerate Frenkel type states involving ca. 5 and 6 PDI units, respectively.

This analysis allows us to quantify and model the effect of the geometrical arrangements on the exciton properties as well as on the nature of the Excited State, even when considering equilibrium geometries only. On the basis of these findings, one could expect a significant impact on the exciton nature and delocalization due to the inclusion of finite temperature effects, as we will discuss in the next sections by analyzing the results of the MD simulations.

2.2.3 MD simulation

Before proceeding with the following analysis, it is useful to recall that, especially in the case of the large-sized aggregates, it is preferable to describe the Excited States using the less expensive TDA approach and to switch from a hybrid functional to a long-range-corrected one to avoid the sizable underestimation of long-range CT states. However, we found for both B3LYP and CAM-B3LYP a systematic blue shift in absorption maxima due to the use of TDA (ca. 0.2 to 0.3 eV).[85] On the other hand, this is, overall, compensated by the red shift obtained using the FF-based geometries (ca. 0.2 eV) and the COSMO solvation scheme and neglecting the terminal chains. Considering, however, that our goal here is getting insights into the nature and delocalization of the exciton as well as analyzing the topology of low-energy CT states along the MD simulations rather than reproducing the position of the experimental absorption maximum of the aggregates, we prefer the

use of CAM-B3LYP for the TDA calculations, even if it is noticeably blue-shifted, because it delivers the right order of bright and CT states. Indeed, as pointed out by the Dreuw group, CAM-B3LYP provides better transition density matrices even if the excitation energies are of lower quality compared with B3LYP.[86]

Monomer

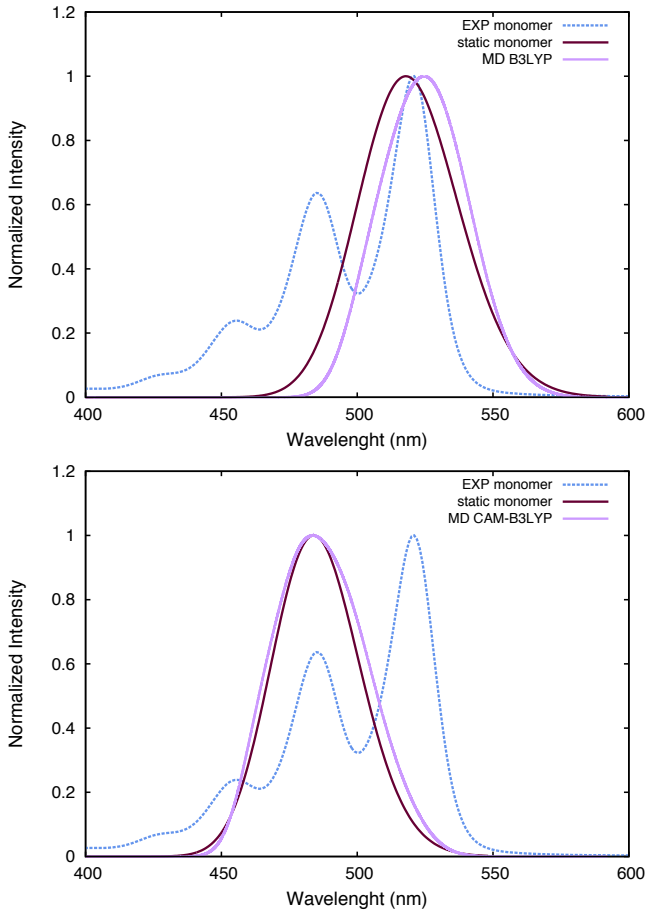

Figure 2.7: Calculated B3LYP (top panel) and CAM-B3LYP (bottom panel) static (brown full line) and CEA-VE (violet full line) absorption spectra of the PDI monomer compared with the experimental one (light-blue dashed line). A fwhm of 0.1 eV has been used for the convolution.

In Figure 2.7 we report the absorption spectrum of the PDI monomer obtained

as the convolution of the vertical transitions obtained from 100 MD snapshots. As compared with the absorption maximum obtained from the static description and due to the rigidity of the perylene core, the CEA-VE spectrum is almost unaffected, with a deviation of < 0.1eV for both B3LYP and CAM-B3LYP; however, as expected, the band is globally broader. Finally, we note that the classing sampling of the Ground State conformational shape, as expected, is not able to reproduce the observed vibronic secondary band, which requires the explicit calculation of the Franck-Condon factors to take into account the coupling between electronic and vibrational quantum states.[87, 88]

Tetramer

In Figure 2.8, we report the distribution of the dihedral angles and of the center-of-mass distances between consecutive units of the tetrameric aggregates. During the MD runs the PDI aggregates structure experienced deviations from the helicoidal ideal structure; indeed, one can observe an interconversion between the two conformations namely the "helix-like" and "alternated-type" proceeding through quite persistent intermediate states ("mixed-type"). On the contrary, and coherently with the high stacking energies (Figure 2.5), the center-of-mass distance of consecutive units experiences negligible variations along the MD simulation, remaining close to 3.5 Å.

The CAM-B3LYP CEA-VE spectrum is reported in Figure 2.9 compared with the static one obtained on the FF-optimized tetramer (top panel). One can note that once again the inclusion of thermal motion effects induces only a negligible red shift of the absorption maximum. Indeed, as shown for the equilibrium structures, the effect of the different conformations, that is, helical alternated or mixed, on the maximum wavelength is absolutely negligible. However, thermal agitation should be analyzed in terms of the effects it produces on the exciton wave function and, in particular, on the exciton delocalization length, which can, in turn, strongly alter the photophysical properties of the aggregates.

To analyze the exciton properties, we computed the CT numbers and the PR values of each Excited State on top of the snapshots extracted from the MD trajectory. Their distributions are displayed in Figure 2.10. The distribution of PR

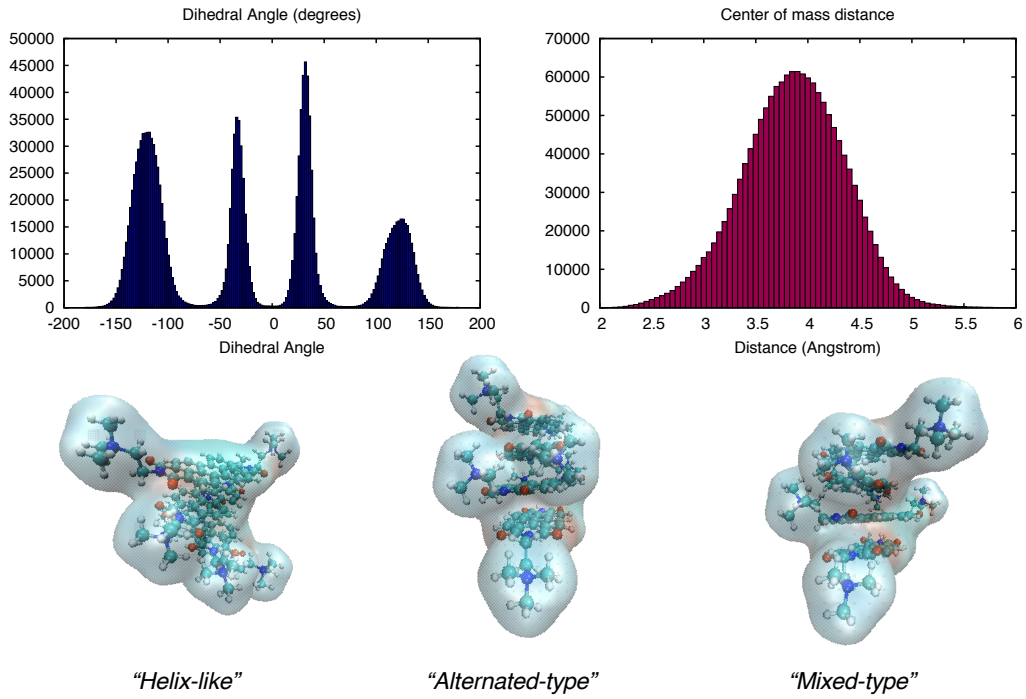

Figure 2.8: Distributions of the dihedral angle between a couple of PDIs (top-left) and of the center-of-mass distances of consecutive PDI units (top-right) obtained from the whole MD production run of the tetramer together with representative snapshots (bottom). Note that the asymmetry with respect to zero can be ascribed to the convergence of the statistical sampling only.

values presents a sharp peak at value of 1, which is indicative of the monomer-like states obtained at high excitation energies. However, the distribution also presents a rather broad but evident maximum peaked around PR of 2.0. Hence, we can see that bimolecular excitons, that is, Excited States delocalized on two PDI units only, are also highly probable. The PR distribution, however, goes to zero quite rapidly for values > 2.5 and is practically zero close to 4.0. This aspect implies that only very few Excited States will present excitons delocalized over the whole aggregate, and even the ones spread over three units will be quite rare. The topological analysis can be completed by taking into account the emergence of CT states (bottom panels in Figure 2.10). We can observe that most of the states will be quite local, as the broad maximum of the CT distribution centered around 0.3 indicates. However, a number of states characterized by an almost

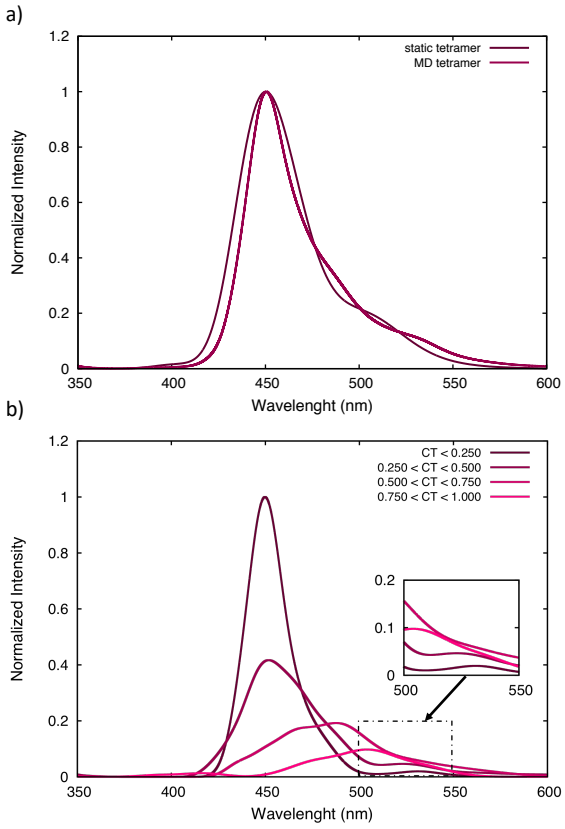

Figure 2.9: Calculated (TDA-DFT CAMB3LYP/6-31G*) CEA-VE spectra of the PDI tetramer in water (brown) compared with the static one (violet) obtained at the same level of theory on the FF minimized structure of the tetramer. (b) Decomposition of the PDI tetramer spectra taking into account only states having specific Charge Transfer character (CT index).

total charge separation (CT ca. 0.9 to 1.0) appears, as indicated by the strongly peaked maximum. Interestingly, even if those high CT states will be characterized by very low oscillator strengths, they appear at rather small excitation energies, and hence they might be populated during the photophysical evolution of the excitonic manifold and could lead to important properties concerning the interfacial charge generation properties of PDI-sensitized devices. Indeed, the accumulation of the CT states at the red edge of the absorption band can be confirmed by Figure 2.9b, in which the calculated CEA-VE spectrum is decomposed in terms of states having specific CT indexes.

Figure 2.10: CT numbers and PR values computed from the TDA calculations obtained from MD frames of the PDI tetramer. In the left column are reported the analyses for all of the calculated states, and in the right column are reported the analyses for all of the states having an excitation energy equal to or lower than the brightest state.

Heptamer

Similar considerations also apply for the larger heptamer-PDI aggregate, even though the dynamics is obviously more complicated, notably spanning a much more complex conformational space. The distribution of the dihedral angle between two contiguous units is reported in Figure 2.11, together with the illustration of some representative snapshots extracted from the MD trajectory. The main thermal motion of the PDI units is due to the coupled and simultaneous movement of chunks of monomers, from two to four units, that undergo a concerted rotation, hence producing local inhomogeneity, and the coexistence of helical and alternated regions inside the column ("mixed-type" structures). The CEA-VE spectrum, reported in Figure 2.13, presents similar characteristics to the ones evidenced by the

tetramer. However, the tetramer CEA-VE spectrum results more intense at lower energy compare to the heptamer case reflecting the presence of less delocalized Excited States. Both the weak effect of the aggregate size and the peculiar con-

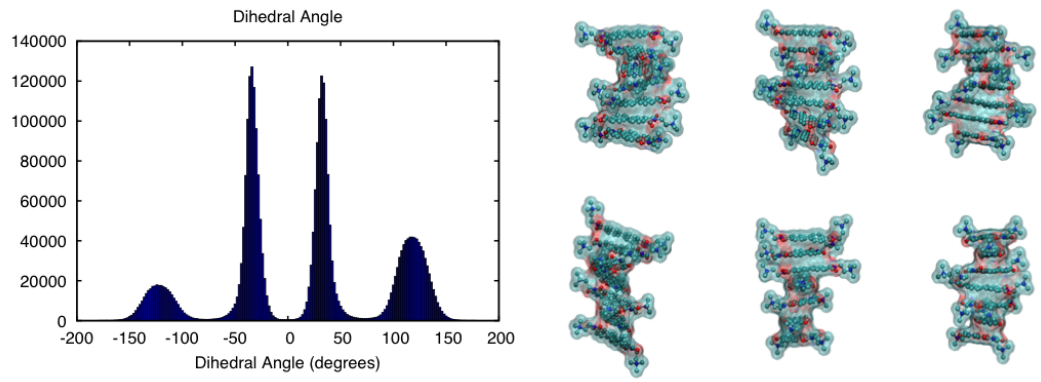

Figure 2.11: Dihedral angle between each couple of PDI for the heptamer aggregate (left panel) and some representative snapshots extracted along the MD trajectory (right panel).

certed rotation of chunks of PDI can be rationalized considering the topology of the observed Excited States (Figure 2.12). Indeed, the distribution of the PR values presents an important accumulation of entries in the region comprised between 1 and 2, hence suggesting an important presence of monomer-like and bimolecular excitons. Furthermore, and again in agreement with the tetramer case, even if a secondary maximum centered around 3 is evident, the distribution goes to 0 rapidly for PR values close to 5. Hence, we can safely conclude that even in the heptamer case only very rare occurrences of exciton length larger than four to five units will be observed, whereas no exciton state delocalized over the entire aggregate can be evidenced. As far as the nature of Excited States is concerned, once again, very similar considerations to the ones drawn for the tetramer hold, and the majority of states and, in particular, the brightest one present a pronounced local character. However, we may still evidence the presence of low-energy CT states showing an almost total electron separation involving two PDI units and accumulating at the red edge of the absorption spectrum, as evidenced in Figure 2.13b.

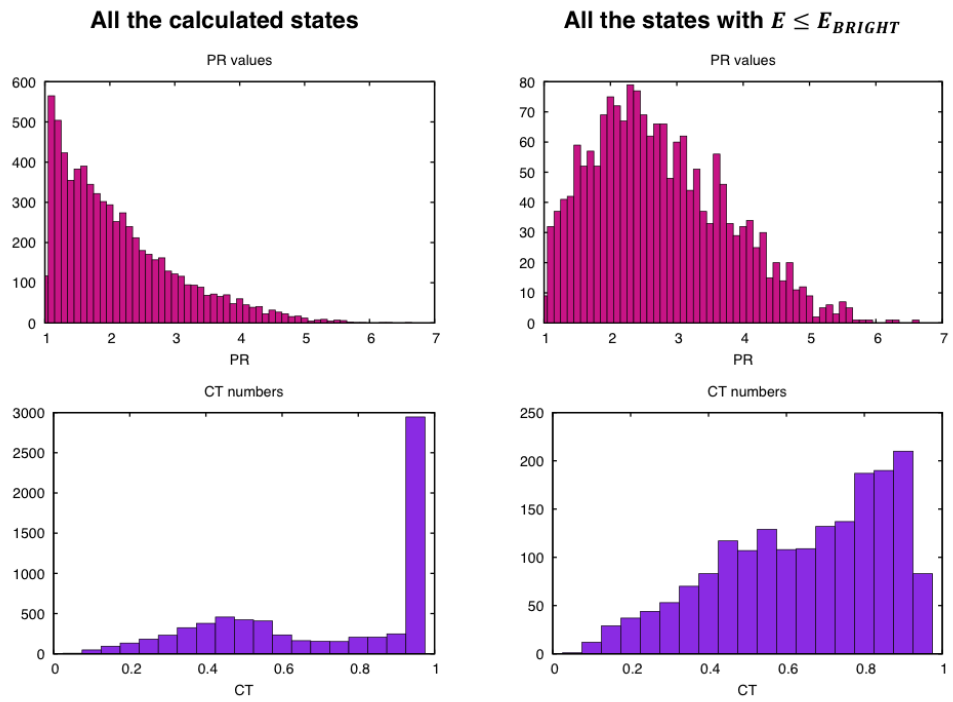

Figure 2.12: CT numbers and Participation Ratio (PR) values computed from the TDA calculations obtained from MD frames of the PDI heptamer. In the left column are reported the analyses for all of the calculated states, and in the right column are reported the analyses for all of the states having an excitation energy equal to or lower than the brightest state.

Overall, our findings are consistent with the experimental conclusions drawn by Kim and coworkers[48] on perylene bisimide helices composed of 10 units, indicating an initial delocalization of the Frenkel-type exciton on three monomeric units. Indeed, our results confirm that because of the combined effect of electronic and thermal factors, PDIs are unable to produce strongly delocalized excitons; as a consequence, the most probable coherent electron or energy-transfer phenomena will involve at a maximum four to five units. Hence the preparation of larger-size π-stacked aggregates will most probably not be strongly beneficial in enhancing PDI photophysical and charge-transport properties.

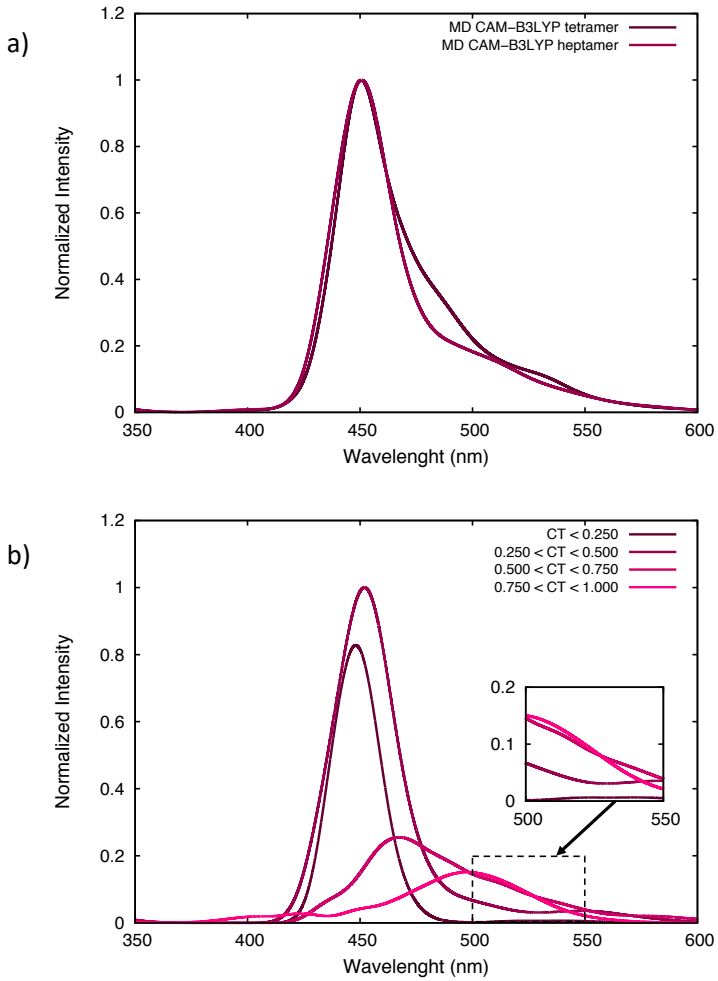

Figure 2.13: a) Theoretical spectra of the PDI tetramer and PDI heptamer at the TDA-DFT CAM-B3LYP/6-31G* level of theory in water (COSMO) obtained from the convolution of 100 TDA-DFT calculations from as many snapshots randomly extracted from the PDI MD production runs. b) Decomposition of the PDI heptamer spectra taking into accounts only states having specific Charge Transfer character (CT index).

2.2.4 Final Remarks

In this section, we have deeply analyzed the optical properties of PDI aggregates by combining quantum-chemistry methods and classical Molecular Mechanics. In particular, we have confirmed the capacity of PDI π-stacked H-aggregates to give

rise to delocalized excitonic wave functions. The effects of thermal motion on the shape and position of the absorption spectrum are, however, negligible, in the case of both the monomer and the aggregates. Even if not evident in the optical properties, the effect of thermal motion is crucial in dictating the global properties of the aggregate's Excited-State manifold. In particular, the peculiar large-scale motion observed in the aggregate MD and characterized by the concerted and simultaneous rotation of chunks of the PDI column prevents the formation of strongly delocalized excitons. In fact, even in the case of longer helices, the exciton delocalization almost never exceeds five PDI units, confirming recent experimental observations.[48] Even if the delocalization of the Frenkel exciton state is, however, not extremely large compared with similar self-aggregate materials, one should evidence the presence of a dark but low-lying CT Excited State leading to a full electron-hole separation between two units that, hence, can be efficiently exploited to optimize charge separation and transport in PDI-based optical devices.

2.3 Vibronic features of PDI spectra through a mixed quantum-classical scheme

In the last two decades several time-independent [88–92] and time-dependent (TD) [93–98] methods have been proposed to compute fully quantum spectra, but for large systems they basically rely on harmonic approximation for the potential energy surfaces and therefore they are suited for rigid systems rather than for flexible ones.[88–93, 96, 97] On these grounds, a number of Mixed Quantum Classical (MQC) approaches, where quantum and classical refers to the way the nuclear motion is treated, have been proposed.[47, 99–103] The "Adiabatic Molecular Dynamics generalized Vertical Hessian" ($Ad-MD|gVH$)[47] approach was very recently introduced and is aimed to simulate the electronic spectra of flexible dyes in condensed phase, yet preserving their vibronic features. At variance with most of the other approaches, [100–102, 104] rather than adopting the standard solute-solvent partition scheme, the $Ad-MD|gVH$ method is based on differentiating the nuclear Degrees of Freedom in stiff and soft modes, and assuming that the former modes are much faster than the latter (Adiabatic hypothesis). In this framework, the spectrum can be rigorously obtained as an average of configuration-specific vibronic spectra, computed along the MD trajectory sampling a selected set of large amplitude soft modes. For dyes with negligible inter-state couplings, each vibronic spectrum might be retrieved by means of the gVH approach,[47] a generalization of the Vertical Hessian model. [105, 106] Conversely, in order to be able to deal with spectra of molecular aggregates $Ad-MD|gVH$ needs to be generalized substituting the engine that computes the spectra, i.e. the gVH approach, with a methodology able to account for strong inter-state couplings.

Before any attempt to generalize the theoretical framework to obtain an accurate description of the vibronic spectra of large-sized self-assembled PDIs, it is necessary to extensively investigate the protocol performances for monomers in solution. To this end, two points require, in our opinion, particular attention: (a) the capability of the adopted FF to properly describe both the rigidity of PDI core and the flexibility of its lateral chains (which are expected to play an important role in the aggregation mechanism), and, (b) the accuracy of the

$Ad-MD|gVH$ method in combination with the selected FF in properly reproducing the well-resolved vibronic structure of the spectrum of a solvated PDI monomer. The $Ad-MD|gVH$ method will be therefore applied here in combination with a molecule-specific QM derived FF (QMD-FF), to obtain the absorption spectrum of the PDI in Acetonitrile (ACN), eventually validating the results through the comparison of the computed spectra with their experimental counterparts.[5]

Besides setting up a sound MQC protocol to successively tackle vibronic spectra of large π-aggregates in solution, this project was also the occasion to present an extensive evaluation of the performance of a number of different techniques, designed to reproduce spectral shapes of flexible molecules, whose interest goes beyond the specific PDI system. In order to perform such an extended analysis, we designed a computational protocol that is schematically displayed in Figure 2.14. More in detail, we will first compare the predictions of our QMD-FF, parameterized on the basis of Density Functional Theory (DFT) data specifically computed for the target PDI, to the results of the GAFF FF, investigating the differences in terms of the sampled configurational space and its consequences on the prediction of purely-classical CEA-VE absorption spectra. To have a reference to compare with and assess the FFs capability in delivering a reliable description of the monomer structure and dynamics, we also performed calculations in Gas Phase, benchmarking the results with those obtained by an Ab Initio MD (AIMD) simulation. Next, we investigate the difference among the two MD and the AIMD samplings, when combined with the $Ad-MD|gVH$ method to account for vibronic progressions. Finally, we compare the MQC predictions, which account for the solvated PDI dynamics, with the results of a standard "static" approach, based on vibronic calculations carried out upon harmonic approximation on a single optimized PDI conformer, accounting for the solvent with a Conductor-like Polarizable Continuum Model (C-PCM).[65] This Section is organized as follows: after a description of the MQC protocol (Subsection 2.3.1), we give the computational details in Subsection 2.3.2 and discuss all results in Subsection 2.3.3; our final remarks are finally drawn in Subsection 2.3.4.

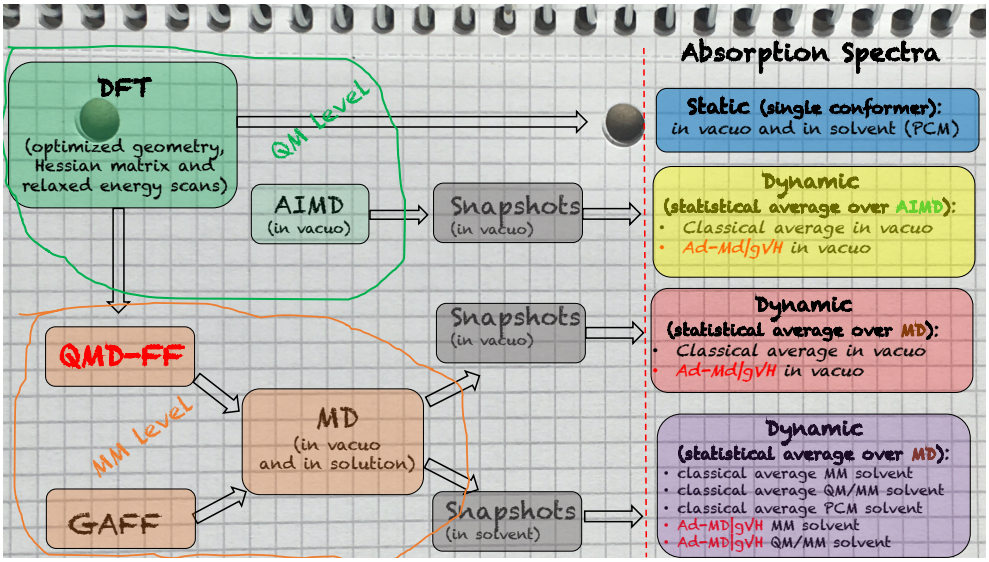

Figure 2.14: Flow chart of the MQC approach presented in this work: the integration of QM (green) and CL (MM, orange) techniques leads to the simulation of absorption spectra (right panels) at different level of complexity, thus allowing to unravel selected effects acting on spectral shape, as the system dynamics, the presence of the solvent or the vibronic features. The key ingredients for the most complete description, i.e. the accurate and specific QMD-FF and the recently proposed $Ad-MD|gVH$ method, are highlighted in red.

2.3.1 Methods

The MQC protocol

The MQC protocol used here consists in the hierarchical integration of different QM and MM techniques: a QMD-FF parameterization of the target solute based on QM data, MD simulations carried out with the resulting FF and, eventually, the calculation of the absorption spectra along the MD sampled trajectories. Extensive MD runs, either in Gas Phase or solution, are then carried out exploiting the QMD-FF, to accurately sample PDI's conformational space through a reliable collection of system snapshots. Finally, the absorption spectra is obtained by applying the $Ad-MD|gVH$ method over the aforementioned frame collection as described in

the following. In a TD formalism, the general QM expression of the absorption lineshape $L^{QM}(\omega)$ from an initial electronic state i to a final one, f, is

$$L^{QM}(\omega) = \frac{1}{2\pi Z_{v_i}} \int \mathrm{Tr}\left[\boldsymbol{\mu}_{if} e^{-itH_f/\hbar} \boldsymbol{\mu}_{fi} e^{-(\beta - it/\hbar)H_i}\right] e^{i\omega t} dt \tag{2.1}$$

H_i and H_f are the Hamiltonians for the i and f states, $\boldsymbol{\mu}_{if}$ their transition electric dipole moment (with $\boldsymbol{\mu}_{if}$=$\boldsymbol{\mu}_{fi}$) and Tr denotes the trace operation. $\beta = (K_B T)^{-1}$, where K_B is the Boltzmann constant, T the absolute temperature, and Z_{v_i} is the partition function of the initial vibrational states. From equation 2.1, it is possible to obtain a CL approximation to the spectrum, $L^{CL}(\omega)$, in two steps. First, following Lax[107], we neglect the commutators between the Hamiltonians H_i and H_f and with the operator $\boldsymbol{\mu}_{if}$,[47] and, second, the quantum distribution of the system in the initial electronic state, $\rho_i^{QM}(\mathbf{Q}, T)$, is approximated with its CL analogue, $\rho_i^{CL}(\mathbf{Q}, T)$, which can be sampled along the MD trajectory.[47] In this way we obtain the CEA-VE spectral lineshape

$$L^{CL}(\omega) = \frac{1}{N_{con}} \sum_{\alpha} |\boldsymbol{\mu}_{if}(\mathbf{Q}^{\alpha,CL})|^2 g\left(\omega - \Delta\Omega(\mathbf{Q}^{\alpha,CL})\right) \tag{2.2}$$

where g is a linewidth function, in condensed phase usually a Gaussian, whose width can be set to account phenomenologically for a number of effects missing in the model (like the quantum nature of the nuclear motion).

To obtain the MQC spectral shape, $L^{MQC}(\omega)$, we resort, as stated above, to the $Ad-MD|gVH$ method.[47] According to this model, all nuclear Degrees of Freedom (DoFs) of the solute+solvent system can be separated in two categories: the stiff modes, $\mathbf{r}$, pertaining to the dye (and to a number of selected solvent molecules, if required), and the soft modes, $\mathbf{R}$, represented by the flexible DoFs of the dye together with all the remaining environmental modes. The former $\mathbf{r}$ set is handled at QM level, while the $\mathbf{R}$ collection is treated at CL level. Concretely, as for the CEA-VE spectra, the CL configurational space $\rho_i^{CL}([\mathbf{R}, \mathbf{r}], T)$ is first sampled through a representative number N_{con} of MD snapshots ($\mathbf{R}^{\alpha}$,$\mathbf{r}^{\alpha}$). Next, in order to (re-)introduce a QM vibronic treatment of the stiff-coordinates $\mathbf{r}^{\alpha}$, we invoke an adiabatic approximation, thus assuming that $\mathbf{R}$ coordinates are much slower than stiff ones, which can hence rearrange very quickly to any $\Delta\mathbf{R}$ displacement,

so that the soft $\mathbf{R}$ coordinates can be considered frozen at each sampled frame α. This allows us to build, at each α, reduced-dimensionality harmonic Potential Energy Surfaces (PESs) along the stiff-coordinates, for the initial ($V_i(\mathbf{r};\mathbf{R}^\alpha)$) and final-state ($V_f(\mathbf{r};\mathbf{R}^\alpha)$). In order to define $V_k(\mathbf{r};\mathbf{R}^\alpha)$ (k=i,f), at each α snapshot we compute with a QM/MM scheme the energy gradient and Hessian of the initial and final state for a subset of the system coordinates, comprising all dyes atoms and a first layer of environment molecules. Soft modes are projected out moving to a set of redundant curvilinear internal coordinates[106, 108] and applying iteratively proper projectors. Further details can be found in Ref. [47]. $V_i(\mathbf{r};\mathbf{R}^\alpha)$, and $V_f(\mathbf{r};\mathbf{R}^\alpha)$ PESs can be eventually exploited to compute, through equation 2.1, a vibronic quantum spectrum $L_\alpha^{QM,\mathbf{r}}(\omega)$, which involves the fast coordinates $\mathbf{r}$ only, and is specific for each sampled CL configuration $\mathbf{R}^\alpha$. Then, $L^{MQC}(\omega)$ then is simply the average of all the reduced-dimensionality vibronic spectra, $L_\alpha^{QM,\mathbf{r}}(\omega)$. [47]

$$L^{MQC}(\omega) = \frac{1}{N_{con}} \sum_\alpha L_\alpha^{QM,\mathbf{r}}(\omega) \tag{2.3}$$

Finally, it might be worth mentioning that the MQC equation 2.3 and the CL one (2.2) are formally very similar. The fundamental difference is that the phenomenological lineshape g, required by the CL lineshape $L^{CL}(\omega)$ and with the same Gaussian shape for each sampled configuration α, is substituted in $L^{CL}(\omega)$ by the α-specific $L_\alpha^{QM,r}(\omega)$, i.e. without introducing any phenomenological factor.

2.3.2 Computational Details

MM calculations

Two different FFs have been tested in this work. The first FF is a QMD-FF, parametrized with respect to the DFT data for the isolated PDI molecule. In particular, all intra-molecular PDI's parameters were obtained with the JOYCE code [109–111]. Further details about the parameterization are included in Appendix A. The LJ parameters entering the PDI's intermolecular term (A.4) were instead transferred from the OPLS libraries as implemented in the GROMACS5.1 package,[112] whereas the point-charges were obtained through the RESP protocol by using the Antechamber suite.[68] Finally, for consistency with the PDI intermolec-

ular parameter set, all ACN and Cl^- parameters were also taken from the OPLS FF.

The second FF is the generalized AMBER Force Field (GAFF) that was already discussed in the previous section. The GAFF topology files were here transformed into GROMACS-type files by exploiting the ACPYPE - AnteChamber PYthon Parser interface program in order to have a trustful comparison with the QMD-FF which has been built in Gromacs format. All PDI's intermolecular FF parameters, and those concerning the solvent (ACN) and the counter ion (Cl^-) where also transferred from GAFF. [113]

Classical MD simulations for both the isolated PDI molecule in Gas Phase (GP) and the solvated system in ACN solution (PDI@ACN) were performed by exploiting the GROMACS5.1 Engine.[112] In GP, both FFs have been employed in the NVT ensemble for 10 ns, by imposing a timestep of 0.1 fs and a temperature of 300 K, through the use of the Berendsen thermostat[114]. Turning to condensed phase, a PDI@ACN system, composed of the PDI solute, two Cl^- counterions, and $\sim$ 1000 ACN molecules, was initially minimized to remove bad contacts and thereafter thermally equilibrated for $\sim$ 2 ns at 300 K in the NVT ensemble. The final NPT production runs were carried out at 1 atm and 300 K through the Parrinello-Raman[115] and the v-rescale[116] schemes by using coupling constants of 0.1 ps and 1 ps respectively and applying periodic boundary conditions. Also for the simulations of the PDI@ACN we set the timestep to 0.1 fs and the cutoff radius for the Coulombic charge-charge and LJ terms to 11 Å whereas we accounted for the long-range electrostatics interactions by means of the particle mesh Ewald procedure.

All the MD trajectories were stored in sets of 100 α-conformations, equally spaced in terms of time, and used first to investigate the statistical behaviour of key structural parameters, and, next, to compute the final spectra.

QM calculations

QM static calculations were carried out with GAUSSIAN16[117] package, whereas the Terachem software[71–73] was employed for the GP AIMD run. For all the DFT/TD-DFT calculations discussed here the CAM-B3LYP functional[76] in com-

bination with the 6-31G* basis set was adopted. To obtain the data for the QMD-FF parameterization, the PDI molecule Ground State was fully optimized and the resulting geometry stored together with its Hessian matrix. The Grimme's Dispersion DFT-D3 correction [118] was also adopted: notwithstanding its effect is expected to be negligible on the isolated PDI monomer, reliably accounting for dispersion interactions may become decisive when investigating π-aggregates, which is the future prospect of our work. Additionally, a number of relaxed torsional energy scans were also carried out at the same level of theory, optimizing all coordinates except the scanned flexible chain dihedrals, δ_μ, entering in equation A.7. To partially screen the electrostatic repulsion of the lateral chains due to the +2 charge of the PDI molecule, both geometry optimization and relaxed scans were carried out in an implicit solvent adopting the Conductor-like Polarizable Continuum Model (C-PCM). [65] To retrieve the energy, gradients and Hessian matrix in initial (Ground) and final (Excited) PDI's electronic states, needed for the simulation of the vibronic absorption spectra within the $Ad-MD|gVH$ formalism, DFT and TD-DFT calculations were, respectively, carried out, either for the GP or PDI@ACN system, at each configuration extracted from the MD trajectories.

CAM-B3LYP/6-31G* AIMD simulations have been performed on the isolated PDI in GP starting from the optimized structure of PDI, which has been obtained at the same level of theory. The AIMD simulations have been conducted for 103 ps in the NVT ensemble, where the first 3 ps have been used for equilibration and hence discarded. We adopted a timestep of 0.1 fs and set the temperature to 300K, by using the Bussi-Parrinello Langevin scheme[119] and imposing a damping time of 200 fs. In the following, the AIMD trajectory will be labeled as "DFT".

Absorption Spectra

Embedding schemes

Absorption spectra were computed for both the isolated monomer and the solvated PDI@ACN system. For the former system, GP MD (GAFF and Joyce) and AIMD (DFT) trajectories were employed. Conversely, to account for the embedding effects, several protocols of increasing complexity were applied to each MD snapshot extracted from the PDI@ACN runs:

i) **C-PCM**: All the ACN molecules and Cl^- counterions are removed from each frame, and the solvent effects accounted for at C-PCM level, considering ACN and the less polar diethyl ether.

ii) **EEpc**: Following an Electronic Embedding (EE) scheme, all the solvent molecules and counterions within a large cut-off radius of 20 Å from the PDI center of mass are included in the calculation as point-charges (pc).

iii) **QM/MM/EE**: The embedding environment is included according to a mixed QM/MM/EE scheme, where the QM/MM model was built according to the ONIOM approach, considering the solute in the model system (high layer) and by including the first solvation shell into the real system. The latter is described at MM level making use of the same parameters obtained for the GAFF or JOYCE FFs. Finally, the EE scheme consisted as usual in including all ACN and Cl^- atoms within the large 20 Å radius as point charges.

iv) **QM/EE**:The solvent molecules and the counterions are treated using a mixed QM/EE approach, for which the solvent molecules of the first solvation layer (within a 4 Åradius) are explicitly included in the KS Hamiltonian, while the remaining solvent molecules, within a 20 Å radius, are included as point charges.

CEA-VE spectra

CEA-VE spectra are obtained, for both GP and PDI@ACN systems, by computing the vertical transition energies and intensities over the 100 snapshots sets extracted either from the GAFF, JOYCE or DFT trajectories. The final spectral shape is retrieved according to equation 2.2, using a phenomenological convolution with Gaussian functions having a fwhm of 0.1 eV. For the solvated system, **C-PCM**, **EEpc**, **QM/MM/EE**, and **QM/EE** schemes were separately employed for both FFs.

Ad – MD|gVH spectra

All the configuration-specific vibronic spectra, necessary for the $Ad-MD|gVH$ calculations, have been obtained for both GP and PDI@ACN systems in Franck-Condon approximation, with $\mathcal{FC}classes$3.0, [120, 121]. For each snapshot, the code computes the vibronic spectrum at 300 K with the TD formulation. [93–98, 122] To this end it reads energies, gradients, and Hessians of the initial and final electronic states computed over the snapshot sets, and builds up the reduced dimensionality gVH model by projecting out the soft modes. The spectra for the different snapshots are then averaged to obtain the final $Ad-MD|gVH$spectrum according to equation 2.3. It accounts explicitly for possible broadening mechanisms, like the inhomogeneous one, hence, in principle, it does not require the adoption of any phenomenological Gaussian. In practice, since the sum over conformations, α, is necessarily finite, the average arising from Eq. 2.3 may display some noise. Therefore, in order to compensate the limited conformational sampling and obtains smooth profiles, $L_r^{\alpha,q}(\omega)$ spectra are convoluted with a narrow Gaussian with fwhm=0.01 eV. As discussed in ref. [47], this procedure only removes the noise but does not alter the overall shape and width and of the spectrum. As far as the PDI@ACN system is concerned the solvation scheme **QM/MM/EE** was adopted since we recently demonstrate the necessity to use a three-layers set up in order to minimize the spurious imaginary frequencies. In particular, the LJ interactions, that are included in the treatment of the first solvation layer, were found fundamental to properly polarize the QM wave-function. The effect of the mutual solute/solvent polarization on the transition energies was accounted with a mixed approach in which vertical excitations are computed with the **QM/EE** scheme, including the first solvation shell in the QM region, while the first and second energy derivatives are obtained from the **QM/MM/EE** scheme. For sake of simplicity, in the context of vibronic spectra, in the following, we will refer to this mixed approach as **QM/EE**.

2.3.3 Results

PDI structure and dynamics

Depending on the relative orientation of the aliphatic side chains with respect to the perylene's plane, DFT optimizations indicate the presence of two possible minima, corresponding to the *syn* or to the *anti* conformer (left a) panel in Figure 2.15).

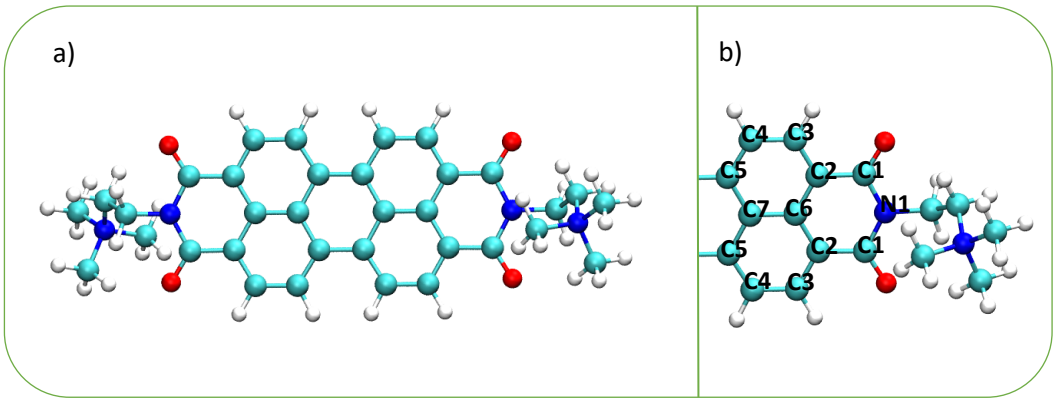

Figure 2.15: a) DFT optimized structure of the PDI *anti*-conformer; b) Atom labels used in QMD-FF parameterization for the PDI aromatic core.

These isomers are almost degenerate, with an energy difference of ~ 0.1 kJ/mol, and, besides the relaxed scans, only the Hessian matrix of the *anti* conformer was considered to build the QMD-FF.

Figure 2.16 compares the torsional relaxed energy scans computed at DFT level with the corresponding MM scans, obtained by using either the GAFF or the JOYCE FF. As expected, the torsional profiles obtained by the QMD-FF better compare with DFT with respect to the ones calculated using GAFF. In particular, for δ_1 and δ_2, the most stable minima predicted by GAFF (90° and 180°, respectively) correspond to maxima (δ_1) or higher energy local minima (δ_2) of the QM torsional profile and, in general, the energy barriers between the different minima are underestimated, thus favoring the inter-conversion between the *syn* and *anti* conformers. To further gauge the quality of the two considered FFs, we analysed

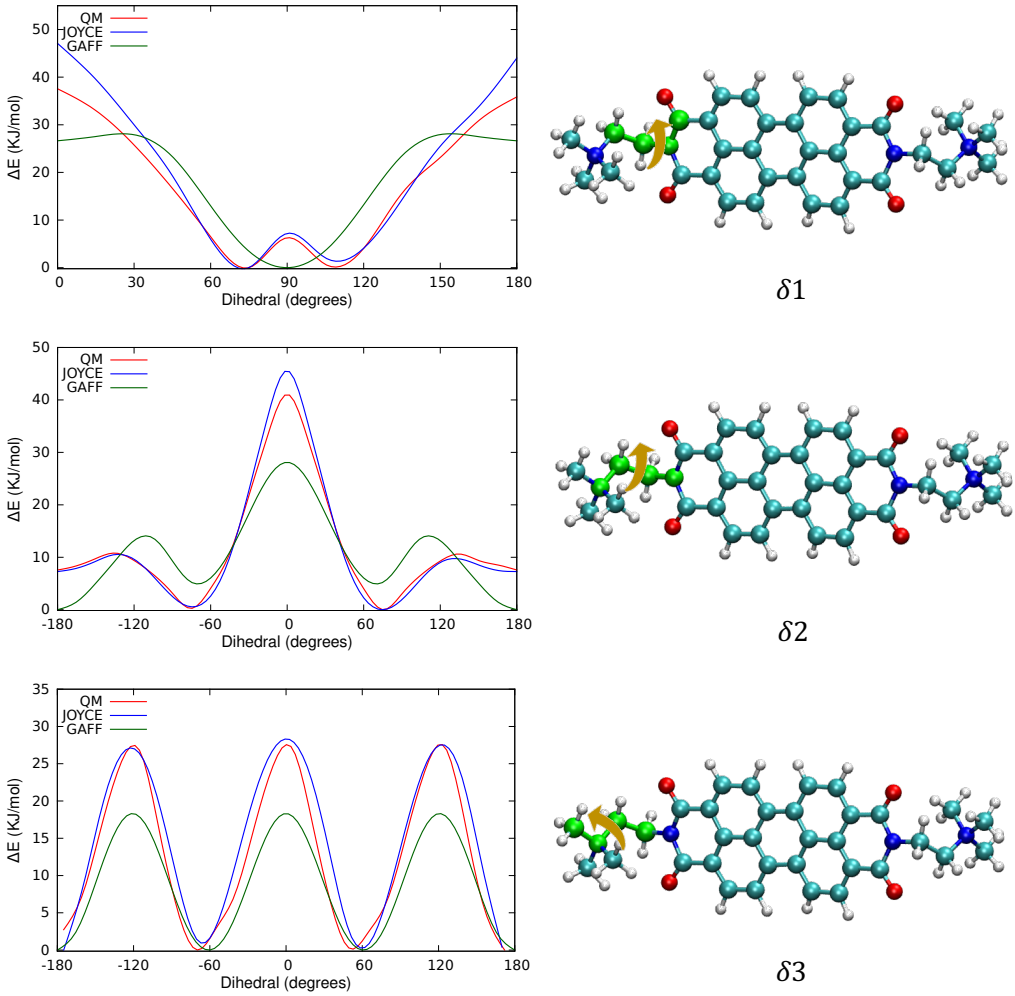

Figure 2.16: Comparison between QM torsional relaxed energy scans (red lines) and the relative MM relaxed profiles computed for the Joyce (blue) and the GAFF (green) FFs. Each of the monitored PDI's flexible dihedrals is evidenced in the right insets as a orange arrow, and the heavy atom quadruplets used for their definition highlighted in green.

the first 100 ps of the classical MD trajectories in GP, in comparison with the reference AIMD run. The conformational changes, sampled every 0.1 ps, have been monitored by considering the most relevant bond lengths of the PDI conjugated core (Table 2.3) and the flexible chain dihedrals (Figure 2.17). While the former are important for the accurate prediction of the absorption spectrum, as the $S0 \rightarrow S1$ transition is localized on the planar perylene core, the distribution of the flexible dihedrals along the MD runs is expected to be crucial in dictating the

self-aggregation properties. Data in Table 2.3 show an overall good match between the JOYCE and the DFT distributions, whereas GAFF predicts less accurate bond lengths, especially for the C5-C5 and the N1-C1 bonds (see Figure 2.15 for label definition), where significant differences around 0.05 Å are found.

	DFT	JOYCE	GAFF		DFT	JOYCE	GAFF
N1-C1	1.407 ± 0.029	1.399 ± 0.031	1.360 ± 0.024	C5-C5	1.476 ± 0.029	1.473 ± 0.030	1.412 ± 0.023
C1-C2	1.476 ± 0.029	1.473 ± 0.032	1.498 ± 0.028	C2-C6	1.417 ± 0.025	1.413 ± 0.027	1.393 ± 0.024
C2-C3	1.379 ± 0.024	1.377 ± 0.027	1.392 ± 0.025	C6-C7	1.420 ± 0.026	1.419 ± 0.030	1.409 ± 0.023
C3-C4	1.401 ± 0.026	1.398 ± 0.026	1.391 ± 0.025	C5-C7	1.429 ± 0.026	1.428 ± 0.028	1.412 ± 0.024
C4-C5	1.389 ± 0.024	1.387 ± 0.026	1.407 ± 0.025				

Table 2.3: Bond lengths (Å) distributions and standard deviations computed from the PDI trajectories in vacuo, considering either MD ((GAFF or JOYCE) or AIMD (DFT) runs. The atom labels refer the ones defined for the JOYCE FF, shown in Figure 2.15

These discrepancies arise from the transferability requirements of the general purpose nature of the GAFF FF, where only three different atom types are used to describe the PDI core: one atom type for N, one for the carbon bearing the oxygen atoms (C) and one for the remaining carbon atoms. Evidently, this severely limits the capability of GAFF to account for different single (or double) bonds within the perylene core, with the inevitable consequence of the poor description of the bond length alternation with respect to the QM reference[123]. Conversely, as detailed in Figure A.1, a more specific atom type assignment can be adopted in the construction of the QMD-FF, in turn leading to the larger variety of stretching (and bending) parameters emerging from the comparison of the two FFs. As is apparent, despite the simplicity of the model harmonic function, JOYCE QMD-FF is able to reproduce the DFT distributions, indicating a negligible impact of the anharmonic effects.

Figure 2.17 shows the population distribution of the chain flexible dihedrals δ_1-δ_3 obtained with the two FFs and along the reference AIMD trajectory.

As suggested from the torsional energy profiles shown in Figure 2.16, the main lack of the GAFF trajectory in reproducing dihedral dynamics consists in predicting δ_1 in a wrong position, centered at $\sim 90°$ (instead of $\sim 75°/\sim 105°$, where the QM minima are located) and delivering for δ_2 an asymmetric distribution around $0°$. On the contrary, the δ_1 and , in particular, δ_2 QMD-FF distributions are more closely related to the QM profiles and torsional minima, even if the AIMD simulation seems to indicate lower potential barriers. These differences might arise

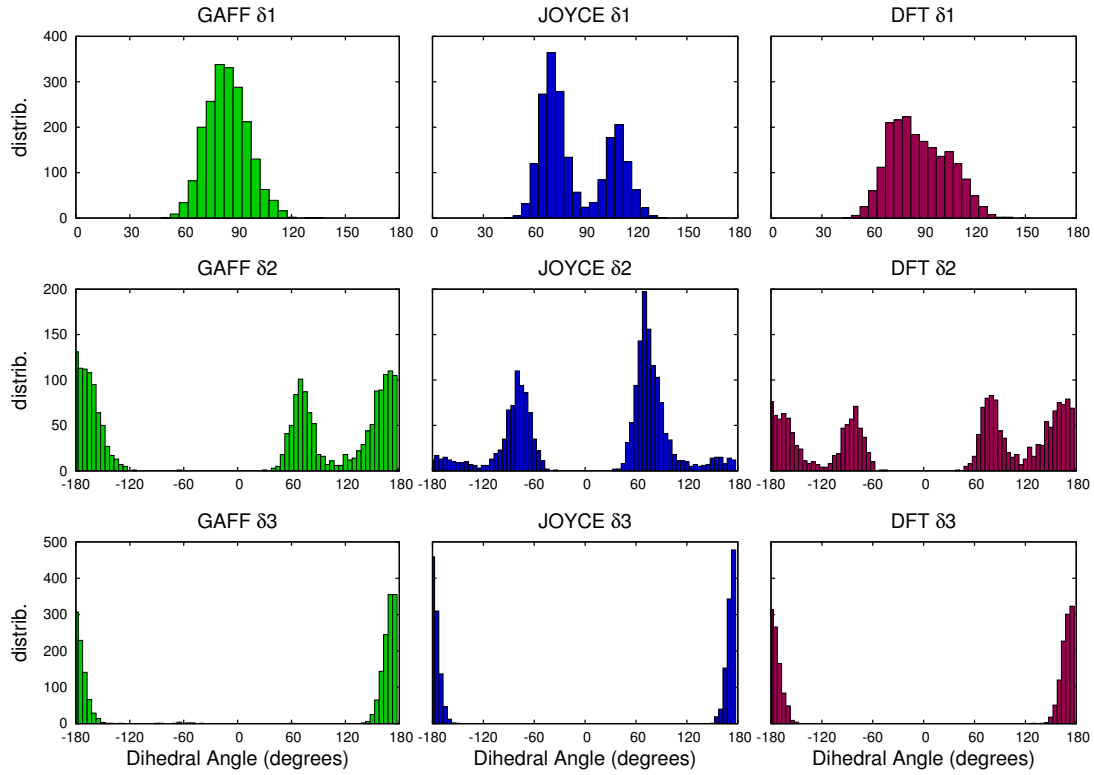

Figure 2.17: Dihedral distributions computed along the AIMD (DFT) and MD (GAFF, JOYCE) trajectories. The labels of the flexible dihedrals are given in Figure 2.16.

from the coupling between these torsions, which is neglected in both GAFF and JOYCE FF. MD simulations in solution (ACN) revealed even more remarkable

	JOYCE	GAFF		JOYCE	GAFF
N1-C1	1.400 ± 0.031	1.359 ± 0.024	C5-C5	1.472 ± 0.030	1.411 ± 0.023
C1-C2	1.473 ± 0.032	1.499 ± 0.027	C2-C6	1.411 ± 0.027	1.391 ± 0.023
C2-C3	1.375 ± 0.025	1.391 ± 0.024	C6-C7	1.418 ± 0.029	1.409 ± 0.023
C3-C4	1.397 ± 0.027	1.389 ± 0.024	C5-C7	1.426 ± 0.028	1.407 ± 0.023
C4-C5	1.385 ± 0.026	1.406 ± 0.024			

Table 2.4: Bond lengths (Å) distributions and standard deviations computed from the PDI@ACN MD runs considering the JOYCE and the GAFF FFs and by analyzing one conformation every 0.5 ps. The labels of the atoms involved in the analyzed bonds are given in Figure 2.15

differences between GAFF and JOYCE FFs. The comparison between the bond lengths distribution (Table 2.4) essentially confirm the results obtained in GP, be-

ing the stiff modes less sensitive to the solvent. The distributions of the flexible dihedrals are conversely expected to be more effected by the presence of the solvent. In particular, the exchange rate among different minima is usually higher in

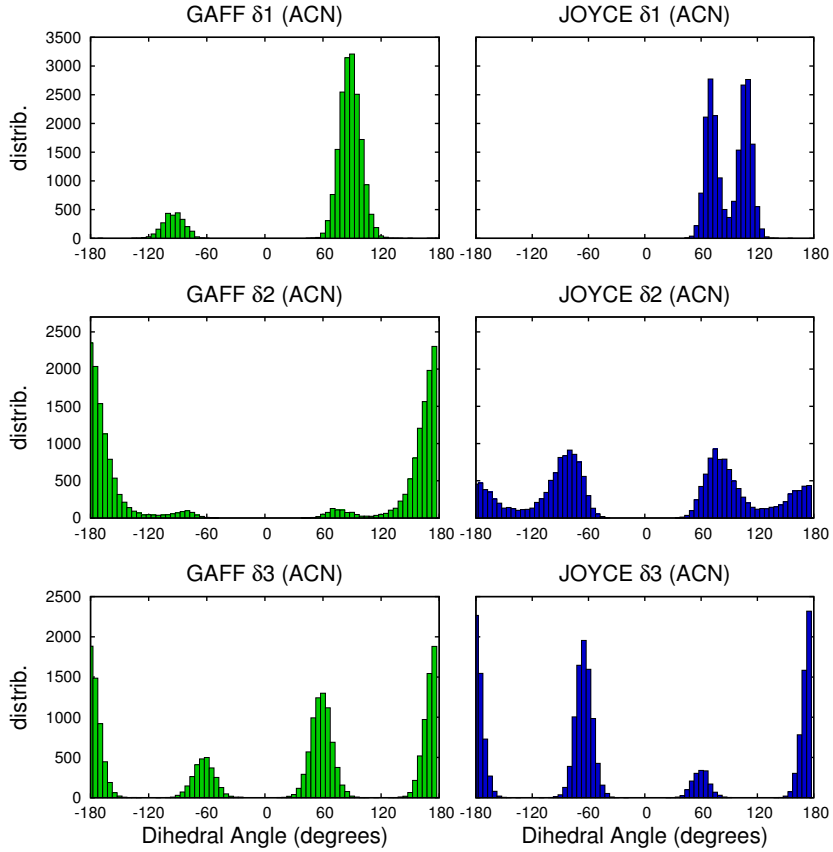

Figure 2.18: Dihedral distributions computed from the PDI@ACN MD runs by using the GAFF FF and the JOYCE FF. The labels of the flexible dihedrals are given in Figure 2.16.

solution compared to GP, because the interactions with the solvent might help in overcoming the energy barriers. For this reason, the δ_1-δ_3 population distribution, obtained for the PDI@ACN system with both FFs, is shown in Figure 2.18 along the whole $[-180° - 180°]$ range. As far as δ_1 is concerned, JOYCE FF yields two equally intense peaks centered at $\sim 75°$ and $\sim 105°$, in agreement with two degenerate minima revealed by the QM torsional profiles. On the contrary, as evident in the left top panel, GAFF FF is characterized by two peaks of different

intensity, centered at ± 90°, meaning that the molecule is visiting the *syn* conformation, as a consequence of the underestimated *syn*/*anti* inter-conversion barrier (see Figure 2.16). On the same foot, GAFF predicts the local minimum of the $\delta 2$ dihedral at 180° to be remarkably more overpopulated with respect to the real minimum at $\sim 75°$. The conformational analysis presented here, in line with the results obtained in GP, highlights the limitations that could arise from the blind use of a general purpose FF: both the bond length alternation within the perylene core and the flexibility of the side chains are poorly described, possibly delivering inaccuracies in the calculation of the optical and aggregation properties. In the following, we will discuss the first point, that is the accuracy of the absorption spectrum prediction, by using different levels of approximations.

Absorption Spectra

CEA-VE The three 100 ps trajectories (DFT, GAFF and JOYCE) have been sampled by extracting a configuration every 1 ps, computing, to build CEA-VE spectra, the vertical transition energy and its intensity. As expected, the good agreement found between JOYCE and DFT descriptions of the PDI core's structure is reflected in the spectra shown in Figure 2.19. In fact, both the position and the shape of the JOYCE spectrum almost coincide with the ones computed along the DFT trajectory.

On the same foot, the discrepancies emerged in the average values and distribution of key Internal Coordinates, cause GAFF to deliver a significantly (∼0.3 eV) red-shifted spectrum, with an overestimated intensity, as revealed by Figure 2.20, where, instead of the molar absorbivity, $\epsilon(\omega) = C\omega L(\omega)$, the lineshape $L(\omega)$ given in equation 2.2 is considered.

Turning to the simulations in Acetonitrile, as detailed in section 2.3.2, we tested different schemes to take the solvent into account and Figure 2.21 collects the resulting CEA-VE spectra.

As evident from the first two top panels, when the solvent is accounted for with a given solvation scheme, the GAFF, panel a), and JOYCE, panel b), FFs behave rather similarly with respect to their GP reference spectra. It appears for instance that in both cases the simple **EEpc** scheme, based on bare point-charges, only

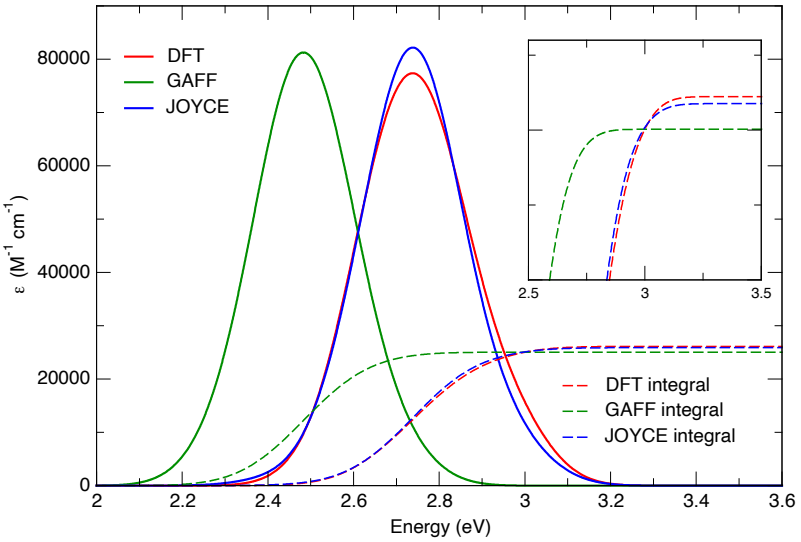

Figure 2.19: Absorption spectra ($\epsilon(\omega)$, $M^{-1}cm^{-1}$) and integral, computed with the CEA-VE approach along the trajectories of the isolated PDI monomer (GP) obtained with AIMD (DFT, red) or MD (GAFF, green and JOYCE,blue). The vertical transitions have been convoluted by using Gaussian functions having fwhm of 0.1 eV.

predicts a negligible effect, i.e. a slight blue-shift of less than ~ 0.01 eV. Furthermore, when the first solvation layer is included in the QM calculation (**QM/EE** scheme), both FFs show a more significant red-shift, of ~ 0.1 eV, in the absorption maximum with respect to GP spectra. This is in line with experimental evidences, which indicate, for a series of perylenes, a bathochromic shift of the order of $0.06 - 0.08$ eV, increasing as the solvent polarity increases.[124, 125]. Interestingly, results similar to the **QM/EE** scheme, can be also obtained with an implicit description of the medium, as in the **C-PCM** scheme: the main solvent effects seem to be captured, with an overall good agreement with the explicit **QM/EE** approach obtained at a significantly lower computational cost. It is important to stress, however, that implicit solvent schemes can hardly provide a reliable description of PDI self-assembly nor be used to monitor a possible dynamical solvent response.[126] Furthermore, the performances of implicit models for the prediction

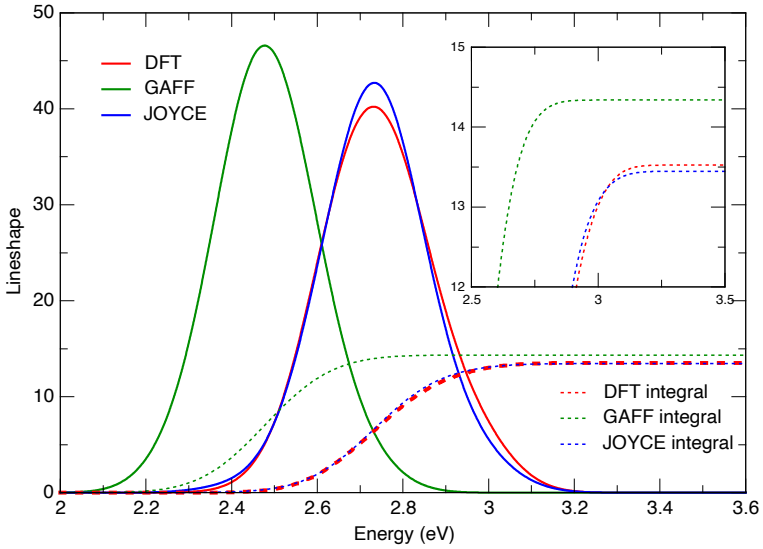

Figure 2.20: Absorption lineshape and integrals computed from the PDI MD runs (DFT, JOYCE, GAFF) in Gas Phase with the CEA-VE approach. The vertical transitions have been convoluted by using Gaussian functions having fwhm of 0.1 eV.

of solvatochromic shifts in solvents capable of forming hydrogen bonds like ACN would need a careful evaluation.[127]

In the bottom panel of Figure 2.21, we eventually compare the CEA-VE spectra computed with the most refined model (QM/EE), with the one experimentally recorded in ACN. [5] While the JOYCE-based spectrum is appreciably blue-shifted, (0.28 eV considering the maximum), an almost perfect agreement with experiment is obtained by using the GAFF trajectory (maximum: +0.04 eV). Based on the results of both the conformational analysis and the performances of the GP spectra with respect to the AIMD reference, this result is rather surprising and documents a fortuitous error cancellation, similarly to what recently reported for a metallo-organic dye complex. [128] On the one hand, the ∼0.3 eV red-shift found in GAFF-based spectra of the isolated PDI with respect to reference AIMD, evident in Figure 2.19, is due to the inaccurate bond lengths and angles of the perylene core, yielded by the GAFF simulations. Given the scarce flexibility of the π-

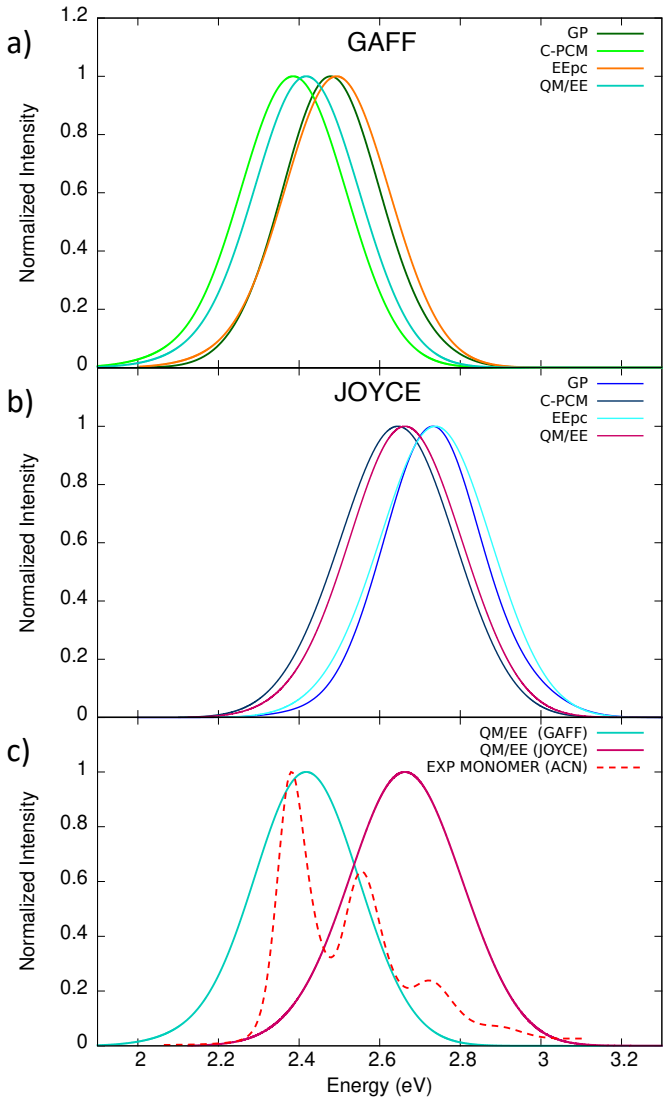

Figure 2.21: a) CEA-VE spectra computed along the GAFF trajectories: comparison between GP and PDI@ACN, by considering different solvent models (section 2.3.2); b) the same comparison for CEA-VE spectra computed along the JOYCE trajectories; c) Comparison of the PDI@ACN spectra computed using the **QM/EE** scheme with the experimental one. [5] For all the spectra, the vertical transitions have been convoluted by using Gaussian functions having fwhm of 0.1 eV.

core, it can be therefore expected that the spectra in solution will be affected by such a bias in a rather similar way. On the other hand, in the calculation of the excitation energy a blue-shift of about the same magnitude was reported

for the CAM-B3LYP functional with respect to the experiment. In summary, even if accounting for vibronic effects actually sensibly reduces the CAM-B3LYP deficiency (see next section), at CEA-VE level its combined effect with the error due to the geometrical inaccuracies leads, in the case of the GAFF, to the fortuitous very good agreement appearing in Figure 2.21. Nonetheless, the most important conclusion that can be drawn from the bottom panel, is the confirmation that, regardless of the employed FF, the CEA-VE approach is not able to reproduce the PDI vibronic progressions, which instead requires to take into account the coupling between electronic and vibrational quantum states explicitly, as discussed in the next section.

MQC spectra Figure 2.22a displays the $Ad-MD|gVH$ spectra calculated by averaging over the 100 snapshots extracted from the DFT, GAFF and JOYCE MD trajectories in GP (100 ps runs). Both GAFF and JOYCE predictions are very close to the reference DFT spectrum: a quite remarkable result because, as evidenced in Figure 2.19, at CEA-VE level the GAFF spectrum is off (red-shifted) by ~ 0.3 eV, due to the wrong sampling of the distribution of the stiff coordinates. This finding shows that $Ad-MD|gVH$ makes a very good job in recovering such an error. This is possible because, at each snapshot, the gVH method reconstructs harmonic PESs along the stiff coordinates, by extrapolating the equilibrium geometry from the gradient and Hessian. Since stiff coordinates have short-amplitude oscillations, this procedure reveals to be quite accurate even starting from significantly displaced geometries, like those sampled by GAFF. Results are expected to be different for systems with larger anharmonicites and couplings between soft and stiff coordinates. A more detailed analysis shows that the GAFF peaks maxima are slightly blue-shifted, while JOYCE's slightly red-shifted but closer to the reference. The intensity of the JOYCE spectrum is only apparently slightly smaller. Actually, the integrated intensity of JOYCE spectrum is extremely similar to the AIMD reference, indicating that the slightly smaller maxima are compensated by a slightly broader spectrum. JOYCE vibronic spectrum in fact becomes more intense than the DFT one at energies ≥ 3.1 eV. At variance, as shown in Figure 2.19, the total intensity of GAFF spectrum is truly, though very slightly, higher. Summing up, the vibronic peaks are quite well resolved along all three trajecto-

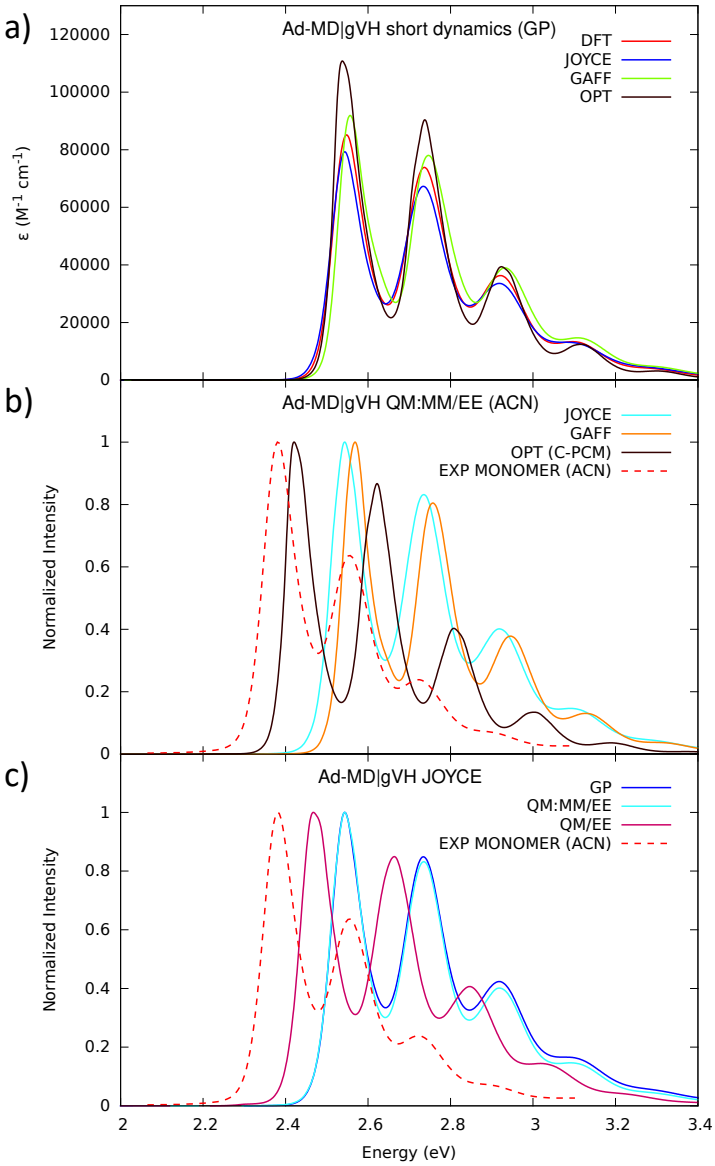

Figure 2.22: a) $Ad-MD|gVH$ spectra computed in GP along the AIMD and MD trajectories. The simple vibronic spectrum (OPT) computed for the single optimized PDI is also reported for comparison; b) Comparison among GAFF and Joyce based $Ad-MD|gVH$ spectra computed for the PDI@ACN system with the **QM/MM/EE** scheme, the OPT spectrum in PCM, and the experimental one; c) Effect of the solvent model scheme on the $Ad-MD|gVH$ PDI spectra in ACN computed along the Joyce trajectory. The experimental spectrum[5] is also reported for comparison. In all panels, the single vibronic spectra concurring in the $Ad-MD|gVH$ lineshape were calculated by including the torsions of the alkyl chains in the classical set, and considering a fwhm of 0.01 eV.

ries, they have a very regular shape and a quite similar width. The fact that vibronic resolution is preserved after an average over 100 snapshots indicates that no spurious broadening mechanism due to excessive fluctuations of the molecular structures occur during classical MD runs. This is especially noteworthy in the QMD-FF case, considering that JOYCE FF was built over a much smaller set of Internal Coordinates with respect to GAFF, avoiding for instance the burden connected the inclusion of all nonbonded intramolecular distances. Finally, it should be noted that in the $Ad-MD|gVH$ spectra shown in Figure 2.22, all vibrational DoF were treated at quantum level, except the δ_1–δ_3 torsions of the flexible lateral chains and the rotations of the methyl groups, which were included in the classical set. Hence, it is interesting to compare the predictions of $Ad-MD|gVH$ with a standard static vibronic VH approach, in which the spectrum is computed assuming harmonic approximation for all DoFs. Panel a) in Figure 2.22 displays

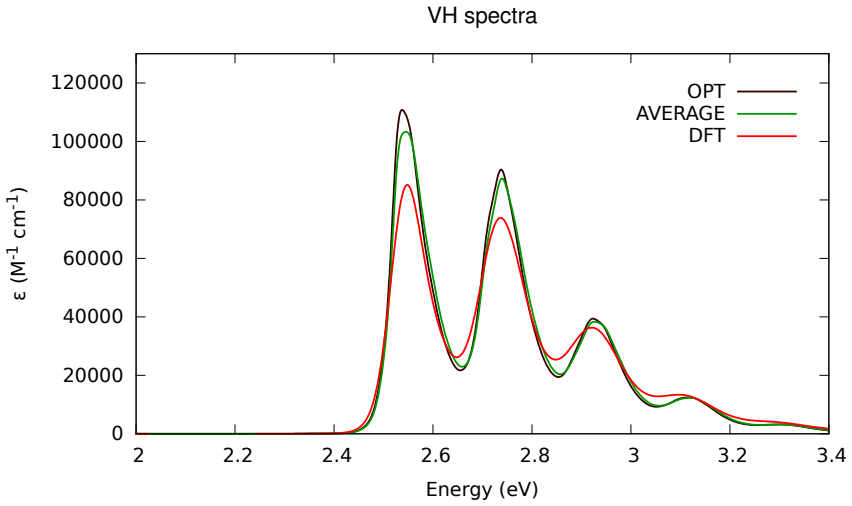

Figure 2.23: static vibronic spectrum of PDI in GP (OPT) compared with the average between the spectra computed for all the local minima of the dihedral torsional profiles (AVERAGE). The average have been weighted by using the calculated Boltzmann factors.

such spectrum (OPT, black line), and shows that it is indeed quite similar to the $Ad-MD|gVH$ ones, both in its position and overall shape. However the static vibronic spectrum is more resolved and the bands are slightly narrower. The same behaviour is observed considering the average of Boltzmann static spectra at all the local minima along the flexible torsions (Figure 2.23). This finding suggests

that fluctuations of the lateral chains do induce a broadening, captured by the $Ad-MD|gVH$ methodology, but this is minimal, in agreement with the scarce dependence of the spectra on the nature of the side chains argued in refs.[35] and discussed at the beginning of the chapter. This also explains why the low-energy peaks of the static spectrum appear higher, although the total intensity of the spectra is practically identical.

Figure 2.22b plots the $Ad-MD|gVH$ spectra computed in ACN along the GAFF or JOYCE trajectories using the **QM/MM/EE** solvent scheme, and compares them with the experiment.[5] In this case, beside the torsions of the lateral perylene chains also all solvent DOFs were included in the classical set. The figure also reports the results of a static vibronic computation with the VH method, obtained describing solvent effects with C-PCM (OPT). $Ad-MD|gVH$ spectral shapes are in good agreement with experiments, apart from an overestimation of the vibronic progression, i.e. of the relative intensity of the excited bands with respect to the lowest-energy $(0 \rightarrow 0)$ one. Such an overestimation is even slightly larger with C-PCM and can be thus ascribed to the use of CAM-B3LYP. As observed in GP, also in the PDI@ACN system $Ad-MD|gVH$ delivers spectra of rather similar quality, when applied to either GAFF or JOYCE trajectories. Focusing on the spectral position with respect to the experiment, MQC spectra are blue-shifted by ~ 0.2 eV in combination with JOYCE and slightly more with GAFF. Moreover, comparison of Figures 2.22a (GP) and 2.22b (ACN) shows that describing the solvent at **QM/MM/EE** level does not significantly affect either the spectral shape or the position. The situation is different when the static OPT approach is employed. C-PCM clearly does not describe the molecularity of the solvent, but it accounts for mutual solute/solvent polarizations which, on the other hand, are neglected in the **QM/MM/EE** model. The OPT/C-PCM scheme (in non-equilibrium regime, as recommended in ref. [88]) indeed predicts a remarkable solvent red-shift of ~ 0.11 eV in line with experiments. Despite the improved agreement with the experimental peaks position, the reliability of (linear response) C-PCM in accounting for the specific solvent shift in ACN should be taken with care, considering the failure of the same model in reproducing the experimental shift [124, 125] between ACN and diethyl ether, as displayed in Figure 2.24. Finally, it is worth noticing that the prediction of OPT/C-PCM is strongly depen-

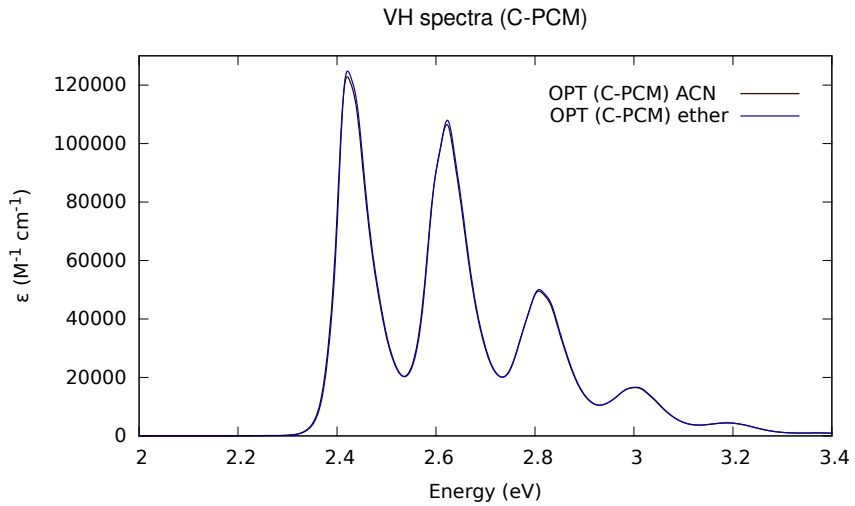

Figure 2.24: Comparison between the PDI static vibronic spectra in ACN and in diethyl ether. The **C-PCM** model has been used to account for the solvents effects.

dent on the adopted solvation regime: Figure 2.25 shows that switching from the non-equilibrium regime (usually adopted for vertical transitions but quite slower for vibronic spectra, due to the numerical calculation of the Hessians implemented in GAUSSIAN16) to the equilibrium regime (the default choice for optimizations and Hessians and much faster) worsens the overestimation of the vibronic progressions and the position of the spectrum, remarkably increasing the shift with respect to GP to ∼0.35 eV.

In order to incorporate in the $Ad-MD|gVH$ spectra the effect of the mutual solute/solvent polarization, accounted in average by C-PCM, we repeated the calculations along the JOYCE trajectory adopting the more refined **QM/EE** model scheme, as defined for the vibronic calculations in section 2.3.2. Figure 2.22c shows that the mutual polarization of solute and solvent molecules red-shifts the spectrum, by ~ 0.08 eV, approximately halving the error with respect to the experiment. It is noteworthy that the adopted procedure does not describe the effect of the solvent/solute polarization on the spectral shape: in order to do it within the $Ad-MD|gVH$ scheme, it would be necessary to recompute with a QM/EE protocol not only the energies but also the gradients and Hessians of the initial and final states at each snapshot. This would be extremely costly and is beyond

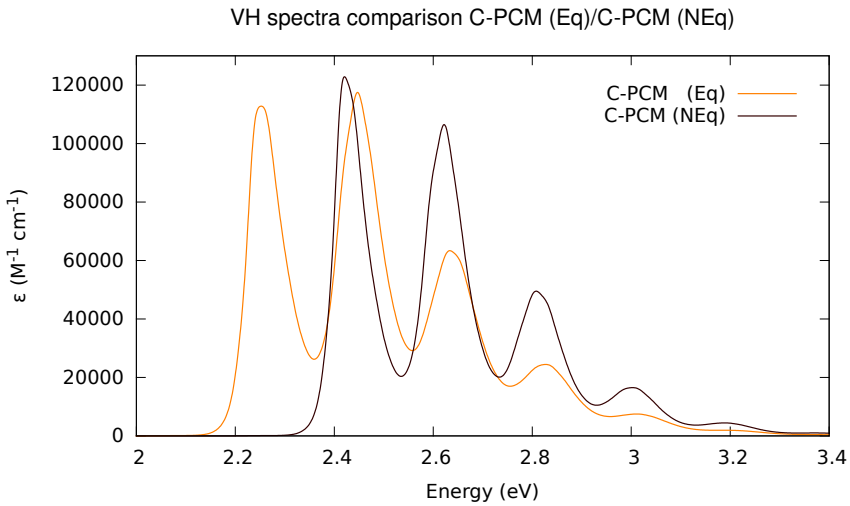

Figure 2.25: PDI static vibronic spectra in ACN calculated by considering both the Equilibrium (Eq) and the Non-Equilibrium (NEq) **C-PCM** model.

the aims of this thesis.

2.3.4 Final Remarks

The different schemes and options explored during this computational study, allowed us to draw a number of conclusions, whose interest goes beyond the application to the PDI species. First, as far as the FF's accuracy is concerned, GAFF and JOYCE FFs lead to remarkably different samplings, and this is reflected in the CEA-VE spectra computed along the two trajectories. In the Gas Phase, at difference with JOYCE, whose spectrum coincides with that computed along the AIMD trajectory used for reference, GAFF is red-shifted by 0.3-0.4 eV. The reason can be traced back to an intrinsic inconsistency in the application of CEA-VE methodology in combination with MD driven by a general purpose FF. CEA-VE is in fact based on the application of the classical Franck-Condon principle. According to it, one should select a level of theory, sample the minimum region in the Ground State and then compute the vertical transitions. This is what is done with the AIMD carried out with the CAM-B3LYP functional, and with the JOYCE FF, built to minimize the differences with the DFT PES. On the contrary, GAFF describes a different PES, consequently inducing the MD runs to explore a configurational

space that does not correspond to the minimum region of the DFT potential. Nonetheless, when the solvent is introduced, the GAFF spectrum at CEA-VE level seems to be in better agreement with the experimental one. Here, we have clearly shown that this is the effect of a fortuitous compensation of errors. On one side a wrong sampling, on the other side the fact that vibronic contributions are neglected and CAM-B3LYP overestimates the transition energies.

Turning to MQC spectra, in Gas Phase $Ad-MD|gVH$ delivers similar results with all three samplings, thus correcting the inherent errors found for GAFF. Beside being another important advantage of our procedure, this finding is quite instructive, because it unveils that for PDI the errors of GAFF sampling more relevant to the spectrum concern stiff modes. This is the reason why they can be corrected by the quadratic extrapolation performed by gVH to locate the minima of the initial and final PES along the stiff coordinates. When the solvent is introduced, if a not-polarizable point-charge embedding model is considered, interestingly, none of the trajectories is able to produce a spectrum with the expected solvent shift with respect to the Gas Phase. In fact, we demonstrated that mutual solute-solvent polarization is indeed important to reproduce the solvent shift, and it was introduced in our procedure by considering a first QM solvation shell. In this particular case, our calculations indicate that these effects could also be inserted with specific settings of the C-PCM, but we do expect this will not be the case for π-aggregates, where the molecularity of the solvent will be important and PCM cavities may be unphysically large. As an additional general observation, it is also worth highlighting that our results document that accounting for the quantum nature of the stiff modes does not simply introduce vibronic resolution: in fact, once the vibronic effects are taken into account, a net red-shift of the spectrum maximum is predicted by ~ 0.2 eV, both in gas and in ACN, strongly improving the agreement with experiment. Similar findings have already been reported in literature for other systems.[129] Finally, the similarity of the $Ad-MD|gVH$ spectra obtained from the GAFF and JOYCE based trajectories, clearly confirms that a reliable description of the lateral pendants is not really required for an accurate spectrum of the PDI monomer, considering the significant errors in the flexible lateral chain GAFF populations, revealed by our conformational analysis. This is further corroborated by the comparison with a full quantum static vibronic cal-

culation that treats also the soft coordinates as harmonic quantum modes: the good agreement with the $Ad-MD|gVH$ spectrum shows that they just induce a very limited broadening. Yet, even if in the specific case the flexibility of the lateral chains has a mild effect on the spectrum, their reliable description is expected to have a larger impact on the spectra of aggregates. On this respect the fact that JOYCE FF is able to properly reproduce both the oscillations of stiff modes and the flexibility of the soft ones is very promising: the extension of the $Ad-MD|gVH$ procedure in combination with JOYCE to the study of aggregates is currently in progress. The major step is to substitute the engine for the computation of vibronic spectra in case of negligible inter-state couplings (gVH) with a model that explicitly account for such couplings like Linear vibronic coupling models[130] and exciton+CT models.

Bibliography

[1] A. Segalina, X. Assfeld, A. Monari, M. Pastore, *J. Phys. Chem. C* **2019**, *123*, 6427–6437.

[2] A. Segalina, J. Cerezo, G. Prampolini, F. Santoro, M. Pastore, *J. Chem. Theory Comput.* **2020**, *16*, 7061–7077.

[3] Y. Shirota, H. Kageyama, *Chem. Rev.* **2007**, *107*, 953–1010.

[4] L. Torsi, M. Magliulo, K. Manoli, G. Palazzo, *Chem. Soc. Rev.* **2013**, *42*, 8612–8628.

[5] S. Berardi, V. Cristino, M. Canton, R. Boaretto, R. Argazzi, E. Benazzi, L. Ganzer, R. Borrego Varillas, G. Cerullo, Z. Syrgiannis, F. Rigodanza, M. Prato, C. A. Bignozzi, S. Caramori, *J. Phys. Chem. C* **2017**, *121*, 17737–17745.

[6] J. Roncali, P. Leriche, P. Blanchard, *Adv. Mater.* **2014**, *26*, 3821–3838.

[7] Shahnawaz, S. Sudheendran Swayamprabha, M. R. Nagar, R. A. K. Yadav, S. Gull, D. K. Dubey, J.-H. Jou, *J. Mater. Chem. C* **2019**, *7*, 7144–7158.

[8] N. J. Hestand, F. C. Spano, *Acc. Chem. Res.* **2017**, *50*, 341–350.

[9] M. Kasha, *Radiat. Res.* **1963**, *20*, 55–70.

[10] D. Kim, D. Lee, H. Lee, W. Lee, Y. Kim, J. Han, K. Cho, *Adv. Mater.* **2007**, *19*, 678–682.

[11] A. Kuhnle, *Curr. Opin. Colloid Interface Sci.* **2009**, *14*, 157–168.

[12] K. Takazawa, Y. Kitahama, Y. Kimura, G. Kido, *Nano Lett.* **2005**, *5*, 1293–1296.

[13] A. E. Clark, C. Qin, A. D. Li, *J. Am. Chem. Soc.* **2007**, *129*, 7586–7595.

[14] Y. Houari, A. D. Laurent, D. Jacquemin, *J. Phys. Chem. C* **2013**, *117*, 21682–21691.

[15] B. O'Regan, M. Grätzel, *Nature* **1991**, *353*, 737–740.

[16] V. Vaissier, E. Mosconi, D. Moia, M. Pastore, J. M. Frost, F. De Angelis, P. R. F. Barnes, J. Nelson, *Chem. Mater.* **2014**, *26*, 4731–4740.

[17] M. Pastore, *Computation* **2017**, *5*, 5.

[18] M. K. Brennaman, R. J. Dillon, L. Alibabaei, M. K. Gish, C. J. Dares, D. L. Ashford, R. L. House, G. J. Meyer, J. M. Papanikolas, T. J. Meyer, *J. Am. Chem. Soc.* **2016**, *138*, 13085–13102.

[19] P. Xu, N. S. McCool, T. E. Mallouk, *Nano Today* **2017**, *14*, 42–58.

[20] A. K. Chandiran, S. M. Zakeeruddin, R. Humphry-Baker, M. K. Nazeeruddin, M. Grätzel, F. Sauvage, *ChemPhysChem* **2017**, *18*, 2724–2731.

[21] S. Jungsuttiwong, K. Sirithip, N. Prachumrak, R. Tarsang, T. Sudyoadsuk, S. Namuangruk, N. Kungwan, V. Promarak, T. Keawin, *New J. Chem.* **2017**, *41*, 7081–7091.

[22] M. Bonchio, Z. Syrgiannis, M. Burian, N. Marino, E. Pizzolato, K. Dirian, F. Rigodanza, G. A. Volpato, G. La Ganga, N. Demitri, et al., *Nat. Chem.* **2019**, *11*, 146–153.

[23] F. Ronconi, Z. Syrgiannis, A. Bonasera, M. Prato, R. Argazzi, S. Caramori, V. Cristino, C. A. Bignozzi, *J. Am. Chem. Soc.* **2015**, *137*, 4630–4633.

[24] K. Hanson, M. K. Brennaman, H. Luo, C. R. K. Glasson, J. J. Concepcion, W. Song, T. J. Meyer, *ACS Appl. Mater. Interfaces* **2012**, *4*, 1462–1469.

[25] M. K. Brennaman, M. R. Norris, M. K. Gish, E. M. Grumstrup, L. Alibabaei, D. L. Ashford, A. M. Lapides, J. M. Papanikolas, J. L. Templeton, T. J. Meyer, *J. Phys. Chem. Lett.* **2015**, *6*, 4736–4742.

[26] R. J. Kamire, K. L. Materna, W. L. Hoffeditz, B. T. Phelan, J. M. Thomsen, O. K. Farha, J. T. Hupp, G. W. Brudvig, M. R. Wasielewski, *J. Phys. Chem. C* **2017**, *121*, 3752–3764.

[27] Z.-G. Zhang, B. Qi, Z. Jin, D. Chi, Z. Qi, Y. Li, J. Wang, *Energy Environ. Sci.* **2014**, *7*, 1966–1973.

[28] E. Kozma, M. Catellani, *Dyes Pigm.* **2013**, *98*, 160–179.

[29] B. Zhang, I. Lyskov, L. J. Wilson, R. P. Sabatini, A. Manian, H. Soleimaninejad, J. M. White, T. A. Smith, G. Lakhwani, D. J. Jones, K. P. Ghiggino, S. P. Russo, W. W. H. Wong, *J. Mater. Chem. C* **2020**, *8*, 8953–8961.

[30] K. Dirian, S. Bauroth, A. Roth, Z. Syrgiannis, F. Rigodanza, M. Burian, H. Amenitsch, D. I. Sharapa, M. Prato, T. Clark, D. M. Guldi, *Nanoscale* **2018**, *10*, 2317–2326.

[31] E. Krieg, A. Niazov-Elkan, E. Cohen, Y. Tsarfati, B. Rybtchinski, *Acc. Chem. Res.* **2019**, *52*, 2634–2646.

[32] Z. Yang, X. Chen, *Acc. Chem. Res.* **2019**, *52*, 1245–1254.

[33] S. M. Obaidulla, M. R. Habib, Y. Khan, Y. Kong, T. Liang, M. Xu, *Adv. Mater. Interfaces* **2020**, *7*, 1901197.

[34] K. Balakrishnan, A. Datar, T. Naddo, J. Huang, R. Oitker, M. Yen, J. Zhao, L. Zang, *J. Am. Chem. Soc.* **2006**, *128*, 7390–7398.

[35] F. Würthner, *Chem. Commun.* **2004**, 1564–1579.

[36] H. Zhao, Y.-y. Zhang, H. Xu, Z.-m. He, Z.-L. Zhang, H.-q. Zhang, *Tetrahedron* **2015**, *71*, 7752–7757.

[37] C. Li, H. Wonneberger, *Adv. Mater.* **2012**, *24*, 613–636.

[38] G. Prampolini, P. R. Livotto, I. Cacelli, *J. Chem. Theory Comput.* **2015**, *11*, 5182–5196.

[39] S. Kraner, G. Prampolini, G. Cuniberti, *J. Phys. Chem. C* **2017**, *121*, 17088–17095.

[40] L. Greff da Silveira, M. Jacobs, G. Prampolini, P. R. Livotto, I. Cacelli, *J. Chem. Theory Comput.* **2018**, *14*, 4884–4900.

[41] G. Belletti, E. Schulte, E. Colombo, W. Schmickler, P. Quaino, *Chem. Phys. Lett.* **2019**, *735*, 136778.

[42] K. Claridge, A. Troisi, *J. Phys. Chem. B* **2019**, *123*, 428–438.

[43] L. Jiang, D. M. Rogers, J. D. Hirst, H. Do, *J. Chem. Theory Comput.* **2020**, *10.1021/acs.jctc.0c00399*.

[44] M. Bondanza, M. Nottoli, L. Cupellini, F. Lipparini, B. Mennucci, *Phys. Chem. Chem. Phys.* **2020**, 14433–14448.

[45] A. Petrone, J. Cerezo, F. J. A. Ferrer, G. Donati, R. Improta, N. Rega, F. Santoro, *J. Phys. Chem. A* **2015**, *119*, 5426–5438.

[46] J. Cerezo, F. Santoro, G. Prampolini, *Theor. Chem. Acc.* **2016**, *135*, 143.

[47] J. Cerezo, D. Aranda, F. J. Avila Ferrer, G. Prampolini, F. Santoro, *J. Chem. Theory Comput.* **2020**, *16*, 1215–1231.

[48] J. Sung, P. Kim, B. Fimmel, F. Würthner, D. Kim, *Nature Comm.* **2015**, *6*.

[49] E. R. Kennehan, C. Grieco, A. N. Brigeman, G. S. Doucette, A. Rimshaw, K. Bisgaier, N. C. Giebink, J. B. Asbury, *Phys. Chem. Chem. Phys.* **2017**, *19*, 24829–24839.

[50] H.-M. Zhao, J. Pfister, V. Settels, M. Renz, M. Kaupp, V. C. Dehm, F. Würthner, R. F. Fink, B. Engels, *J. Am. Chem. Soc.* **2009**, *131*, 15660–15668.

[51] Z. Chen, V. Stepanenko, V. Dehm, P. Prins, L. D. Siebbeles, J. Seibt, P. Marquetand, V. Engel, F. Würthner, *Chem. Eur. J.* **2007**, *13*, 436–449.

[52] F. Würthner, Z. Chen, V. Dehm, V. Stepanenko, *Chem. Commun.* **2006**, 1188–1190.

[53] F. C. Spano, S. C. J. Meskers, E. Hennebicq, D. Beljonne, *J. Am. Chem. Soc.* **2007**, *129*, 7044–7054.

[54] V. Settels, A. Schubert, M. Tafipolski, W. Liu, V. Stehr, A. K. Topczak, J. Pflaum, C. Deibel, R. F. Fink, V. Engel, et al., *J. Am. Chem. Soc.* **2014**, *136*, 9327–9337.

[55] R. Pandya, R. Y. Chen, Q. Gu, J. Gorman, F. Auras, J. Sung, R. Friend, P. Kukura, C. Schnedermann, A. Rao, *J. Phys. Chem. A* **2020**, *124*, 2721–2730.

[56] N. J. Hestand, F. C. Spano, *Chem. Rev.* **2018**, *118*, 7069–7163.

[57] H. Yoo, J. Yang, A. Yousef, M. R. Wasielewski, D. Kim, *J. Am. Chem. Soc.* **2010**, *132*, 3939–3944.

[58] R. F. Fink, J. Seibt, V. Engel, M. Renz, M. Kaupp, S. Lochbrunner, H.-M. Zhao, J. Pfister, F. Würthner, B. Engels, *J. Am. Chem. Soc.* **2008**, *130*, 12858–12859.

[59] E. Engel, K. Schmidt, D. Beljonne, J.-L. Brédas, J. Assa, H. Fröb, K. Leo, M. Hoffmann, *Phys. Rev. B* **2006**, *73*, 245216.

[60] C. Kaufmann, W. Kim, A. Nowak-Król, Y. Hong, D. Kim, F. Würthner, *J. Am. Chem. Soc.* **2018**, *140*, 4253–4258.

[61] T. Ye, R. Singh, H.-J. Butt, G. Floudas, P. E. Keivanidis, *ACS Appl. Mater. Interfaces* **2013**, *5*, 11844–11857.

[62] F. Fennel, S. Wolter, Z. Xie, P.-A. Plötz, O. Kühn, F. Würthner, S. Lochbrunner, *J. Am. Chem. Soc.* **2013**, *135*, 18722–18725.

[63] J. Sung, A. Nowak-Kröl, F. Schlosser, B. Fimmel, W. Kim, D. Kim, F. Würthner, *J. Am. Chem. Soc.* **2016**, *138*, 9029–9032.

[64] M. Walker, A. J. A. Harvey, A. Sen, C. E. H. Dessent, *J. Phys. Chem. A*, *117*.

[65] J. Tomasi, B. Mennucci, R. Cammi, *Chem. Rev.* **2005**, *105*, 2999–3094.

[66] M. J. Frisch, G. W. Trucks, H. B. Schlegel, G. E. Scuseria, M. A. Robb, J. R. Cheeseman, G. Scalmani, V. Barone, B. Mennucci, G. A. Petersson, H. Nakatsuji, M. Caricato, X. Li, H. P. Hratchian, A. F. Izmaylov, J. Bloino, G. Zheng, J. L. Sonnenberg, M. Hada, M. Ehara, K. Toyota, R. Fukuda, J. Hasegawa, M. Ishida, T. Nakajima, Y. Honda, O. Kitao, H. Nakai, T. Vreven, J. A. Montgomery, Jr., J. E. Peralta, F. Ogliaro, M. Bearpark, J. J. Heyd, E. Brothers, K. N. Kudin, V. N. Staroverov, R. Kobayashi, J. Normand, K. Raghavachari, A. Rendell, J. C. Burant, S. S. Iyengar, J. Tomasi, M. Cossi, N. Rega, J. M. Millam, M. Klene, J. E. Knox, J. B. Cross, V. Bakken, C. Adamo, J. Jaramillo, R. Gomperts, R. E. Stratmann, O. Yazyev, A. J. Austin, R. Cammi, C. Pomelli,

J. W. Ochterski, R. L. Martin, K. Morokuma, V. G. Zakrzewski, G. A. Voth, P. Salvador, J. J. Dannenberg, S. Dapprich, A. D. Daniels, Ö. Farkas, J. B. Foresman, J. V. Ortiz, J. Cioslowski, D. J. Fox, Gaussian 09 Revision E.01, Gaussian Inc. Wallingford CT 2009.

[67] J. Wang, R. Wolf, J. Caldwell, P. Kollman, D. Case, *J. Comput. Chem.* **2004**, *25*, 1157–1174.

[68] J. Wang, W. Wang, P. A. Kollman, D. A. Case, *J. Mol. Graph. Model.* **2006**, *25*, 247–260.

[69] P. Mark, L. Nilsson, *J. Phys. Chem. A* **2001**, *105*, 9954–9960.

[70] A. W. Götz, M. J. Williamson, D. Xu, D. Poole, S. Le Grand, R. C. Walker, *J. Chem. Theory Comput.* **2012**, *8*, 1542–1555.

[71] I. S. Ufimtsev, T. J. Martínez, *J. Chem. Theory Comput.* **2008**, *4*, 222–231.

[72] I. S. Ufimtsev, T. J. Martinez, *J. Chem. Theory Comput.* **2009**, *5*, 1004–1015.

[73] I. S. Ufimtsev, T. J. Martinez, *J. Chem. Theory Comput.* **2009**, *5*, 2619–2628.

[74] S. Hirata, M. Head-Gordon, *Chem. Phys. Lett.* **1999**, *314*, 291–299.

[75] C. Lee, W. Yang, R. G. Parr, *Phys. Rev. B* **1988**, *37*, 785–789.

[76] T. Yanai, D. P. Tew, N. C. Handy, *Chem. Phys. Lett.* **2004**, *393*, 51–57.

[77] A. Klamt, G. Schuurmann, *J. Chem. Soc., Perkin Trans. 2* **1993**, 799–805.

[78] F. Plasser, S. A. Bäppler, M. Wormit, A. Dreuw, *J. Chem. Phys.* **2014**, *141*, 024107.

[79] F. Plasser, H. Lischka, *J. Chem. Theory Comput.* **2012**, *8*, 2777–2789.

[80] F. Plasser, M. Wormit, A. Dreuw, *J. Chem. Phys.* **2014**, *141*, 024106.

[81] M. C. R. Delgado, E.-G. Kim, D. A. d. S. Filho, J.-L. Bredas, *J. Am. Chem. Soc.* **2010**, *132*, 3375–3387.

[82] S. Ghosh, X.-Q. Li, V. Stepanenko, F. Würthner, *Chem. Eur. J.* **2008**, *14*, 11343–11357.

[83] S. Siddiqui, F. Spano, *Chem. Phys. Lett.* **1999**, *308*, 99–105.

[84] J. J. Nogueira, F. Plasser, L. González, *Chem. Sci.* **2017**, *8*, 5682–5691.

[85] A. Charaf-Eddin, A. Planchat, B. Mennucci, C. Adamo, D. Jacquemin, *J. Chem. Theory Comput.* **2013**, *9*, 2749–2760.

[86] S. A. Mewes, F. Plasser, A. Krylov, A. Dreuw, *J. Chem. Theory Comput.* **2018**, *14*, 710–725.

[87] A. E. Clark, C. Qin, A. D. Q. Li, *J. Am. Chem. Soc.* **2007**, *129*, 7586–7595.

[88] F. Santoro, R. Improta, A. Lami, J. Bloino, V. Barone, *J. Chem. Phys.* **2007**, *126*, 084509.

[89] A. Hazra, M. Nooijen, *Int. J. Quantum Chem.* **2003**, *95*, 643–657.

[90] M. Dierksen, S. Grimme, *J. Chem. Phys.* **2005**, *122*, 244101.

[91] H.-C. Jankowiak, J. L. Stuber, R. Berger, *J. Chem. Phys.* **2007**, *127*, 234101.

[92] F. Santoro, A. Lami, R. Improta, J. Bloino, V. Barone, *J. Chem. Phys.* **2008**, *128*, 224311.

[93] R. Ianconescu, E. Pollak, *J. Phys. Chem. A* **2004**, *108*, 7778–7784.

[94] J. Tatchen, E. Pollak, *J. Chem. Phys.* **2008**, *128*, 164303.

[95] J. Huh, R. Berger, *J. Phys.: Conf. Ser.* **2012**, *380*, 012019.

[96] R. Borrelli, A. Capobianco, A. Peluso, *J. Phys. Chem. A* **2012**, *116*, 9934–9940.

[97] A. Baiardi, J. Bloino, V. Barone, *J. Chem. Theory Comput.* **2013**, *9*, 4097–4115.

[98] F. J. Avila Ferrer, J. Cerezo, J. Soto, R. Improta, F. Santoro, *Comput. Theoret. Chem.* **2014**, *1040–1041*, 328–337.

[99] J. Cerezo, G. Mazzeo, G. Longhi, S. Abbate, F. Santoro, *J. Phys. Chem. Lett.* **2016**, *7*, 4891–4897.

[100] T. J. Zuehlsdorff, C. M. Isborn, *J. Chem. Phys.* **2018**, *148*, 024110.

[101] T. J. Zuehlsdorff, J. A. Napoli, J. M. Milanese, T. E. Markland, C. M. Isborn, *J. Chem. Phys.* **2018**, *149*, 024107.

[102] T. J. Zuehlsdorff, A. Montoya-Castillo, J. A. Napoli, T. E. Markland, C. M. Isborn, *J. Chem. Phys.* **2019**, *151*, 074111.

[103] D. Loco, L. Cupellini, *Int. J. Quantum Chem.* **2019**, *119*, e25726.

[104] J. Cerezo, F. J. A. Ferrer, G. Prampolini, F. Santoro, *J. Chem. Theory Comput.* **2015**, *11*, 5810–5825.

[105] F. J. Avila Ferrer, F. Santoro, *Phys. Chem. Chem. Phys.* **2012**, *14*, 13549–13563.

[106] J. Cerezo, F. Santoro, *J. Chem. Theory Comput.* **2016**, *12*, 4970–4985.

[107] M. Lax, *J. Chem. Phys.* **1952**, *20*, 1752–1760.

[108] A. Baiardi, J. Bloino, V. Barone, *J. Chem. Phys.* **2016**, *144*, 084114.

[109] I. Cacelli, G. Prampolini, *J. Chem. Theory Comput.* **2007**, *3*, 1803–1817.

[110] V. Barone, I. Cacelli, N. De Mitri, D. Licari, S. Monti, G. Prampolini, *Phys. Chem. Chem. Phys.* **2013**, *15*, 3736–51.

[111] J. Cerezo, G. Prampolini, I. Cacelli, *Theor. Chem. Acc.* **2018**, *137*, 80.

[112] M. J. Abraham, T. Murtola, R. Schulz, S. Páll, J. C. Smith, B. Hess, E. Lindahl, *SoftwareX* **2015**, *1-2*, 19–25.

[113] A. M. Nikitin, A. P. Lyubartsev, *J. Comput. Chem.* **2007**, *28*, 2020–2026.

[114] H. J. C. Berendsen, J. P. M. Postma, W. F. van Gunsteren, A. DiNola, J. R. Haak, *J. Chem. Phys.* **1984**, *81*, 3684–3690.

[115] M. Parrinello, A. Rahman, *J. Appl. Phys.* **1981**, *52*, 7182–7190.

[116] G. Bussi, D. Donadio, M. Parrinello, *J. Chem. Phys.* **2007**, *126*, 014101.

[117] M. J. Frisch, G. W. Trucks, H. B. Schlegel, G. E. Scuseria, M. A. Robb, J. R. Cheeseman, G. Scalmani, V. Barone, G. A. Petersson, H. Nakatsuji, X. Li, M. Caricato, A. V. Marenich, J. Bloino, B. G. Janesko, R. Gomperts, B. Mennucci, H. P. Hratchian, J. V. Ortiz, A. F. Izmaylov, J. L. Sonnenberg, D. Williams-Young, F. Ding, F. Lipparini, F. Egidi, J. Goings, B. Peng, A. Petrone, T. Henderson, D. Ranasinghe, V. G. Zakrzewski, J. Gao, N. Rega, G. Zheng, W. Liang, M. Hada, M. Ehara, K. Toyota, R. Fukuda, J. Hasegawa, M. Ishida, T. Nakajima, Y. Honda, O. Kitao, H. Nakai, T. Vreven, K. Throssell, J. A. Montgomery, Jr., J. E. Peralta, F. Ogliaro, M. J. Bearpark, J. J. Heyd, E. N. Brothers, K. N. Kudin, V. N. Staroverov, T. A. Keith, R. Kobayashi, J. Normand, K. Raghavachari, A. P. Rendell, J. C. Burant, S. S. Iyengar, J. Tomasi, M. Cossi, J. M. Millam, M. Klene, C. Adamo, R. Cammi, J. W. Ochterski, R. L. Martin, K. Morokuma, O. Farkas, J. B. Foresman, D. J. Fox, Gaussian16 Revision C.01, Gaussian Inc. Wallingford CT, **2016**.

[118] S. Grimme, S. Ehrlic, L. Goerigk, *J. Comp. Chem.* **2011**, *32*, 1456–65.

[119] G. Bussi, M. Parrinello, *Phys. Rev. E* **2007**, *75*, 056707.

[120] F. Santoro, $\mathcal{FC}classes$, a Fortran 77 code for vibronic calculations, visit: http://www.pi.iccom.cnr.it/fcclasses, last consulted November, **2019**.

[121] F. Santoro, J. Cerezo, $\mathcal{FC}classes3$, a code for vibronic calculations. Available upon request, **2019**.

[122] Q. Peng, Y. Niu, C. Deng, Z. Shuai, *Chem. Phys.* **2010**, *370*, 215–222.

[123] O. Andreussi, I. G. Prandi, M. Campetella, G. Prampolini, B. Mennucci, *J. Chem. Theory Comput.* **2017**, *13*, 4636–4648.

[124] Z. Chen, B. Fimmel, F. Würthner, *Org. Biomol. Chem.* **2012**, *10*, 5845–5855.

[125] S. Maity, M. Shyamal, P. Mazumdar, G. P. Sahoo, R. Maity, G. Salgado-Morán, A. Misra, *J. Mol. Liq.* **2016**, *224*, 255–264.

[126] G. Prampolini, F. Ingrosso, J. Cerezo, A. Iagatti, P. Foggi, M. Pastore, *J. Phys. Chem. Lett.* **2019**, *10*, 2885–2891.

[127] A. Eilmes, *Theor. Chem. Acc.* **2014**, *133*, 1–13.

[128] V. Diez-Cabanes, G. Prampolini, A. Francés-Monerris, A. Monari, M. Pastore, *Molecules* **2020**, *25*.

[129] F. J. Avila Ferrer, J. Cerezo, E. Stendardo, R. Improta, F. Santoro, *J. Chem. Theory Comput.* **2013**, *9*, 2072–2082.

[130] Y. Liu, L. Martínez Fernández, J. Cerezo, G. Prampolini, R. Improta, F. Santoro, *Chem. Phys.* **2018**, *515*, 452–463.

Chapter 3
Structure and Energetics of Dye-Sensitized NiO Interfaces in Water from AIMD and GW Calculations

The results presented in this chapter have been reproduced from:

- **Structure and Energetics of Dye-Sensitized NiO Interfaces in Water from AIMD and GW Calculations** A. Segalina, S. Lebegue, D. Rocca, S. Piccinin and M. Pastore, In preparation

Thirty years have passed since the pioneering work of O'Regan and Grätzel[1] paving the way to the development of efficient Dye-Sensitized Solar Cells (DSSCs). The standard architecture of a DSSC includes the use of a single photoactive electrode that can be either a photoanode (n-type DSSCs)[1, 2] or a photocathode (p-type DSSCs).[3, 4] The photo-active interface in a DSSC is composed of three principal ingredients: a wide band gap Semiconductor (SC), usually TiO_2 and NiO in n- and p-type DSSCs respectively, a dye sensitizer, either a full organic or a metallorganic compound, and a redox shuttle. The functioning mechanism of a n-/p-type DSSC is the following: sunlight is absorbed by the photosensitizing dye and the photo-excited electrons/holes are injected in the Conduction/Valence Band (CB/VB) of the SC, while the oxidized/reduced redox shuttle, having regenerated the dye Ground State (GS), is in turn reduced/oxidized at the counter electrode, closing the circuit.[5] Clearly, a multitude of factors interplays in determining the overall device efficiency,[6] such as the opto-electronic properties of the isolated dyes and Semiconductors, the structure of the dye/SC interface, the fast dye regeneration by the redox mediator and the efficient electron/hole injection into the SC. The energetical prerequisite, however, to realize the cascade of electron/hole transfer processes described above is the correct alignment of the redox potentials (energy levels) between the dye, the SC and the electrolyte: the Excited/Ground State potential of the dye should be higher/lower of the CB/VB edge of the SC to have electron/hole injection, while the oxidation/reduction potential of the electrolyte couple should be higher/lower of the Ground/Excited State oxidation potential of the dye to have the GS regeneration.

If, on one hand, n-type DSSCs have known a rapid development in the last decades, with reported power conversion efficiencies of about 14% [7, 8], the performances of p-type DSSCs remains, on the other hand, extremely poor (PCEs $\sim 2.5\%$).[3, 9, 10] Research efforts in boosting the efficiency of p-type dye-sensitized photo-electrodes, for both DSSCs and Dye-Sensitized Photoelectrochemical Cells (DSPECs),[11, 12] are motivated by the possibility of combining a photocathode and a photoanode in tandem devices, to surpass the theoretical Shockley–Queisser upper efficiency limit ($\sim 30\%$) of a single photoactive electrode solar cell.[13, 14]

Despite the recent encouraging attempts to find alternative transparent p-type Semiconductors,[11, 15, 16] NiO is still the standard material, both in Solar Cells

and Photoelectrochemical Cells. If on one hand, mesopourous NiO has good electrical conductivity,[17, 18] and, ultrafast interfacial hole injection from photoexcited dyes has been reported[19–22], it shows poor interfacial charge transfer resistance and trap states placed above the SC VB edge, which promote detrimental hole/electron recombination reactions at the SC/dye/electrolyte interface.[17, 22–24] As a matter of fact, a detailed understanding and characterization of the energetics, trapping mechanisms and hole dynamics at the dye/NiO interface is still lacking, while this would be needed to give clear guidelines to optimize the structure of dyes, electrolytes and catalysts.[25, 26]

In this regard, computational modeling is a powerful tool to predict the optoelectronic and redox properties of Semiconductor, chromophores and catalysts as well as to provide atomistic insights on the structure, energetics and charge generation in model dye-sensitized interfaces. [27–36]

As far as dye-sensitized nickel oxide is concerned, however, relatively few computational works, based on Density Functional Theory (DFT) calculations, have been reported.[37–43] A common outcome of these studies is that the interfacial energetics, dictating the driving force for hole injection from the dye to the NiO VB, turns out to be extremely sensitive to the dye anchoring mode and solvation effects, thus indicating a major role of the interfacial dipole in influencing the dye and Semiconductor energy levels lining up.

Piccinin and co-workers[37] very recently reported a study on the electronic structure of the (100) NiO surface sensitized by the Coumarin 343[44–46] dye by means of Ab Initio Molecular Dynamics (AIMD) and Density functional theory (DFT) calculations. In this work it is shown that the inclusion of explicit solvation effects is essential to predict a favorable energy levels alignment to allow the hole transfer from the dye's HOMO to the NiO's VB states. The calculated driving forces by both the PBE+U approach and the HSE06 hybrid functional were found, however, to be somewhat underestimated with respect to experiments, as a result of a sizeable destabilization of the dye's HOMO. As also reported for dye@TiO_2 systems,[47, 48] this suggests that hybrid functionals are unable to correctly reproduce the interfacial energy levels alignment in hybrid organic/inorganic interfaces, since molecules and SC surfaces may require different percentage of nonlocal exchange to be properly treated, as a consequence of their different electronic

screening.[47]

In these systems, the spatial dependence of the electronic correlation can be accounted for by using more refined approximations, such as Many Body Perturbation Theory (MBPT) based methods.[28, 49–51] In particular, within the MBPT methods, the Hedin's GW approximation is the state-of-the-art for the computational modeling of photoemission and inverse photoemission process for solid systems, as well as for the calculation of Ionization potentials (IP) and electron affinities (EA) of molecules.[49, 52, 53] Moreover, GW is particularly suitable to handle interface systems, being able to correctly describe image charge effects[54–56] which can be pronounced for the dye's electronic states and critically influence the energy levels alignment.[47, 51, 57–59]

Here we report a theoretical characterization of the C343-sensitized NiO surface in water, by combining AIMD simulations with GW (G_0W_0) calculations along the MD trajectory, to reliably describe the structure and energetics of the interface when explicit solvation and finite temperature effects are also accounted for.

The chapter is organized as follows: after the description of the theoretical methods (Section 3.1), we validate our GW protocol on the standalone elements of the C343@NiO interface and on the NiO bulk system. Secondly, we analyze the electronic structure of the C343@NiO interface for which we compute the energy gap of both the Dye and the NiO and the VBM-HOMO difference. Then, we analyze the AIMD simulation of the C343@NiO interface in aqueous solution and the role of the MD on the electronic properties of interface. Lastly, our Final Remarks are drawn in Section 3.3.

3.1 Computational Details

NiO is paramagnetic, but the most stable phase below the Neél temperature (525 K)[60] is the type-II Antiferromagnetic Phase (AFII) that induces a rhombohedral symmetry. All the calculations reported throughout this Chapter have been performed on the AFII phase. Following previous studies,[37, 61] we modeled the NiO bulk system starting from the experimental NiO rock-salt, that has a lattice constant of ~ 4.17 Å.

To build the surface slab, we cleaved the bulk structure along the (100) direction and we considered 6 layers in a (2 × 2) supercell. For the dye, to have direct comparison with the available experiments, we considered here the original C343 molecule, bearing the carboxylic acid as anchoring group. To model the adsorption of C343 onto the NiO surface we evaluated the binding energy in vacuo and at different level of theory for the bidentate anchoring with proton transfer to one surface oxygen, and two monodentate binding modes, in which the proton of the carboxylic acid is pointing toward the surface (H-DOWN) or toward the carbonyl oxygen of the coumarin (H-UP). See Figure 3.6.

Ground State optimizations for the C343, NiO (bulk and slab) and C343@NiO were performed using DFT with the PBE exchange and correlation functional and adopting a Hubbard term for the Ni(d) electrons. The latter was set equal to 4.6 eV following the value obtained by Cococcioni and de Gironcoli with their linear response method.[61] The C343 molecule has been considered into a parallelepiped rectangular cell having 10 Å of vacuo in each direction. Then, to correct the spurious electrostatic interactions, introduced by the periodicity, we applied a monopole/dipole/quadruple corrections to the total energy.

DFT and GW (G_0W_0) calculations were performed with the VASP[62–64] using the pseudopotentials constructed by the Projector Augmented Wave Method (PAW) [65] and a plane waves basis set. We used a cutoff of 650 eV for the NiO systems (bulk, slab and interfaces) and 600 eV for the isolated C343. The Brillouin zone for the NiO bulk was sampled using a $8 \times 8 \times 8$ K points grid centered in Γ, whereas for C343, NiO slab and the C343@NiO interface Γ point only has been considered. The G_0W_0 approximation consists in a perturbative correction of the DFT Kohn-Sham energies and has been demonstrated, as has already been discussed, to be highly dependent on the DFT starting point, i.e., on the considered functional.[66] Here, we apply the G_0W_0 correction on the KS energies computed from PBE+U calculations (G_0W_0@PBE+U), since as reported by Scheffler et. al., this approach delivers energy gaps in good agreement with experiments for most of the transition-metal monoxides, including NiO.[67] We set a GW cutoff (see Ref.[64] for further details) of 200 eV for both the isolated C343, the NiO slab and the C343@NiO interface and 433.3 eV for the NiO bulk system. More details about the convergence of GW calculations are discussed below.

Molecular dynamics (MD) simulations of the C343@NiO(100) interface in explicit water were performed with the CP2K code [68] using GTH norm conserving pseudopotentials, MOLOPT-DZVP basis set, 500 Ry cutoff for charge density and sampling the Brillouin zone at the Γ point. Also in this case we used the PBE+U approach, imposing U equal to 2 eV and adopting the Grimme's Van Der Waals corrections. The simulation box, having dimensions $8.35 \times 8.35 \times 33.40$ Å^3, consists of the C343@NiO interface and 42 water molecules. After an initial minimization that has been carried out for 200 step, the MD run was performed in the NVT ensemble by imposing the temperature to 360 K through the canonical sampling velocity rescaling thermostat.[69] The time step was set to 1 fs but imposing the deuterium mass for hydrogen atoms.

After equilibration (the first 3ps of the MD simulation), from the production run of $\sim$ 27 ps we extracted 20 configurations equally spaced in term of time, to perform single point PBE+U and G_0W_0@PBE+U calculations with the same set up discussed above for the C343@NiO interface in vacuo. From these calculations, we evaluate, by means of the Projected Density Of States (PDOS), the thermal averaged $E_{\mathrm{VBM}} - E_{\mathrm{HOMO}}$ and energy gaps for the dye and for the NiO slab.

3.2 Results and Discussion

3.2.1 Isolated systems in gas phase

NiO bulk

The experimental optical gap and the fundamental gap of NiO are reported in a wide energetic range, depending on the method used for the investigation. The optical gap is usually reported in the $3.1 - 4$ eV range where the onset of the absorption is located at about 3 eV and the first well-defined maximum is higher in energy at ca. 4 eV.[70–72] The fundamental gap measured through Photoemission Spectroscopy (PESp), for occupied states, and Bremsstrahlung-Isochromat Spectroscopy (BISp), for unoccupied state, is 4.3 eV [73], while a value of 4.0 eV was obtained from X-Ray Absorption (XAS) and Emission (XES).[74] It is well documented in the literature [61, 75, 76] that, like for many other transition metal

monoxides, the energy gap of NiO is dramatically underestimated at PBE level of theory and that, on the other hand, the combination with the Mott-Hubbard parameter U (PBE+U) delivers values closer to the experimental results. At the same

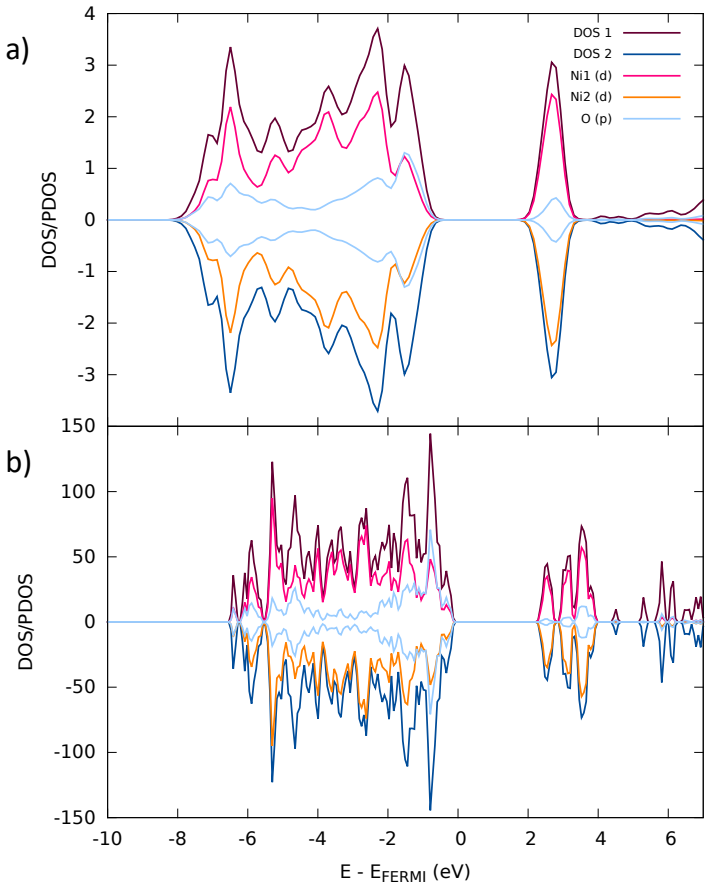

Figure 3.1: DOS and PDOS for the NiO bulk (a) and slab (b) computed at the PBE+U level. Positive and negative values represent the spin-up and the spin-down channel respectively.

time, the electronic structure of NiO is sensitive to the choice of the functional. Indeed, as discussed in previous works[61, 75–78], inclusion of the U term pushes down the d levels from the top of the Valence Band and promote the presence of mixed Ni(d)-O(p) states on the Valence Band Maximum (VBM), whereas, the Conduction Band Minimum (CBM) is dominated by Ni(d) states (Figure 3.1a).

As shown in Table 3.1, the NiO has an indirect band gap.[67, 76] Moreover, in

Method	Band Gap (eV)	
	direct	indirect
PBE+U	3.33 [T]	2.85 [T → 0.5 0.25 0.25]
G_0W_0@PBE+U	4.24 [T]	3.76 [T → 0.5 0.25 0.25]
Other theoretical work		
G_0W_0@LDA+U [67]	3.75	
G_0W_0@HSE03[79]	4.70	
Experiment		
$E_g^{PESp+BISp}$ [73]	4.3	
$E_g^{XAS+XES}$[74]	4.0	

Table 3.1: Direct and indirect band gaps (eV) of NiO rocksalt at PBE+U and GW@PBE+U level of theory compared with the experimental gap obtained from PES+BIS and XAS+XES and other theoretical studies. The K points involved in the band gaps are reported into squared brackets

both PBE+U and G_0W_0@PBE+U calculations, the same k points are involved in both the direct and indirect band gaps. As expected, the application of the GW correction on top of PBE+U notably improves the agreement with experiments (Table 3.1), increasing the band gap of about 0.9 eV (from 2.86 to 3.77 eV).

NiO (100) slab and C343

GW calculations for the NiO (100) slab (96 atoms) are extremely expensive and the convergence of the results depends on many variables. In particular, to get converged quasi-particles (qp) energies, and thus qp gaps, for 2D systems, the most important parameters to consider are: i) the vacuo space along the direction perpendicular to the exposed surface; ii) the number of empty bands and iii) the number of k points. Moreover, in the GW approach implemented in VASP, a key parameter is the cutoff used for the evaluation of the response function $\chi_q^0(G, G', \omega)$ that determines the number of G vectors used in the GW calculation (GW cutoff).

The PBE+U calculations have been found to be weakly affected by the vacuo space due to the semilocal nature of the electrostatic interactions of the GGA functionals; this guarantees also the convergence with respect to the energy cutoff, i.e. there is a negligible effect by increasing the number of plane waves. Conversely, it remarkably influences the convergence of the GW calculations due to the long range nature of the screened Coulomb interactions.[80] Here we consider Γ point

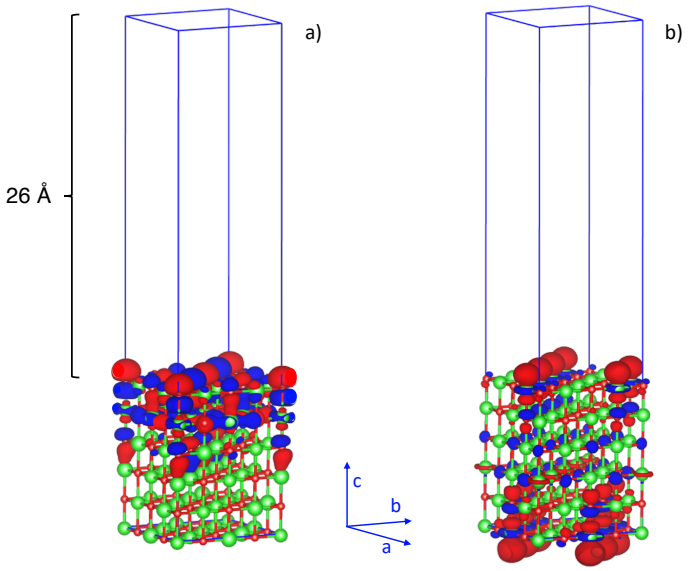

Figure 3.2: Calculated isosurfaces of the VBM (a) and CBM (b) Kohn-Sham orbitals of the NiO slab system considering 26 Å of vacuo space.

only and we set up a 2-dimensional convergence approach considering at the same time the dependence on the vacuo space and on the empty bands. Thus, starting from 14 Å of vacuo space along c direction (see Figure 3.2) and 1200 bands (816 empty bands) we increase these parameters up to 26 Å and 1600 bands (1216 empty bands) where we estimated that convergence was reached for both the qp gap and qp energies (see Figures 3.3-3.5). The converged PBE+U and GW gaps are reported in Table 3.2, where one can notice that for the slab these values are lower than the ones obtained for the bulk in Table 3.1. In fact, even though the PDOS of the NiO slab has a similar nature to the one of the bulk (Figure 3.1b), in the slab the band edges are dominated by surface states (Figure 3.2), as a consequence of the under-coordination of the atoms on the two surface layers.[81–83]

We also computed the Ionization Potential (IP) and the Electron Affinity (EA), see Table 3.2, of the slab as the negative of the value of the VBM and CBM Kohn Sham (KS) eigenvalues and qp energies relative to vacuo level (r.t.v.). [86]. The experimental value of the VBM usually reported is -5 eV r.t.v.,[84] although, as

Method	E_g	IP	EA
NiO(100)			
PBE+U	2.57	5.49	2.92
G_0W_0@PBE+U	3.47	5.02	1.56
Exp.[84]		~ 5	~ 1.8
C343			
PBE	2.06	5.74	3.68
G_0W_0@PBE	6.05	6.58	0.53
evGW@LDA [85]	6.61	7.21	0.60

Table 3.2: Energy gap, Ionization Potential (IP) and Electron Affinity (EA) in eV for the NiO (100) slab and the C343 dye computed using PBE+U and G_0W_0@PBE+U

for the band gap, it depends on the adopted measurement technique. Indeed, this varies from the -4.8 eV (PES)[87] to -5.0 eV (electrochemical measurement)[84, 88] to -5.8 eV (thermionic emission)[89]. Measured EAs are not available for NiO, so the experimental EA values are obtained by subtracting the experimental band gap from the experimental IP. Clearly, the spread in the VBM as well as in the band gaps values makes this estimation quite uncertain and, here, for the sake of simplicity, we refer to the value of -1.8 eV,[84] since it is the one more frequently reported in the literature. The GW correction (Table 3.2) notably improves the agreement with experiments, predicting IP and EA values of 5.02 and 1.55 eV, respectively. In particular, as reported for a large set of Semiconductors,[90] GW reduces the over-stabilization of the IP and, in particular, the EA obtained at DFT level.

Then, for the C343 molecule, from the PBE and the G_0W_0@PBE calculations we computed the E_g and the IP and EA, by considering the HOMO and LUMO KS values with respect to the electrostatic corrected potential in the vacuo region averaged over the three a,b,c directions. As far as we know there are no reported experimental IP and EA for C343 in gas phase, so here we compare our results with those reported by Blase and co-workers[85] obtained by partially self consistent GW (evGW) on the top of LDA calculation. Values in Table 3.2 show an overall good agreement between our G_0W_0 values and the more accurate evGW ones. In both cases the energy gap is very different from the C343 optical absorption, that, in apolar solvent (ciclohexane) shows an absorption maxima at ca. 3 eV therefore

evidencing an huge exciton binding energy.[85, 91]

It is important to stress that, as discussed in Section 3.1, the calculations on the C343 the NiO slab and the C343@NiO interfaces, which will be reported in the next sections, have been carried out with a different GW cutoff compared to the one of the NiO bulk system. However, as shown in Table 3.3, the use of the same GW setup as the one used for the such systems, is giving only negligible difference in the calculated direct and indirect energy gap for the NiO bulk system.

In this section we validate our methodology considering the standalone elements of the C343@NiO interface finding an overall good agreement with the available experimental data and with other theoretical investigations. In the next section we will address the study of the C343@NiO interface.

Method	Band Gap (eV)	
	direct	indirect
PBE+U	3.33 [T]	2.85 [T → 0.5 0.25 0.25]
G_0W_0@PBE+U	4.29 [T]	3.81 [T → 0.5 0.25 0.25]

Table 3.3: Direct and indirect band gaps (eV) of NiO rocksalt at PBE+U and GW@PBE+U level of theory. The GW@PBE+U calculation has been carried out adopting a GW cutoff equal to 200 eV.

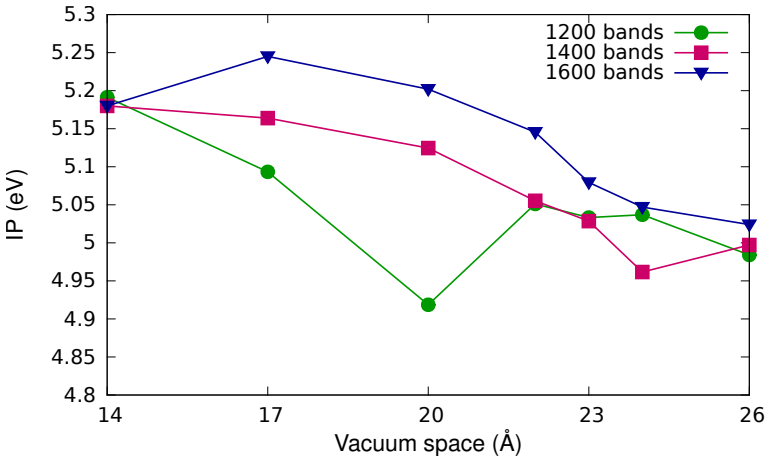

Figure 3.3: Calculated GW Ionization Potential (IP) of NiO(100) slab as a function of the vacuo space and of the number of the considered KS bands.

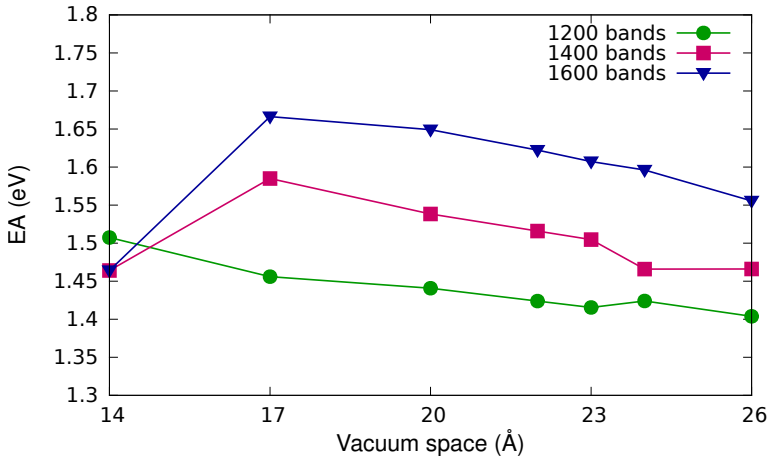

Figure 3.4: Calculated GW Electron Affinity (EA) of NiO(100) slab as a function of the vacuo space and of the number of the considered KS bands.

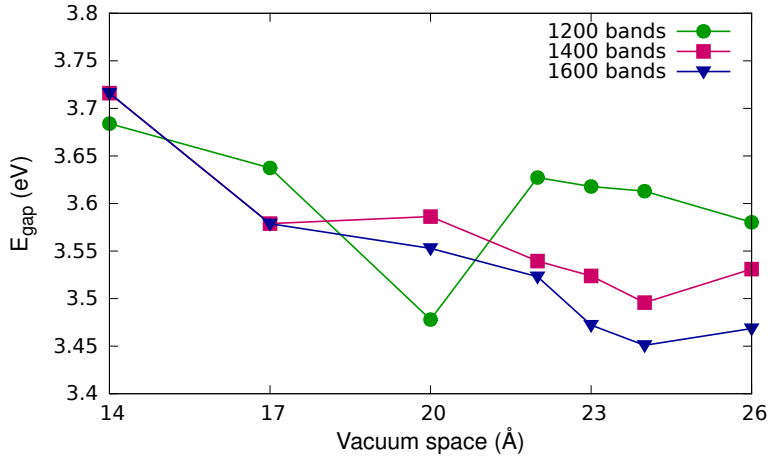

Figure 3.5: Calculated GW band gap of NiO(100) slab as a function of the vacuo space and of the number of the considered KS bands.

3.2.2 C343@NiO Interface in vacuo

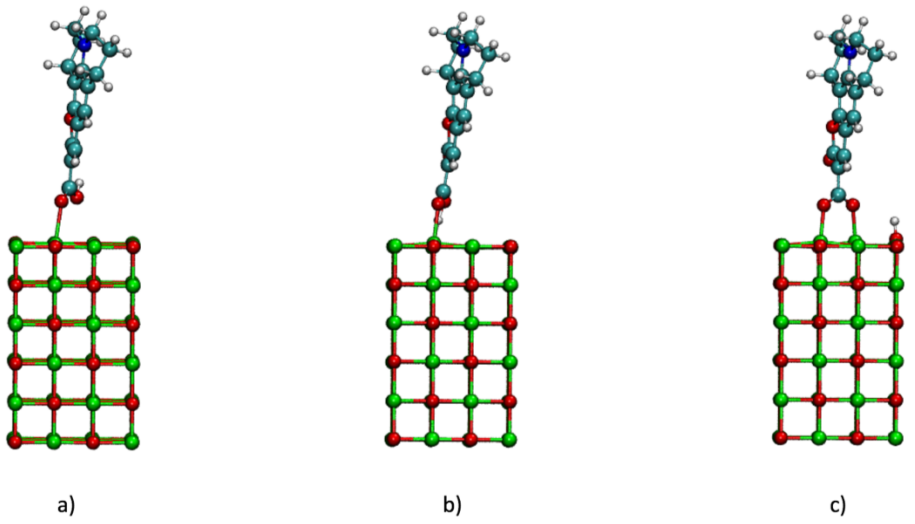

Figure 3.6: Optimized structures of the C343@NiO system in monodentate H up (a) monodentate H down (b) and bidentate (c) modes in vacuo.

To investigate how C343 binds on the NiO (100) surface, we computed, for the C343@NiO system, the binding energies for both monodentate and bidentate. In particular, the monodentate can exist in two distinct forms depending on whether the hydrogen of the carboxylic group makes H-bond with the NiO surface (H-down) or with the carbonyl oxygen of the C343 (H-up) (Figure 3.6).

Method	BINDING MODE		
	monodentate		bidentate
	H-UP	H-DOWN	
PBE	-0.082	-0.347	-0.455
PBE + U	-0.049	-0.373	-0.353
PBE + U (Grimme)	-0.565	-0.919	-0.880
PBE + U (Grimme 1L)	-0.474	-0.825	-0.814

Table 3.4: Binding energies in eV obtained from the optimized PBE+U geometries considering different binding modes, namely monodentate and bidentate, and different methods

We calculated the binding energy ($E_{Binding} = -(E^{opt}_{C343@NiO(100)} - E^{opt}_{C343} - E^{opt}_{NiO(100)})$) at different level of theory, namely PBE, PBE+U and the PBE+U combined with

the popular Grimme's D3 correction. The latter was adopted within two different approaches: considering the D3 corrections on the whole system (molecule + slab) or applying these corrections only to C343 and the first NiO layer (where the dye is grafted) (Grimme 1L). As shown in Table 3.4 the bidentate mode is more stable than the H-UP monodentate binding mode. On the other hand, the binding energies between the bidentate mode and the H-DOWN monodentate mode are very similar. However, given the small difference found between the H-DOWN and the bidentate modes, following previous findings[37, 39], we considered the C343 dye anchored in a bidentate fashion (Figure 3.7a) to the (100) NiO surface slab for the following investigations.[37] Moreover, in accordance with other studies [92, 93], to account for Van der Walls interactions for the subsequent MD simulations, we consider the Grimme 1L approach, since it delivers binding energy similar to the one reported in the literature for the same system.[39]

In order to remove spurious interactions between periodic images we imposed a vacuo space of ca. 26 Å between the two surfaces of NiO and we introduced the monopole/dipole/quadrupole correction within the vacuo region (along the c direction). Then, we considered a number of bands that meets the same ratio between occupied and unoccupied KS bands found in the converged calculations on the isolated slab, namely 1800 bands (i.e. 1362 empty bands). As shown by the isodensity plots in panels b and c of Figure 3.7, dye's HOMO and the NiO's VBM present a negligible electronic coupling,[37] being the electron density strongly localized on the molecule and on the slab, respectively. Thus, once identified the C343 HOMO/LUMO and the VBM/CBM bands by means of the PDOS (Figure 3.8), the energy alignment between the frontiers KS orbitals, the energy gaps and driving forces for the hole injection can be straightforwardly obtained (Figure 3.9) and compared with the one given by the calculations on the isolated dye and Semiconductor slab (Table 3.2). Let us first discuss the results obtained from the PBE+U calculation (top panel in Figure 3.9). NiO's gap calculated when the dye is grafted on the surface turns out to be $\sim$ 0.1eV smaller than the one obtained for the isolated slab, due to a larger upshift of the VBM with respect to the CBM. Being the VBM and the CBM mainly decoupled from dye's states, this phenomenon might be due to the interfacial electric dipole and the slab distortion that are promoted by the dye and proton adsorption on the surface. On the other

hand, the calculated HOMO/LUMO gap of the dye increases ($\sim$ 0.3eV) when the dye is anchored on the slab, as the consequence of a sizeable destabilization of the LUMO. This effect is due to geometrical distortion of the C343 structure driven by the bonds with the Ni atoms of the NiO surface, the C343 deprotonation and interactions between periodic images along the a and b directions.[58] However, the latter are not to be regarded as spurious because the surface dye concentration that we represent in our interface ($\sim$ 1 molecule/ 0.70 nm^2) model is in line with the typical experimental surface coverage employed in DSSCs.[94, 95] As far as the VBM-HOMO difference is concerned, a slightly negative (-0.35 eV) driving force, impeding the hole injection process, is predicted for the interface in gas phase, whereas by taking the HOMO and VBM values calculated for the isolated systems, this difference is positive and amounts to 0.24 eV.

The G_0W_0 correction (bottom panel in Figure 3.9), as already discussed for the standalone components, brings about a sizeable increase in the energy gaps and relevant differences in the electronic structure (Figure 3.8). The NiO gap (that now turns out to be the gap of the interface system) results to be, again, close

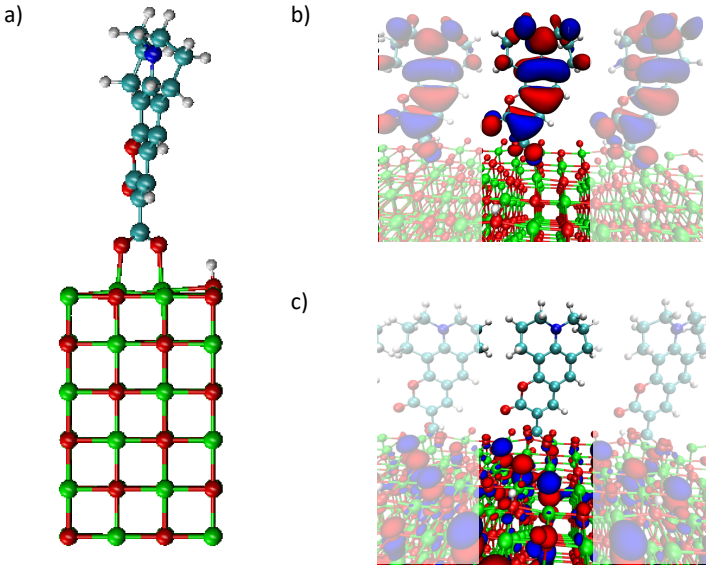

Figure 3.7: Optimized C343@NiO system in gas phase a) and isodensity plots of the dye's HOMO (b) and NiO's VBM (c) Kohn-Sham orbitals.

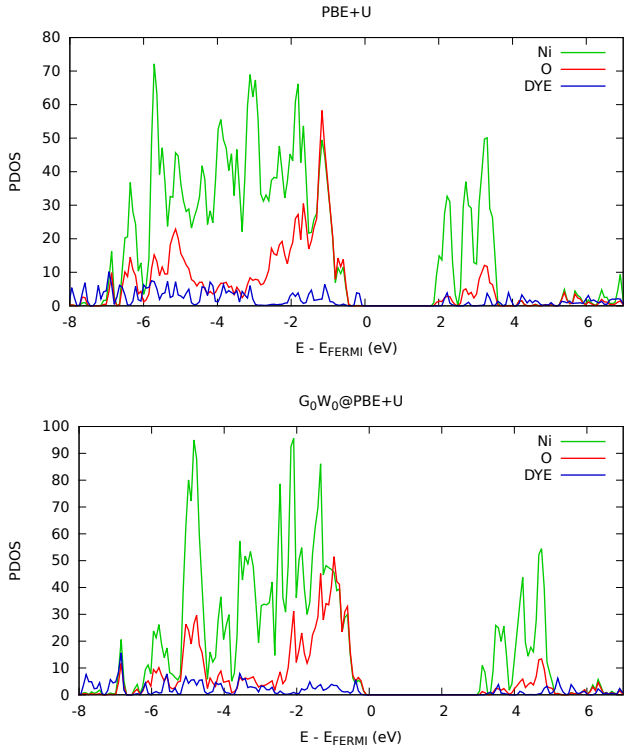

Figure 3.8: DOS and PDOS for the C343@NiO interface computed at the PBE+U level (top panel) and at G_0W_0@PBE+U level (bottom panel) considering the spin-up channel

to the gap calculated on the isolated slab and the small decrease ($\sim$ 0.1eV) is mainly due to the stabilization of the CBM. On the other hand, the qp Dye's gap is significantly (about 2 eV) reduced compared the one obtained from the isolated molecule. This marked gap reduction predicted from the GW calculation, has been already reported for comparable interface systems[58, 96] and depends on image charge effects that are not correctly described at the bare DFT level, where the gap is usually unchanged when going from the isolated molecule to the molecule at the interface.[54, 55, 96] Moreover, these effects reduce also the exciton binding energy, as shown by Garcia-Lastra et. al. for molecule physisorbed on metallic surfaces,[55] and produce a qp gap much more similar to the experimental optical one that has been reported in Section 3.2.1. The most striking result coming from the G_0W_0 correction, however, concerns the relative alignment between the C343's HOMO and the VBM of the adsorbed system (bottom panel in Figure 3.9). At

GW level, indeed, the sign of the driving force is inverted with respect to the DFT results, and now a slightly positive value of 0.19 eV is obtained. This is the result of a differential perturbative correction on the dye's and NiO states, coming from the different nature of the qps, as quantified by the difference in the Z renormalization factors calculated for the C343 ($\sim$ 0.8) and the surface slab

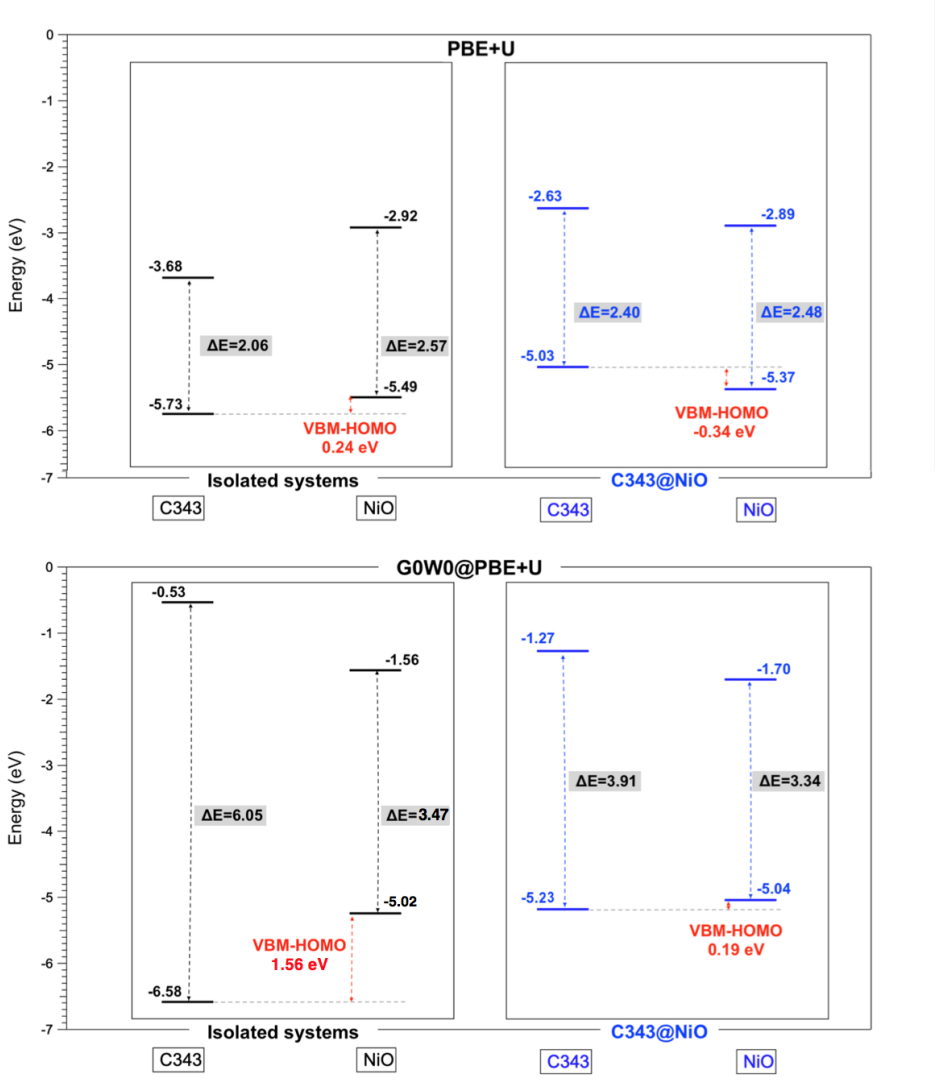

Figure 3.9: PBE+U (top panel) and G_0W_0@PBE+U (bottom panel) energy levels with respect to the vacuo of the C343 HOMO/LUMO and NiO VBM/CBM as computed for the isolated systems (data in Table 3.2) and for the C343@NiO interface model. The band gaps and driving forces for the hole injection from the dye to the Semiconductor (VBM-HOMO) are also reported.

(0.6-0.7) qps.[67, 97, 98] It is worth to stress here that this change in the dye and Semiconductor relative energy levels alignment cannot be attained by using hybrid functionals, since they only produce an opening of the energy gap of the interface system, without altering the lining up between the molecule and Semiconductor KS eigenvalues, thus delivering very similar driving forces.[37]

To sum up, here we have shown that GW calculations on the model dye/SC system in gas phase can recover the correct interfacial energetics, which is missed at DFT+U level. As we shall discuss in the next section, inclusion of the explicit solvation effects will further refine our picture, allowing for a quantitative comparison with experiments.

3.2.3 C343@NiO interface in water

Dye sensitizers bearing carboxylic anchoring groups are often prone to undergo desorption from metal oxides surfaces in water environment[99, 100] and the use of phosphonic acid group is, usually, recommended to guarantee a better long-term stability of the cell. Water chemisorption on NiO and on other oxyde SCs is indeed a well-known phenomenon, reported by both experimental and theoretical investigations[101–103] and the competitive adsorption between water molecules and carboxylates at the metal oxide interface is the reason for the observed dye desorption.[99, 104]. However, since here we aim at refining the electronic structure description by benchmark our GW results against experimental data, we considered the original C343-COOH dye, for which the solvation and finite temperature effects on the energetics of the components of the interface have been experimentally investigated.

The first point to assess is, therefore, the stability of C343 on the NiO surface. Along the 30 ps trajectory we did not observe dye desorption, although a dynamic interconversion between the bidentate and monodentate anchoring, driven by thermal fluctuations and by the interaction with the surrounding water molecules, as shown by the distance fluctuations of one of the two Ni-O bonds in Figure 3.10. Along the MD run we observed, indeed, dissociative adsoprtion (H^+ and OH^-) of two water molecules, one for each face of the NiO slab. As evidenced by the interatomic pair distribution function ($g_{\alpha\beta}(r)$) in Figure 3.11 between the hydrogen

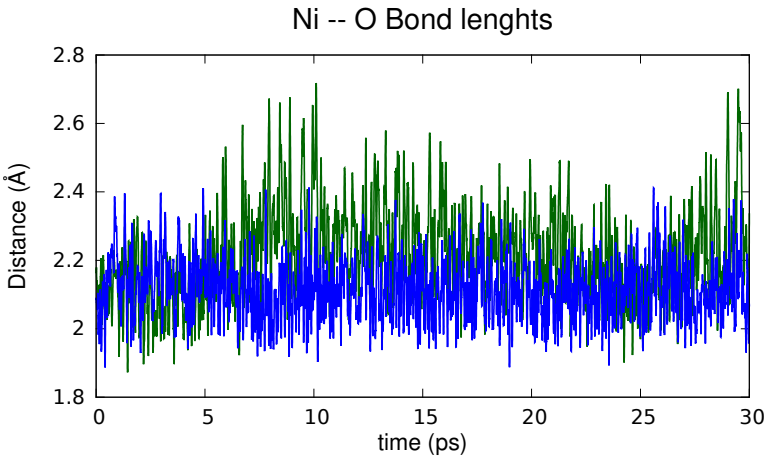

Figure 3.10: Ni-O Bond Distances computed along the whole MD run

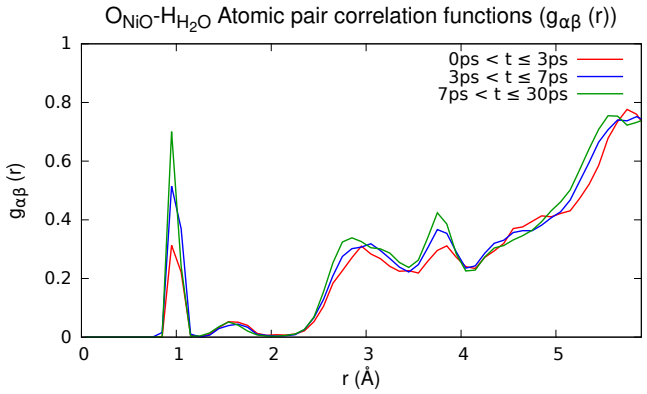

Figure 3.11: Atomic pair correlation functions ($g_{\alpha\beta}$(r)) computed between the nichel atoms of the NiO surfaces and the hydrogen atoms belonging to the water molecules. The $g_{\alpha\beta}$(r) have been computed along the equilibration phase (0ps < t < 3ps) and two time interval along the MD production run (3ps < t ≤ 7ps and 7ps < t ≤ 30ps)

atoms of the water molecules and the NiO oxygen atoms, within the first ∼ 3ps one of the two water molecules is already chemisorbed, giving rise to the peak at 1 Å; the second water molecule, the one at the C343/NiO interface, is adsorbed after 6-7 ps, as evidenced by the increase in the intensity of the peak of the $g_{\alpha\beta}(r)$ in the time interval 3-7 picoseconds. Those water molecules, as evidenced by the intense narrow peak at 1 Å present in the $g_{\alpha\beta}(r)$ computed over the last part of the dynamics (7ps < t ≤ 30 ps), remain stable adsorbed on the NiO surfaces. As a consequence, the oxydril at C343/NiO interface interacts with the anchoring unit

of C343 (see Figure 3.12), inducing the elongation of the Ni-O bond observed in Figure 3.10.

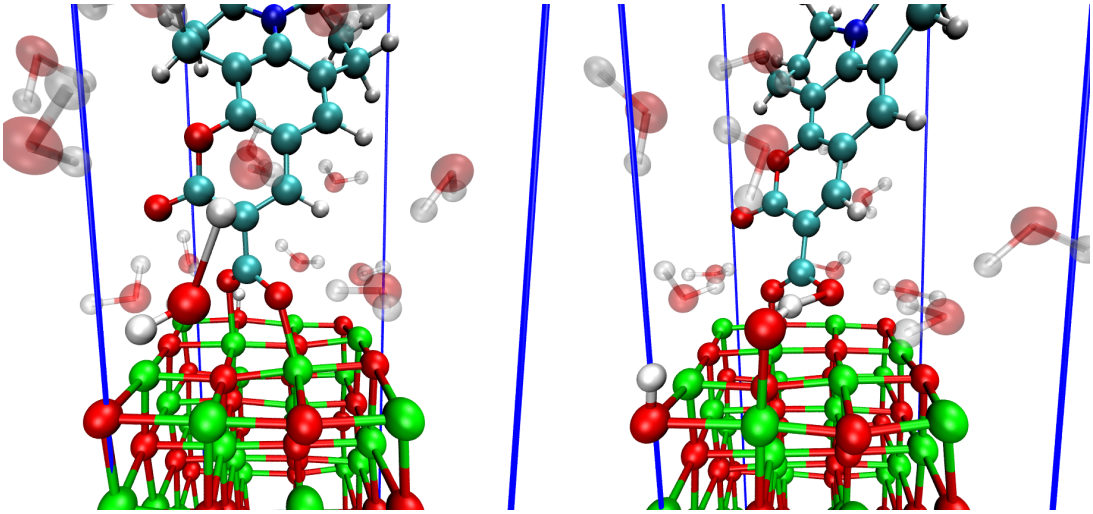

Figure 3.12: Two snapshots extracted from the MD trajectory at 0.5 ps (Left) and 7 ps (Right) showing the water chemisorption at the C343@NiO interface.

In order to analyze in detail the role of the solvent on the electronic properties of C343@NiO, we considered a snapshot extracted at the early stages of the MD production run (after 3 ps). For the GW calculations we used the same set up adopted for the interface in gas phase by considering the same ratio between occupied and unoccupied bands needed to converge the calculations on the NiO slab (2500 KS bands with 1890 empty bands). Figure 3.13 shows that the dye's levels and the NiO's bands are electronically decoupled also in aqueous environment, so the energy gaps and the driving force can be easily obtained by peaks in the PDOSs.

As shown in ref.[37], explicit solvation has a major effect on the interfacial energetics (Table 3.5), by relatively shifting the levels of the dye and of the NiO slab in the direction of increasing the driving force for the hole injection.

Table 3.5 reports these gaps highlighting an important solvent effects resulting in a decrease of the band gaps for both the components of the system. As is apparent in Table 3.5, indeed, already at PBE+U level, the driving force is positive, passing from -0.34 eV, for the optimized interface in vacuo (top panel of Figure 3.9), to

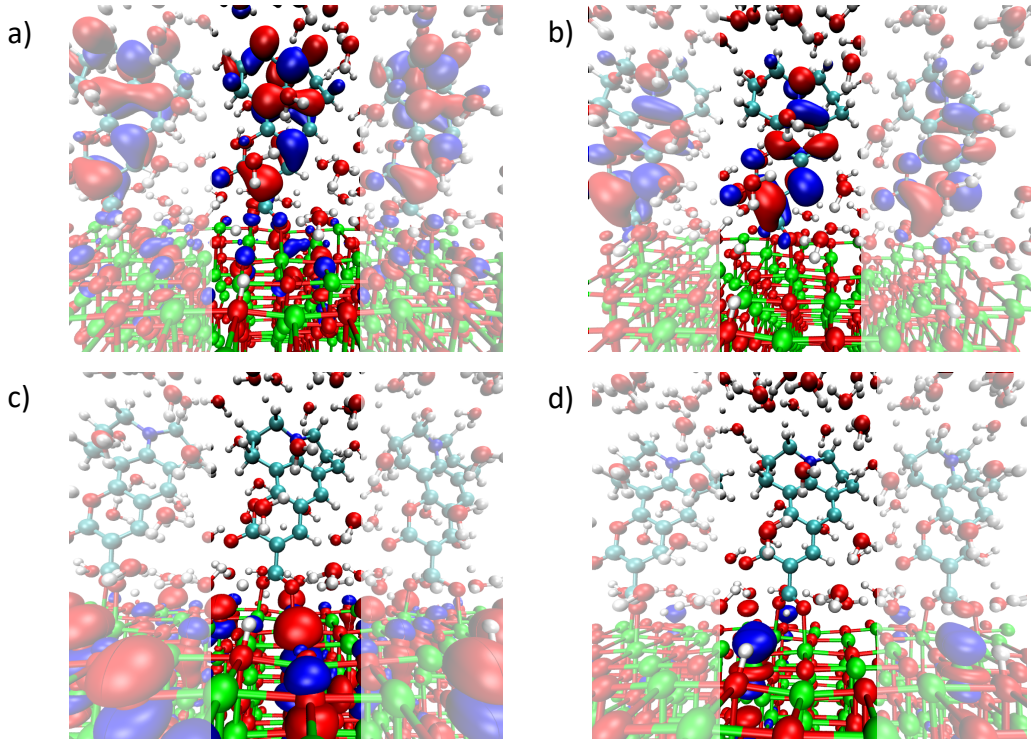

Figure 3.13: Calculated isosurfaces of the HOMO (a),LUMO (b), VBM (c) and CBM (d) Kohn-Sham orbitals of the Interface system in water solution calculated from a snapshot extracted at the early stage of the MD simulation

+0.39 eV. A larger driving force with respect to the one calculated in vacuo (bottom panel of Figure 3.9) is also obtained at GW level of theory, where the calculated VBM-HOMO difference is 0.6 eV, quantitatively agreeing with the experimental estimation of the driving force.[45, 46] It is important, however, to stress here that no photoelectron spectroscopy measurements on the dye-sensitized interface are available and that the driving force is estimated using the red-ox potentials of isolated C343 and NiO. We also note that dye's energy gap is now in excellent agreement with the experimental optical one measured for the C343 adsorbed on NiO surface in ethanol solution[45] evidencing, as discussed in section 3.2.2, a decrease of the exciton binding energy that appears to be further promoted by solvent polarization effects.[55]

To learn more on the role of the solvent at the dye/NiO interface, we can try to

Method	E_g^{DYE}	E_g^{NiO}	VBM − HOMO
PBE+U	2.10	2.39	0.39
G_0W_0@PBE+U	3.34	3.46	0.60
Experiment			
EXP	$\sim$ 3.0[45]		0.6[44]-1.0[46]
without water molecules			
PBE+U	2.32	1.76	0.27
G_0W_0@PBE+U	3.67	2.70	0.37

Table 3.5: Calculated Dye's gap (LUMO-HOMO), NiO's gap (CBM-VBM) and driving force (VBM-HOMO) in eV for the 3ps-snapshot of the NiO interface with and without explicit water molecules computed at PBE+U and G_0W_0@PBE+U levels of theory

disentangle the mechanical embedding effects from the electrostatic and polarization ones. To quantify the effect of the geometrical distortions, we calculated the electronic structure of the same snapshot, the one extracted at 3 ps, but removing all water molecules and applying the monopole/dipole and quadrupole correction in the middle of the vacuo space to determine the reference vacuo level. The resulting driving forces and energy gaps (data "without water molecules" in Table 3.5) are rather different from the ones calculated from the optimized structure in vacuo (Figure 3.9), with an overall reduction of the gaps, and a driving force going from -0.34 and 0.19 eV to 0.27 and 0.37 eV at PBE+U and G_0W_0@PBE+U level, respectively. If we compare these driving forces with the those discussed above and calculated on the explicitly solvated interface, interestingly we disclose that the mechanical effect dominate the electrostatic and polarization effects, already accounting for about 70% and 60% of the total driving force calculated by DFT+U and GW, respectively. By looking at the absolute values of the calculated KS and qp energies (Table 3.6) and comparing them with those depicted in Figure 3.9, we can trace-back the changes on the NiO gaps mainly to the downshift of the CBM (about 0.6 eV) that, being localized on the surface (see Figure 3.7c) is strongly affected by the distortion of the first layer of the slab caused by the interaction with the adsorbed water molecules. The Root Mean Square Deviations (RMSD) for the atoms belonging to the first layer, calculated respect to the optimized interface in vacuo, is indeed higher (0.16 Å) compared to the one computed for the second (0.11 Å) and the third layer (0.10 Å). Concerning the dye, we note a larger stabilization of the LUMO with respect to the HOMO, thus inducing the decrease

of the energy gap.

Method	HOMO	LUMO	VBM	CBM
PBE+U	-5.48	-3.16	-5.21	-3.44
G_0W_0@PBE+U	-5.36	-1.69	-4.99	-2.30

Table 3.6: Dye's HOMO, LUMO and NiO's VBM, CBM in eV (r.t.v.) for the 3ps-snapshot of the C343@NiO interface "without water molecules" computed at PBE+U and G_0W_0@PBE+U levels of theory

Having rationalized the effect of the solvent at the dye/NiO interface on the initial configuration (i.e., the snapshot extracted after 3 ps), we can move to discuss the energy level alignment along the whole trajectory. To do that we considered 20 snapshots, equally spaced in term of time from the MD production run, and we performed PBE+U and G_0W_0@PBE+U calculations on the full solvated interface model. The time evolution of the calculated driving force and energy gaps are plotted in Figure 3.14, while the values with the corresponding standard deviation and standard error are listed in Table 3.7 along with those obtained considering only 10 snapshots. The small differences found between the two samplings reveal that the convergence of the calculated properties has been already reasonably achieved with 20 snapshots. It is meaningful to compare the thermal-averaged quantities with those of the static picture at the beginning of the MD simulations.

Along the dynamics, we observe an overall band gap shrinkage for both dye and NiO, with larger fluctuations at GW level of theory. Interestingly, as shown by panels a) and b) in Figure 3.14, while for the NiO slab the gap evolution at GW level approximately follows the PBE+U one, the correlation between the DFT and the GW corrected values appears less evident for the dye, where the GW results are more scattered. The QP NiO band gap calculated over the MD trajectory is 3.43 $\pm$ 0.27 eV, in better agreement with the experiments.[46] The same applies for the dye: the QP gap is slightly smaller compared to the static picture discussed above (3.25 $\pm$ 0.18), therefore it remains smaller than the gap calculated in the gas phase, evidencing a bathochromic shift in agreement with experimental evidence.[91]

The most interesting result, however, concerns the VBM-HOMO differences (Figure 3.14c). We find that the driving force for hole injection is always significantly larger at GW level (average value of 0.62 $\pm$ 0.28 eV) compared to the values obtained with PBE+U (average value of 0.36 $\pm$ 0.32 eV), and in quantita-

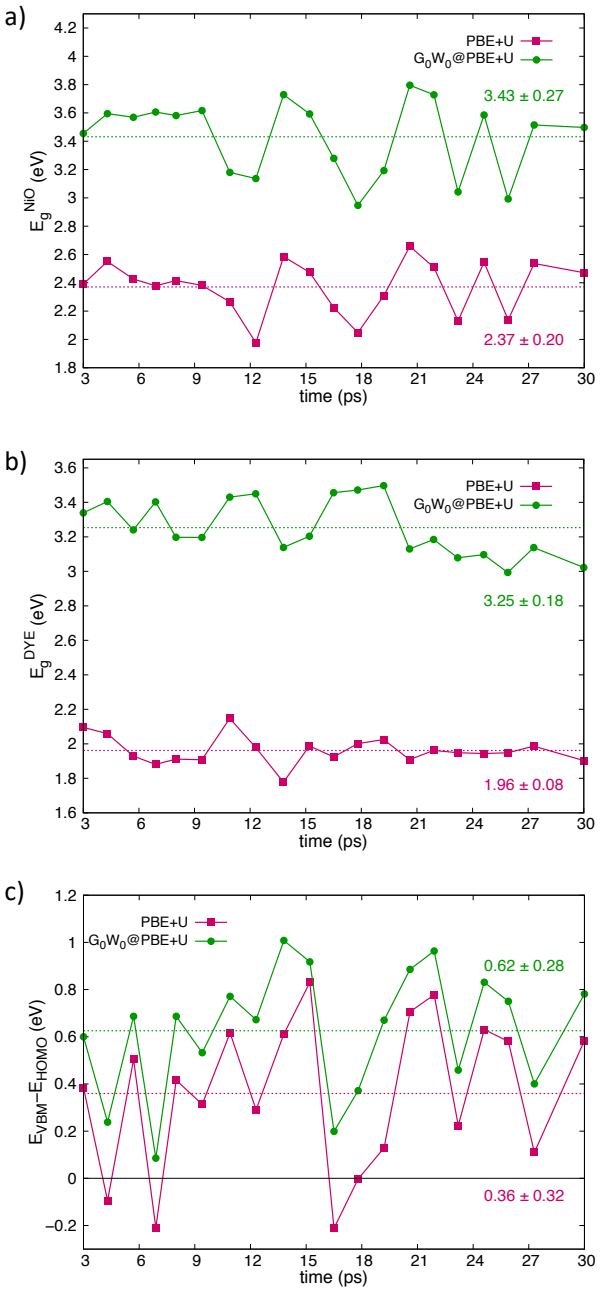

Figure 3.14: Calculated NiO's gap (a), Dye's gap (b) and difference between the VBM of the NiO and the HOMO of the Dye (c) along the MD production run in eV considering both the PBE+U and the G_0W_0@PBE+U methods.

Method	E_g^{DYE}	E_g^{NiO}	VBM − HOMO
	10 snapshots		
PBE + U	1.97 ± 0.11 [0.035]	2.38 ± 0.18 [0.057]	0.37 ± 0.32 [0.101]
G_0W_0@PBE+U	3.30 ± 0.15 [0.047]	3.51 ± 0.21 [0.066]	0.62 ± 0.29 [0.092]
	20 snapshots		
PBE + U	1.96 ± 0.08[0.018]	2.37 ± 0.20 [0.045]	0.36 ± 0.32 [0.072]
G_0W_0@PBE+U	3.25 ± 0.18 [0.040]	3.43 ± 0.27 [0.060]	0.62 ± 0.28 [0.063]

Table 3.7: Energy gaps and VBM-HOMO difference in eV calculated using time averages over either 10 or 20 snapshots, equally spaced in time, extracted from the MD run of the C343@NiO in explicit water with relative standard deviations and standard errors that are reported into squared brackets.

tive agreement with the experimental estimation in the range 0.6-1.0 eV. More in detail, the GW driving force is always positive, i.e. favourable for hole injection, and oscillates between $\simeq$ 1 eV and $\simeq$ 0.1 eV. The GW correction is also very different from one snapshot to the other, going from 0.1 to 0.6 eV. It is worth noting that in ref.[37] the driving forces obtained by using the hybrid HSE06 functional were in the same range of the PBE+U ones, differing by less than 0.1 eV, due to a similar effect on both the VB of NiO and on the HOMO of the dye.

3.3 Final Remarks

By considering a simplified, albeit realistic model, of a dye-sensitized NiO interface (C343@NiO(100)), we have shown, that GW calculations, coupled to AIMD simulations in explicit solvent, are capable to deliver, in quantitative agreement with experiments, the interfacial energy-level alignment required for the functioning of p-type photocathodes. If on one hand, indeed, the alignment is mostly affected by electrostatic and mechanical effects induced by the dye anchoring and by the solvent (water) layer adsorbed to the surface, the accuracy of the employed electronic structure method is, on the other hand, crucial to get a quantitative estimation of the energy difference between the NiO VBM and the dye's HOMO (i.e. the driving force for the hole injection process). Image charge effects, dynamical effects and solvent polarization effects plays a key role in dictating the properties of the C343@NiO interface, by strongly affecting the dye and NiO energy gaps, and cannot be neglected when estimating from first principles the optoelectronic of these

photoactive hybrid interfaces. To conclude, in this chapter, we have shown the feasibility of accurate large scale GW calculations on realistic models of dye-sensitized metal oxide interfaces, including solvent molecules and finite temperature effects.

Bibliography

[1] B. O'Regan, M. Grätzel, *Nature* **1991**, *353*, 737–740.

[2] C.-P. Lee, C.-T. Li, K.-C. Ho, *Mater. Today* **2017**, *20*, 267–283.

[3] V. Nikolaou, A. Charisiadis, G. Charalambidis, A. G. Coutsolelos, F. Odobel, *J. Mater. Chem. A* **2017**, *5*, 21077–21113.

[4] J. He, H. Lindström, A. Hagfeldt, S.-E. Lindquist, *J. Phys. Chem. B* **1999**, *103*, 8940–8943.

[5] J. Gong, J. Liang, K. Sumathy, *Renew. Sust. Energ. Rev.* **2012**, *16*, 5848–5860.

[6] M. Pastore, F. De Angelis, *Top. Curr. Chem.* **2014**, *352*, 151–236.

[7] K. Kakiage, Y. Aoyama, T. Yano, K. Oya, J.-i. Fujisawa, M. Hanaya, *Chem. Commun.* **2015**, *51*, 15894–15897.

[8] C. Lee, W. Yang, R. G. Parr, *Phys. Rev. B* **1988**, *37*, 785–789.

[9] A. Renaud, L. Cario, Y. Pellegrin, E. Blart, M. Boujtita, F. Odobel, S. Jobic, *RSC Adv.* **2015**, *5*, 60148–60151.

[10] E. Benazzi, J. Mallows, G. H. Summers, F. A. Black, E. A. Gibson, *J. Mater. Chem. C* **2019**, *7*, 10409–10445.

[11] T. Jiang, M. Bujoli-Doeuff, Y. Farré, Y. Pellegrin, E. Gautron, M. Boujtita, L. Cario, S. Jobic, F. Odobel, *RSC Adv.* **2016**, *6*, 112765–112770.

[12] X. Zhang, T. Peng, S. Song, *J. Mater. Chem. A* **2016**, *4*, 2365–2402.

[13] J. Warnan, J. Gardner, L. Le Pleux, J. Petersson, Y. Pellegrin, E. Blart, L. Hammarström, F. Odobel, *J. Phys. Chem. C* **2014**, *118*, 103–113.

[14] B. D. Sherman, M. V. Sheridan, K.-R. Wee, S. L. Marquard, D. Wang, L. Alibabaei, D. L. Ashford, T. J. Meyer, *J. Am. Chem. Soc.* **2016**, *138*, 16745–16753.

[15] S. Wrede, H. Tian, *Phys. Chem. Chem. Phys.* **2020**, *22*, 13850–13861.

[16] C. E. Creissen, J. Warnan, D. Antón-García, Y. Farré, F. Odobel, E. Reisner, *ACS Catal.* **2019**, *9*, 9530–9538.

[17] L. D'Amario, G. Boschloo, A. Hagfeldt, L. Hammarström, *J. Phys. Chem. C* **2014**, *118*, 19556–19564.

[18] F. Odobel, Y. Pellegrin, E. Gibson, A. Hagfeldt, A. Smeigh, L. Hammarström, *Coord. Chem. Rev.* **2012**, *256*, 2414–2423.

[19] L. Zhang, L. Favereau, Y. Farré, E. Mijangos, Y. Pellegrin, E. Blart, F. Odobel, L. Hammarström, *Phys. Chem. Chem. Phys.* **2016**, *18*, 18515–18527.

[20] L. J. Antila, P. Ghamgosar, S. Maji, H. Tian, S. Ott, L. Hammarström, *ACS Energy Lett.* **2016**, *1*, 1106–1111.

[21] A. M. Brown, L. J. Antila, M. Mirmohades, S. Pullen, S. Ott, L. Hammarström, *J. Am. Chem. Soc.* **2016**, *138*, 8060–8063.

[22] A. L. Smeigh, L. L. Pleux, J. Fortage, Y. Pellegrin, E. Blart, F. Odobel, L. Hammarström, *Chem. Commun.* **2012**, *48*, 678–680.

[23] X. L. Zhang, F. Huang, A. Nattestad, K. Wang, D. Fu, A. Mishra, P. Baüerle, U. Bach, Y.-B. Cheng, *Chem. Commun.* **2011**, *47*, 4808–4810.

[24] X. L. Zhang, Z. Zhang, D. Chen, P. Baüerle, U. Bach, Y.-B. Cheng, *Chem. Commun.* **2012**, *48*, 9885–9887.

[25] K. L. Materna, A. M. Beiler, A. Thapper, S. Ott, H. Tian, L. Hammarström, *ACS Appl. Mater. Interfaces* **2020**, *12*, 31372–31381.

[26] S. M. McCullough, J. M. Evans, T. Moot, A. D. Taggart, L. Troian-Gautier, J. F. Cahoon, *ACS Appl. Energy Mater.* **2020**, *3*, 1496–1505.

[27] M. Pastore, F. De Angelis, *J. Am. Chem. Soc.* **2015**, *137*, 5798–5809.

[28] P. Umari, E. Mosconi, F. De Angelis, *Sci. Rep.* **2014**, *4*, 4467.

[29] J. Preat, D. Jacquemin, E. A. Perpéte, *Energy Environ. Sci.* **2010**, *3*, 891–904.

[30] N. Martsinovich, A. Troisi, *Energy Environ. Sci.* **2011**, *4*, 4473–4495.

[31] S. Powar, D. Xiong, T. Daeneke, M. T. Ma, A. Gupta, G. Lee, S. Makuta, Y. Tachibana, W. Chen, L. Spiccia, Y.-B. Cheng, G. Götz, P. Bäuerle, U. Bach, *J. Phys. Chem. C* **2014**, *118*, 16375–16379.

[32] Y. Shao, J. M. de Ruiter, H. J. M. de Groot, F. Buda, *J. Phys. Chem. C* **2019**, *123*, 21403–21414.

[33] J. A. Spies, E. A. Perets, K. J. Fisher, B. Rudshteyn, V. S. Batista, G. W. Brudvig, C. A. Schmuttenmaer, *Chem. Soc. Rev.* **2019**, *48*, 1865–1873.

[34] T. Duchanois, L. Liu, M. Pastore, A. Monari, C. Cebrián, Y. Trolez, M. Darari, K. Magra, A. Francés-Monerris, E. Domenichini, et al., *Inorganics* **2018**, *6*, 63.

[35] M. Pastore, *Computation* **2017**, *5*, 5.

[36] F. Lucarini, J. Fize, A. Morozan, M. Marazzi, M. Natali, M. Pastore, V. Artero, A. Ruggi, *Sustain. Energy Fuels* **2020**, *4*, 589–599.

[37] S. Piccinin, D. Rocca, M. Pastore, *J. Phys. Chem. C* **2017**, *121*, 22286–22294.

[38] M. Wykes, F. Odobel, C. Adamo, I. Ciofini, F. Labat, *J. Mol. Model.* **2016**, *22*, 289.

[39] A. B. Muñoz-García, M. Pavone, *Phys. Chem. Chem. Phys.* **2015**, *17*, 12238–12246.

[40] J. Massin, S. Lyu, M. Pavone, A. B. Muñoz-García, B. Kauffmann, T. Toupance, M. Chavarot-Kerlidou, V. Artero, C. Olivier, *Dalton Trans.* **2016**, *45*, 12539–12547.

[41] P. Naik, A. Planchat, Y. Pellegrin, F. Odobel, A. Vasudeva Adhikari, *Sol. Energy* **2017**, *157*, 1064–1073.

[42] L. L. Sun, T. Zhang, J. Wang, H. Li, L. K. Yan, Z. M. Su, *RSC Adv.* **2015**, *5*, 39821–39827.

[43] T. Zhang, W. Guan, L. Yan, T. Ma, J. Wang, Z. Su, *Phys. Chem. Chem. Phys.* **2015**, *17*, 5459–5465.

[44] S. Mori, S. Fukuda, S. Sumikura, Y. Takeda, Y. Tamaki, E. Suzuki, T. Abe, *J. Phys. Chem. C* **2008**, *112*, 16134–16139.

[45] J. M. Gardner, M. Beyler, M. Karnahl, S. Tschierlei, S. Ott, L. Hammarström, *J. Am. Chem. Soc.* **2012**, *134*, 19322–19325.

[46] A. Morandeira, G. Boschloo, A. Hagfeldt, L. Hammarström, *J. Phys. Chem. B* **2005**, *109*, 19403–19410.

[47] A. Migani, D. J. Mowbray, J. Zhao, H. Petek, A. Rubio, *J. Chem. Theory Comput.* **2014**, *10*, 2103–2113.

[48] M. Pastore, S. Fantacci, F. De Angelis, *J. Phys. Chem. C* **2013**, *117*, 3685–3700.

[49] Y. Ping, D. Rocca, G. Galli, *Chem. Soc. Rev.* **2013**, *42*, 2437–2469.

[50] G. Onida, L. Reining, A. Rubio, *Rev. Mod. Phys.* **2002**, *74*, 601–659.

[51] P. Umari, L. Giacomazzi, F. De Angelis, M. Pastore, S. Baroni, *J. Chem. Phys.* **2013**, *139*, 014709.

[52] C. Faber, I. Duchemin, T. Deutsch, X. Blase, *Phys. Rev. B* **2012**, *86*, 155315.

[53] D. Jacquemin, I. Duchemin, X. Blase, *J. Chem. Theory Comput.* **2015**, *11*, 3290–3304.

[54] J. B. Neaton, M. S. Hybertsen, S. G. Louie, *Phys. Rev. Lett.* **2006**, *97*, 216405.

[55] J. M. Garcia-Lastra, K. S. Thygesen, *Phys. Rev. Lett.* **2011**, *106*, 187402.

[56] C. Freysoldt, P. Rinke, M. Scheffler, *Phys. Rev. Lett.* **2009**, *103*, 056803.

[57] M. Yu, P. Doak, I. Tamblyn, J. B. Neaton, *J. Phys. Chem. Lett.* **2013**, *4*, 1701–1706.

[58] C. Verdi, E. Mosconi, F. De Angelis, M. Marsili, P. Umari, *Phys. Rev. B* **2014**, *90*, 155410.

[59] C. E. Patrick, F. Giustino, *Phys. Rev. Lett.* **2012**, *109*, 116801.

[60] N. Rinaldi-Montes, P. Gorria, D. Martínez-Blanco, A. B. Fuertes, I. Puente-Orench, L. Olivi, J. A. Blanco, *AIP Adv.* **2016**, *6*, 056104.

[61] M. Cococcioni, S. de Gironcoli, *Phys. Rev. B* **2005**, *71*, 035105.

[62] G. Kresse, J. Furthmüller, *Phys. Rev. B* **1996**, *54*, 11169–11186.

[63] G. Kresse, J. Furthmüller, *Comput. Mater. Sci.* **1996**, *6*, 15–50.

[64] M. Shishkin, G. Kresse, *Phys. Rev. B* **2006**, *74*, 035101.

[65] G. Kresse, D. Joubert, *Phys. Rev. B* **1999**, *59*, 1758–1775.

[66] F. Bruneval, M. A. L. Marques, *J. Chem. Theory Comput.* **2013**, *9*, 324–329.

[67] H. Jiang, R. I. Gomez-Abal, P. Rinke, M. Scheffler, *Phys. Rev. B* **2010**, *82*, 045108.

[68] J. Hutter, M. Iannuzzi, F. Schiffmann, J. VandeVondele, *Wiley Interdiscip. Rev. Comput. Mol. Sci.* **2014**, *4*, 15–25.

[69] G. Bussi, D. Donadio, M. Parrinello, *J. Chem. Phys.* **2007**, *126*, 014101.

[70] S. Hüfner, *Adv. Phys.* **1994**, *43*, 183–356.

[71] R. J. Powell, W. E. Spicer, *Phys. Rev. B* **1970**, *2*, 2182–2193.

[72] T. Dong, H. Suk, H. Hosun, *J. Korean Phys. Soc.* **2007**, *50*, 632.

[73] G. A. Sawatzky, J. W. Allen, *Phys. Rev. Lett.* **1984**, *53*, 2339–2342.

[74] E. Z. Kurmaev, R. G. Wilks, A. Moewes, L. D. Finkelstein, S. N. Shamin, J. Kune š, *Phys. Rev. B* **2008**, *77*, 165127.

[75] O. Bengone, M. Alouani, J. Hugel, P. Blöchl, *Comput. Mater. Sci.* **2002**, *24*, 192–198.

[76] S. Kobayashi, Y. Nohara, S. Yamamoto, T. Fujiwara, *Phys. Rev. B* **2008**, *78*, 155112.

[77] J.-L. Li, G.-M. Rignanese, S. G. Louie, *Phys. Rev. B* **2005**, *71*, 193102.

[78] S. V. Faleev, M. van Schilfgaarde, T. Kotani, *Phys. Rev. Lett.* **2004**, *93*, 126406.

[79] C. Rödl, F. Fuchs, J. Furthmüller, F. Bechstedt, *Phys. Rev. B* **2009**, *79*, 235114.

[80] G. Onida, L. Reining, R. W. Godby, R. Del Sole, W. Andreoni, *Phys. Rev. Lett.* **1995**, *75*, 818–821.

[81] F. Cinquini, L. Giordano, G. Pacchioni, A. M. Ferrari, C. Pisani, C. Roetti, *Phys. Rev. B* **2006**, *74*, 165403.

[82] A. M. Ferrari, C. Pisani, F. Cinquini, L. Giordano, G. Pacchioni, *J. Chem. Phys.* **2007**, *127*, 174711.

[83] H. Momida, T. Oguchi, *J. Phys. Soc. Jpn.* **2003**, *72*, 588–593.

[84] M. D. Irwin, D. B. Buchholz, A. W. Hains, R. P. H. Chang, T. J. Marks, *Proc. Natl. Acad. Sci. USA* **2008**, *105*, 2783–2787.

[85] X. Blase, C. Attaccalite, *Appl. Phys. Lett.* **2011**, *99*, 171909.

[86] J. F. Janak, *Phys. Rev. B* **1978**, *18*, 7165–7168.

[87] J. Szuber, *J. Electron. Spectros. Relat. Phenomena* **1984**, *34*, 337–341.

[88] D. M. Tench, E. Yeager, *J. Electrochem. Soc.* **1973**, *120*, 164.

[89] A. H. Madjid, J. M. Martinez, *Phys. Rev. Lett.* **1972**, *28*, 1313–1315.

[90] Y. Hinuma, A. Grüneis, G. Kresse, F. Oba, *Phys. Rev. B* **2014**, *90*, 155405.

[91] N. M. Correa, N. E. Levinger, *J. Phys. Chem. B* **2006**, *110*, 13050–13061.

[92] G. Mercurio, E. R. McNellis, I. Martin, S. Hagen, F. Leyssner, S. Soubatch, J. Meyer, M. Wolf, P. Tegeder, F. S. Tautz, K. Reuter, *Phys. Rev. Lett.* **2010**, *104*, 036102.

[93] K. Tonigold, A. Groß, *J. Comput. Chem.* **2012**, *33*, 695–701.

[94] A. Dualeh, F. De Angelis, S. Fantacci, T. Moehl, C. Yi, F. Kessler, E. Baranoff, M. K. Nazeeruddin, M. Grätzel, *J. Phys. Chem. C* **2012**, *116*, 1572–1578.

[95] M. Xu, M. Zhang, M. Pastore, R. Li, F. De Angelis, P. Wang, *Chem. Sci.* **2012**, *3*, 976–983.

[96] J. M. Garcia-Lastra, C. Rostgaard, A. Rubio, K. S. Thygesen, *Phys. Rev. B* **2009**, *80*, 245427.

[97] D. Golze, M. Dvorak, P. Rinke, *Front. Chem.* **2019**, *7*, 377.

[98] C. Di Valentin, S. Botti, M. Cococcioni, Eds., First Principles Approaches to Spectroscopic Properties of Complex Materials, Springer, **2014**.

[99] F. De Angelis, S. Fantacci, R. Gebauer, *J. Phys. Chem. Lett.* **2011**, *2*, 813–817.

[100] F. Bella, C. Gerbaldi, C. Barolo, M. Grätzel, *Chem. Soc. Rev.* **2015**, *44*, 3431–3473.

[101] W. Zhao, M. Bajdich, S. Carey, A. Vojvodic, J. K. Nørskov, C. T. Campbell, *ACS Catal.* **2016**, *6*, 7377–7384.

[102] K. Refson, R. A. Wogelius, D. G. Fraser, M. C. Payne, M. H. Lee, V. Milman, *Phys. Rev. B* **1995**, *52*, 10823–10826.

[103] S. Hosseinpour, F. Tang, F. Wang, R. A. Livingstone, S. J. Schlegel, T. Ohto, M. Bonn, Y. Nagata, E. H. G. Backus, *J. Phys. Chem. Lett.* **2017**, *8*, 2195–2199.

[104] S. Galliano, F. Bella, C. Gerbaldi, M. Falco, G. Viscardi, M. Grätzel, C. Barolo, *Energy Technol.* **2017**, *5*, 300–311.

Chapter 4
Optical and fundamental gap of WO_3 bulk systems

Tungsten trioxide (WO_3) is an Earth abundant material that has been largely studied due to its attractive properties for many technological applications. WO_3 is electrochromic[1] and photochromic,[2] which means that its optical properties change under application of electric potential and light, respectively. These properties make WO_3 suitable for application in energy-efficient windows, displays and photonic crystals.[3] Also, it shows stability against photocorrosion[4] in both basic and acidic solutions, high photosensitivity and notable electron transport properties.[5] For these reasons, WO_3 is a promising material for photovoltaic and Photoelectrochemical Cells (e.g. water splitting devices) where it could be employed as n-type SC in place of the well-known Titania (TiO_2).[6] Indeed, WO_3 has an optical gap of about 2.6 eV, lower than the one of TiO_2 (ca. 3.2 eV), thus allowing a moderate absorption of visible light.[7] However, the WO_3 band gap remains too large for efficient solar energy absorption and many investigations aimed at lowering its gap have been reported. In particular, the optical gap was shown to be very sensitive to the distortion of the crystal structure, promoted by the intercalation of dopant species or by structural modifications.[8] In general, the crystal lattice distortions should be regarded as detrimental, as they enlarge the band gap respect to the one predicted for the highly symmetric phases of WO_3.[7–9] However, the latters, as we will discuss in the following, are unstable at standard conditions. Hence, a deep comprehension of the effects of crystal lattice distortions on the optoelectronic properties of WO_3 could give clear guidelines to perform targeted distortion aimed at producing stable and optimised WO_3 systems.[10–14]

WO_3 has a very rich phase diagram, which shows six different polymorphs, upon temperature and pressure variation, showing different band gaps and different electronic structures.[6] The simplest phase of WO_3 is the cubic one, which is characterized by regular corner-sharing WO_6 octahedrons like the cubic structure of ReO_3.[6, 15] This phase is, as stated, extremely unstable and take place only in critical condition (0.66 GPa and 700°C).[15] As the temperature decreases and under standard pressure conditions, below the melting point of WO_3 (1700 K), there are five different phases that occur in the following order:[6, 9] tetragonal (α-WO_3, $T > 740$°C) $\rightarrow$ orthorombic (β-WO_3, 740°C to 330°C) $\rightarrow$ room-temperature monoclinic (γ-WO_3, 330°C to 17°C) $\rightarrow$ triclinic (δ-WO_3, 17°C to -43°C) $\rightarrow$ low-temperature monoclinic (δ-WO_3, $T < -43$°C). Respect to the "ideal"

cubic structure, these phases consist of distorted corner-sharing WO_6 octhaedra, which becomes more distorted from the tetragonal to the low-temperature monoclinic.[6, 9] The distortions that occur during cooling are assumed to be the main factor delivering the gap opening as has been discussed in some theoretical and computational studies.[8, 9] Pacchioni and co-workers,[9] reported the first systematic first principle investigation on all the WO_3 bulk phases in which they showed that the highly symmetric phases of WO_3 (cubic, tetragonal) have smaller gaps compared to the more distorted ones. This investigation was carried out by means of DFT calculations using standard functionals (LDA and GGA) and several hybrid functionals (e.g. B3LYP, HSE06 and PBE0). Among these two functional categories small differences were found on the band structures shapes and on the lattice parameters, while B3LYP was shown to better reproduce the experimental band gaps. On the other hand, GW and BSE calculations reported so far delivered an overall better agreement with the available experimental photoemission gaps and optical gaps with respect to those estimated from DFT-based calculations.[7, 8, 16, 17] In line with these studies, in this chapter we report, as the first step of an ambitious project aiming at analytically calculate the radiative lifetime, ab initio calculations at the MBPT level of the fundamental gap, the band structure and the optical properties of WO_3 considering its simple cubic phase and the two most stable phases, namely the room-temperature monoclinic and the triclinic phases. In particular, the band structure and the fundamental band gap have been computed at G_0W_0 level, while the optical spectra and the exciton band structure have been computed at the BSE level. For the monoclinic system, we also address the calculation of the excitonic effective masses for the first two bright excitons. The latter, have been calculated through a curve fitting of the excitonic bands that have been constructed by exploring a wide range of momentum transfer q point via q-finite BSE calculations. The final goal of our work, as stated above, is to compute the exciton lifetimes of these WO_3 phases, through an analytical model, which is currently in development in collaboration with the group of Yuan Ping of the University of Santa Cruz. This model will be able to predict the exciton lifetime, considering the radiative decay as the only possible route for the electron-hole recombination, on the basis of the excitation energy, the oscillator strength and the exciton effective mass. Similar models have been reported and have been

recently applied to the study of the wurtzite GaN.[18] However, these models cannot be applied to 3D systems having non-orthogonal axes, such as the monoclinic and the triclinic phases. As stated above, this project is currently ongoing and we present here our preliminary results.

4.1 Computational Details

WO_3 has been studied here considering the room temperature monoclinic, the triclinic and the simple cubic phases. All the calculations reported in this chapter have been carried out making use of the VASP[19, 20], and thus by using plane wave basis set and LDA PAW pseudopotentials[21]. In particular, the 2s and the 2p shells are treated as valence for Oxygens and the 5p 6s 5d for Tungsten atoms. For the DFT calculations, we considered an energy cutoff of 700 eV for the cubic phase and 600 eV for both γ monoclinic and triclinic phases. For the simple cubic WO_3, we sampled the Brilloin zone with different number of K points. Namely, starting from the $6\times6\times6$ K points grid centered in Γ, we increased the number of K points by $2\times2\times2$ until reaching convergence of the fundamental gap, obtained by considering the $12\times12\times12$ K points mesh. The calculations on both the monoclinic and the triclinic phases, have been carried out by sampling the Brilloin zone with $6\times6\times6$ K points, which define a K points density in the reciprocal space similar to the one obtained with $12\times12\times12$ K points for the cubic case. All the phases of WO_3 have been modeled considering the experimental lattice parameters, and by relaxing the atomic positions at LDA level. For the cubic system we consider a lattice constant equal to 3.78 Å.[15] For the monoclinic system we consider the following lattice parameters: a = 7.30 Å b = 7.53Å c = 7.68Å and β=90.9°;[22] and for the triclinic system the following parameters: a = 7.31Å, b=7.52 Å c = 7.68 Å, α =88.81°, β = 90.92° and γ = 90.93°.[23]

GW calculations have been performed making use of the G_0W_0 approximation, and adopting a kinetic energy cutoff for the response function $\chi^0_q(G,G',\omega)$[24] of 250 eV for the cubic system and 200 eV for both the γ monoclinic and the triclinic systems. Then, we considered 320 bands (i.e. 304 empty bands) for the cubic system and 220 bands (i.e. 92 empty bands) for both the monoclinic and the

triclinic phases for the summation over bands in the calculation of the polarizability and the self-energy.

The BSE, the q-finite BSE, and the Random phase Approximation (RPA) calculations, have been carried out by adopting the same parameters used for GW calculations and considering the 8 highest Valence Bands (VB) and 8 lowest Conduction Bands (CB) for all the considered WO_3 phases.

4.2 Fundamental band gap and band structure

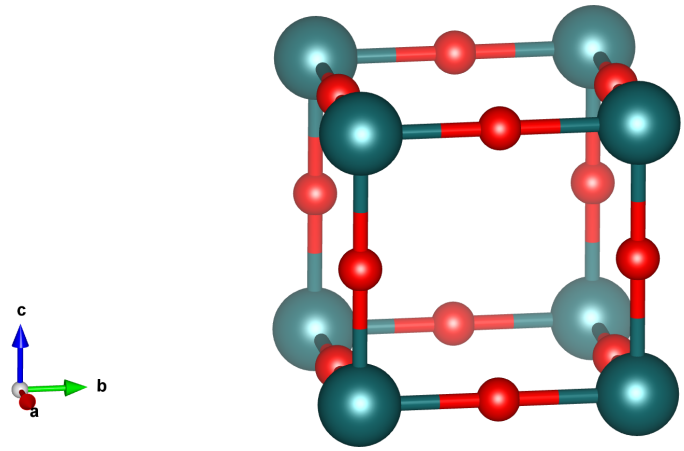

Figure 4.1: The crystal structure of the cubic system of WO_3 relaxed at LDA level.

The cubic phase of WO_3, which is shown in Figure 4.1, is characterized by a corner-sharing octahedron structure where each W (grey-blue) atoms are located in the center of the regular octahedron and the oxygen (red) atoms are positioned on its vertex (Figure 4.1). Cubic WO_3 is stable at ambient condition in combination with intercalated species, namely alkali metals, alkali hearth metals or hydrogen atoms, even if these impurities promote large distortions on the cubic structure and affect its electronic and optical properties.[11–14] Impurities-free cubic WO_3 was only recently reported at ambient condition in the form of powder consisting of crystals of few tenth of nanometres.[15] As a matter of fact, there

are no experimental measures of the band gap or optical gap for the cubic phase of WO_3. However, it is the smallest and the highly symmetric crystal phase of WO_3 and it can be used to test the convergency of the calculations (respect to the K points numbers), as well as a reference to unravel the role of the geometrical distortions on the electronic properties of WO_3.

Method	Direct	Indirect
	$6 \times 6 \times 6$	
LDA	1.598 [Γ]	0.535 [R→ Γ]
G_0W_0@LDA	2.513 [Γ]	1.370 [R→ Γ]
	$8 \times 8 \times 8$	
LDA	1.605 [Γ]	0.543 [R→ Γ]
G_0W_0@LDA	2.536 [Γ]	1.396 [R→ Γ]
	$10 \times 10 \times 10$	
LDA	1.607 [Γ]	0.544 [R→ Γ]
G_0W_0@LDA	2.534 [Γ]	1.395 [R→ Γ]
	$12 \times 12 \times 12$	
LDA	1.607 [Γ]	0.545 [R→ Γ]
G_0W_0@LDA	2.535 [Γ]	1.396 [R→ Γ]
Other theoretical work		
G_0W_0@LDA[8][a]	1.78	
G_0W_0@LDA[8][b]	1.65	

[a] the band gap was computed at the experimental geometry.

[b] the band gap was computed at the optimized geometry relaxing both the ionic positions and the cell parameters.

Table 4.1: Direct and indirect band gap for the cubic phase of WO_3 computed from the LDA and the G_0W_0@LDA calculations considering different samples of the Brilloin zone and compared with G_0W_0@LDA results of ref [8]. The K points involved in the band gaps are reported into squared brackets

The computed LDA and G_0W_0@LDA direct and indirect band gaps for different K points mesh are gathered in Table 4.1, along with G_0W_0@LDA results from ref [8]. In agreement with previous results, we found that the gap for cubic WO_3 is indirect, although the discrepancy (ca. 0.2 eV) between our GW result and the one reported by Galli and coworkers is probably due to their use of relaxed lattice parameters, while in our approach, as stated in Section 4.1, we relaxed the atomic positions only.

From our data reported in Table 4.1, it is evident that the increase of K points delivers only negligible differences in both the direct and the indirect band gap, which are reasonably converged with the $12 \times 12 \times 12$ K points grid. Moreover, in both LDA and G_0W_0@LDA calculations, the same K points are involved in both the direct and indirect band gaps, as also evidenced by the computed LDA and G_0W_0@LDA band structures shown in Figure 4.2. GW corrections, as reported for other WO_3 phases[17] indeed affect only marginally the shape of the electronic band structure. On the other hand, they entail an opening of the band gap of 0.93 eV and 0.85 eV for the direct and the indirect gap, respectively.

Both band structures show different dispersion around the VBM and the CBM

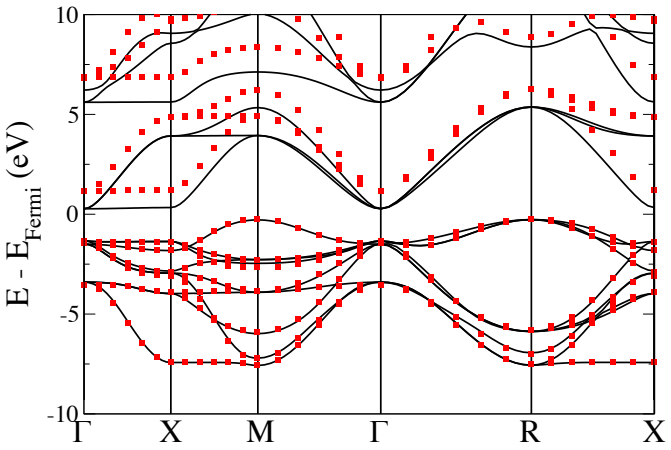

Figure 4.2: Band structure for the cubic phase of WO_3 computed at LDA (black lines) and G_0W_0@LDA (red circles) levels of theory. To have a better visual comparison, the absolute energies of the GW bands have been shifted in such a way to make the GW VBM coincident with the LDA one. The Fermi level, computed at LDA level, is set to 0 eV.

suggesting different effective masses for holes and for electrons. If, on one hand, the VB shows dispersion along the R-Γ and the R-X directions, on the other hand, the CB shows dispersion along the Γ-R and the Γ-M directions and is rather flat along the Γ-X direction, hence suggesting a difficult conduction along this direction.

We now turn to the discussion of the monoclinic phase, i.e., the most stable phase of WO_3.[6] Its unit cell is only slightly distorted compared to the orthorombic

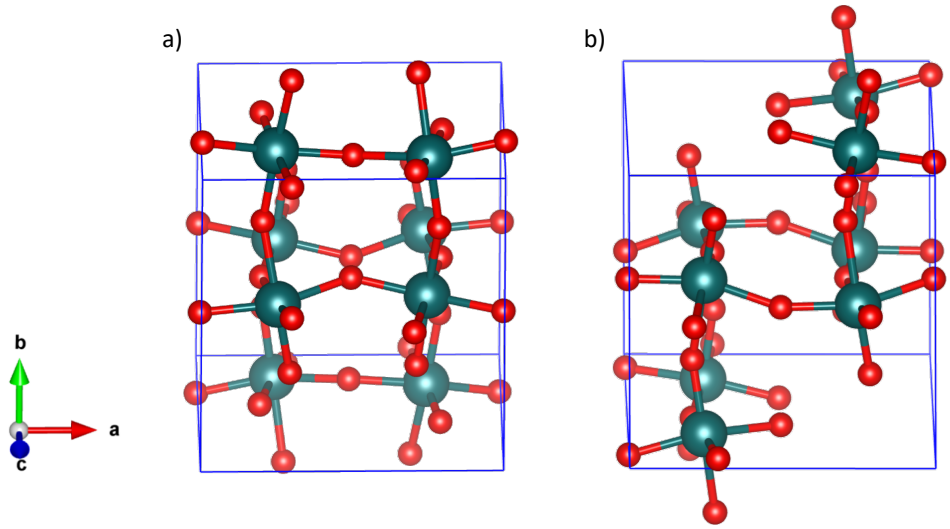

Figure 4.3: LDA relaxed crystal structure of the γ monoclinic phase (left) and the triclinic phase (right) of WO_3

phase, being the β angle not much different from the right angle (90.9°). It contains eight distorted corner sharing WO_6 octahedra (8 W and 24 O atoms) having off-centered W atoms promoting a short-long W-O bond distances alternation along both a,b and c directions. Also, these octahedra are tilted respect all the three main axes.

The electronic properties of the monoclinic system are quite different from the ones of the cubic system.[7, 9] As recently discussed by Galli and Ping, the distortion of the WO_6 octahedra, in particular the variation of the W-O-W angles, which becomes more pronounced going from the cubic phase to the low-temperature monoclinic phase, promotes a gap opening and relevant differences on the band structure.[8]

Table 4.2 reports the band gaps computed from both the LDA and the G_0W_0@LDA calculations, and at both level of theory the gap is larger that the one computed for the cubic phase. The gap predicted from the G_0W_0@LDA calculation is in line with the experimental fundamental gap measured through Ultravi-

Method	Direct	Indirect
MONOCLINIC		
LDA	1.94 [Γ]	1.93 [0.33, 0, 0 → Γ]
G_0W_0@LDA	3.54 [0,0,0.1667]	
Other theoretical work		
G_0W_0@PBE[16][a]	3.38	
G_0W_0@LDA[8][a]	3.30	
G_0W_0@LDA[8][b]	2.59	
Experiment		
EXP (UPS-IPES)	3.38 ± 0.2[25], 3.28 ± 0.14[26]	
TRICLINIC		
LDA	1.65 [Γ]	
G_0W_0@LDA	3.36 [Γ]	
Other theoretical work		
G_0W_0@LDA[8][a]	3.38	
G_0W_0@LDA[8][b]	2.86	

[a] the band gaps were computed at the experimental geometry.

[b] the band gap was computed at the optimized geometry relaxing both the ionic positions and the cell parameters.

Table 4.2: Band gap for the γ monoclinic and the triclinic phases of WO_3 computed from the LDA and the G_0W_0@LDA calculations compared with other theoretical studies. For the monoclinic phase, the fundamental experimental gap and the indirect gap calculated at the LDA level are also reported. The K points involved in the band gaps are reported into squared brackets

olet Photoemission Spectroscopy (UPS) and inverse Photoemission Spectroscopy (IPES). However, as recently discussed by Galli and co-workers, to have a better comparison with the experimental data, one should consider Spin-Orbit (SO) coupling and electron-phonon (e-ph) coupling that, in the γ monoclinic phase produce a decrease in the gap of about 0.3 eV.[7] Although we have not considered these effects in this thesis, progress along these lines are currently ongoing.

Regarding the comparison with other computational studies, a reasonable agreement with the band gap calculated from Gerosa et. al.[16] was found, while larger differences, as in the cubic case, were obtained with respect to the value reported by Galli and co-workers.[7] Similar considerations on the difference in the crystal structure also apply in this case. However, as far as the γ monoclinic phase is concerned, we found a better agreement with the computed gaps at the experi-

mental crystal lattice compared to the one computed at the optimized one. This is probably due to the large difference between the experimental structure and the relaxed one for the γ monoclinic phase.

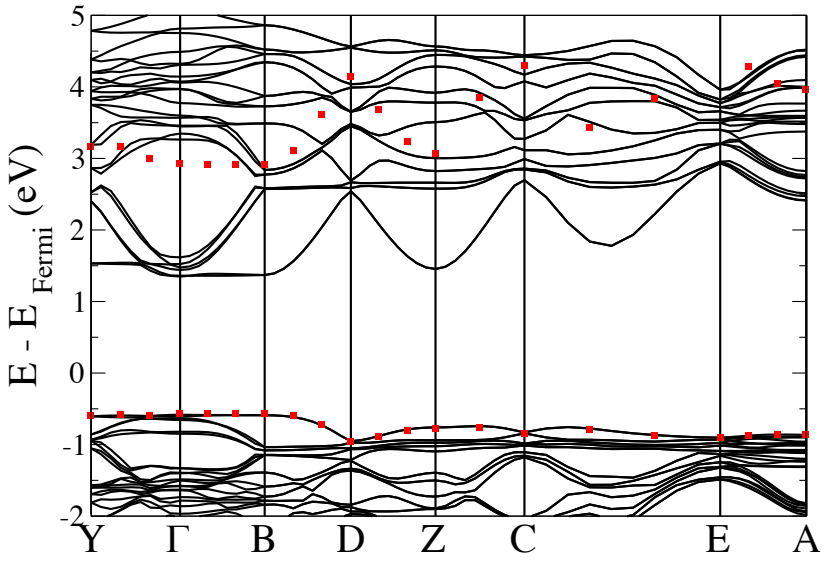

Figure 4.4: Band structure for the γ monoclinic phase of WO_3 computed at LDA (black lines) and G_0W_0@LDA (red circles) levels of theory. Since the GW bands are sizeable shifted, only the VB and CB have been plotted to make the visualization clear. Also, to have a better visual comparison, the absolute energies of the GW bands have been shifted in such a way to make the GW VBM coincident with the LDA one. The Fermi level, computed at LDA level, is set to 0 eV.

LDA predicts an indirect band gap, whereas the gap is direct at G_0W_0@LDA level. Moreover, the K points involved in these gaps are different in the two approaches, though, in both cases, they are located close to Γ. It is worth highlighting that, although the LDA gap is indirect, the difference between the latter and the direct one is very small (ca. 0.006 eV). As a matter of fact, the nature of the γ monoclinic WO_3 gap is still a controversial issue. Several experimental investigations claimed that the optical gap is indirect (2.6 eV)[27, 28] while Salje et al. reported a direct gap (2.58 eV).[29] The nature of the gap is a controversial issue also in the theoretical and computational investigations. The DFT studies reported so far show that most of functionals predict a direct gap, while the revised Perdew-Becke-Ernzerhof exchange and correlation functional (r-PBE) and

the LDA functionals, as we also show, deliver an indirect gap.[9] On the other hand, a direct gap is reported in all the GW works.[7, 8, 17] Anyway, all these studies found a very small difference between the direct and the indirect band gap and usually a gap having this characteristic is referred to as pseudo-direct. The pseudo-direct nature of the gap of the room temperature monoclinic WO_3 is evident in the band structure shown in Figure 4.4, in which both the VB and the CB around the Γ point, i.e. close to the VBM and CBM, show scarce dispersion, and this also implies poor conduction for holes and electrons along the Γ-Y and the Γ-B directions. GW corrections, as stated above, provide small changes in the shape of the band structure. In fact, as is apparent, although a sizeable gap opening (ca. 1.60 eV) and a change of the K points involved in the gap are attained, the overall shape of the band structure is preserved. However, in order to better compare the LDA and the GW bands, the latters should be calculated by sampling the Brilloin zone with an higher number of k-points that is, however, unaffordable for such a big system.

Next, we discuss the triclinic phase of WO_3. This phase does not differ significantly from the monoclinic phase, as it can be seen in Figure 4.3. In fact, both α and γ angles do not differ much from the right angle (See Section 4.1). Similarly, it is formed by tilted WO_6 octhaedra having off-centered W atoms and showing bond length alternation along all the three principal axis. Although the triclinic phase is the second most stable phase of WO_3 and it has been well experimentally characterized,[30] as far as we know, there are no reported experimental data on both fundamental and optical gap. On the other hand, previous computational works, based on GW calculations, addressed the study of the triclinic phase of WO_3.[8, 17] Contrary to the ambiguity of the band gap of the γ monoclinic WO_3 phase, the band gap of δ-WO_3 is generally calculated as direct.[8, 9, 17] As shown in Table 4.2, we obtained from both LDA and G_0W_0@LDA calculations a direct band gap located at Γ. In particular, GW corrections promote a large gap opening (ca. 1.7 eV) similar to the one found for the monoclinic system. Furthermore, for the same reasons discussed above for the monoclinic phase, we found a better agreement with the calculated fundamental gap at the experimental geometry reported from ref. [8] compared to the one calculated at the optimized one.

In Figure 4.5 we report the calculated band structure for the triclinic phase. As

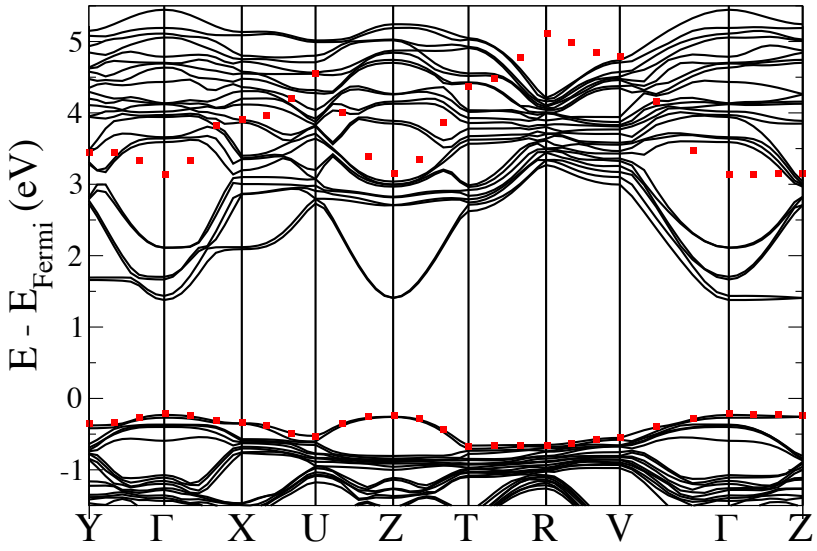

Figure 4.5: Band structure for the triclinic phase of WO_3 computed at LDA (black lines) and G_0W_0@LDA (red circles) levels of theory. Since the GW bands are sizeable shifted, only the VB and CB have been plotted to make the visualization clear. Also, to have a better visual comparison, the absolute energies of the GW bands have been shifted in such a way to make the GW VBM coincident with the LDA one. The Fermi level, computed at LDA level, is set to 0 eV.

discussed for both the cubic and the monoclinic phases, the band edges appear rather flat around the Γ point, especially along the Γ-Z direction and, again, its shape is not very sensitive to GW corrections.

To conclude, the calculated band gap, for the considered WO_3 phases, follows the order: cubic < triclinic < monoclinic at both LDA and GW level of calculation. Moreover, the common aspect of all the studied WO_3 phases is that their band structures show scarce dispersion, close to both the VBM and the CBM, along certain directions of the k-space, suggesting high effective masses for both hole and electron. This will be discussed further in Section 4.4, where we will address the calculation of the exciton effective masses for the monoclinic system.

4.3 Optical gap and optical spectra

The optical gap and the optical spectra of WO_3, as in the case of the fundamental gap, have been experimentally investigated only for the γ monoclinic phase. Nonetheless, we computed the optical spectra and the optical gap for all the considered phases in order to describe the role of lattice distortions on the optical properties. In Figure 4.6 we report the optical spectra for the three phases computed at BSE level considering the qp energies obtained at GW level. Moreover, to understand the influence of the electron-hole correlation, the BSE spectra are compared with those computed considering the RPA, again, with the corrected GW energies. RPA neglects excitonic effects, namely it does not consider the exchange terms related to screened coulombic term (W). As expected and shown in Figures 4.6, the lack of electron-hole correlation is reflected in a blueshift of the calculated RPA spectra with respect to the BSE ones.[7] Furthermore, a rather marked change in the oscillator strengths of the excitations is also evident, with the BSE peaks appearing less broadened.

To further analyse the difference between RPA and BSE, in Figure 4.7-4.9 we report the fatbands representation[31] of the first eigenvector extracted from both BSE and RPA with non-zero oscillator strength and similar nature in terms of K points and occupied and unoccupied bands involved. Here the red dots correspond to GW energies and blue circles, whose radii is proportional to the weight of the particular electron-hole pair in the eigenvector, are located on the k points and on the bands that are involved in the optical excitation. For all the systems considered, the lowest bright transition involves most of the highest occupied bands and the lowest unoccupied bands at Γ point. Moreover, the BSE fatbands show high delocalization along the directions where the band structure is rather flat, namely the Γ-X direction for the cubic system, the Y-Γ-X branch for the γ monoclinic system and both the Y-Γ-X branch and the Γ-Z direction for the triclinic system. The extent of these delocalizations correspond to the dimension of the excitons. Hence, this analysis tell us that excitons, for all the three systems, are delocalized in the reciprocal k-space along all the directions around Γ where the band structure is rather flat. This representation, beside being useful to describe the nature and the dimension of excitons highlight also another important difference between the

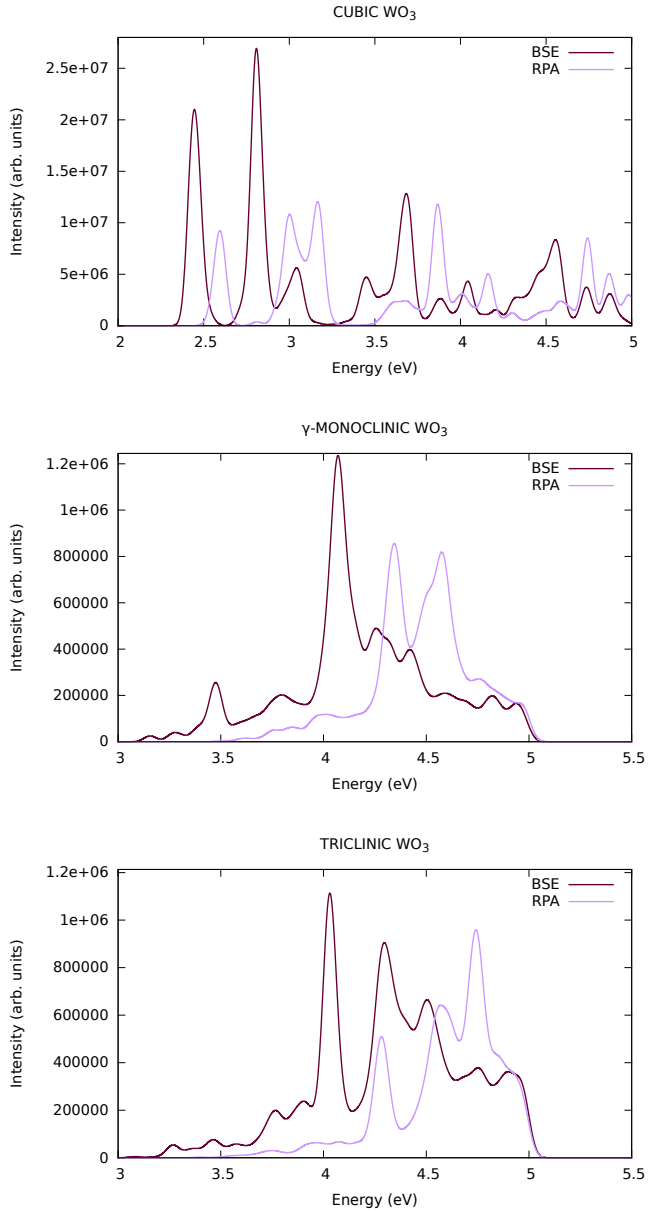

Figure 4.6: Absorption spectra of the cubic (top panel), monoclinic (middle panel) and triclinic phases of WO_3 computed by solving the Bethe-Salpeter equation (BSE) and by adopting the RPA. In both cases the GW corrected energies have been used. The spectra were reproduced through a convolution with Gaussian functions having an fwhm of 0.03 eV.

RPA and the BSE methods. In fact, RPA fatbands are less delocalized, again, as a consequence of the absence of the aforementioned exchange terms. In Table 4.3 we

report, for the three phases, the BSE and RPA excitation energies corresponding to the first bright transition (optical gap) and the exciton binding energy, obtained from the difference between the RPA and the BSE eigenvalues. The computed BSE/RPA excitations follow the same trend of the fundamental gap, i.e. cubic (2.41 eV)<triclinic (3.08 eV)<monoclinic (3.17 eV). The same trend apply for the exciton binding energies being 0.12 eV (cubic), 0.31 eV (triclinic) and 0.34 eV (monoclinic). As a consequence, the electron-hole coupling terms are larger in WO_3 distorted crystal lattices compared to the highly symmetric cubic one. In Table 4.3, it is also reported the experimental optical gap for the γ monoclinic system that, however, is lower in energy of ca. 0.5 eV with respect to the BSE one. Moreover, the experimental exciton binding energy of the monoclinic phase, calculated as the difference between the photoemission gap and the optical gap (Table 4.2), is of the order of 0.5 eV that is, however, higher in energy compared with our findings (0.36 eV). These discrepancies are probably associated with the fact that we did not consider correlation effects that arise from SO coupling and e-ph coupling and, as discussed for the fundamental gap, we are currently working to include such corrections in the description of the optical spectra.

	BSE	RPA	E_B	E_g (EXP)
Cubic	2.41	2.53	0.12	
γ Monoclinic	3.17	3.50	0.34	2.6 $\pm$ 0.1[29, 32]
Triclinic	3.08	3.39	0.31	

Table 4.3: Calculated optical band gap (eV) for both the γ monoclinic, the triclinic and the cubic phases of WO_3 at BSE level and considering the RPA. The experimental optical gap of the γ monoclinic system is also reported.

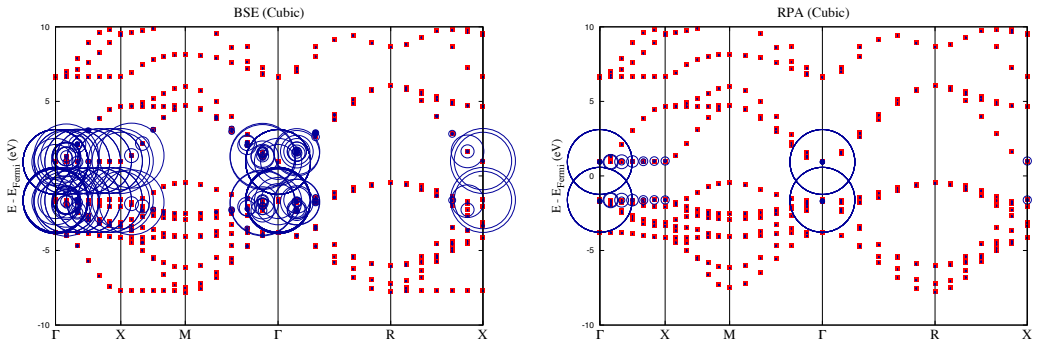

Figure 4.7: GW band structure for the cubic phase of WO_3 considering the eight uppermost occupied bands and the eight bottommost unoccupied bands (red dots). The blue circles represent the contribution of the electron-hole pair at a give k-points and for a given occupied band-unoccupied band pair to the first bright excitation computed at BSE level (left) and at RPA level (right). The Fermi level is set to 0 eV.

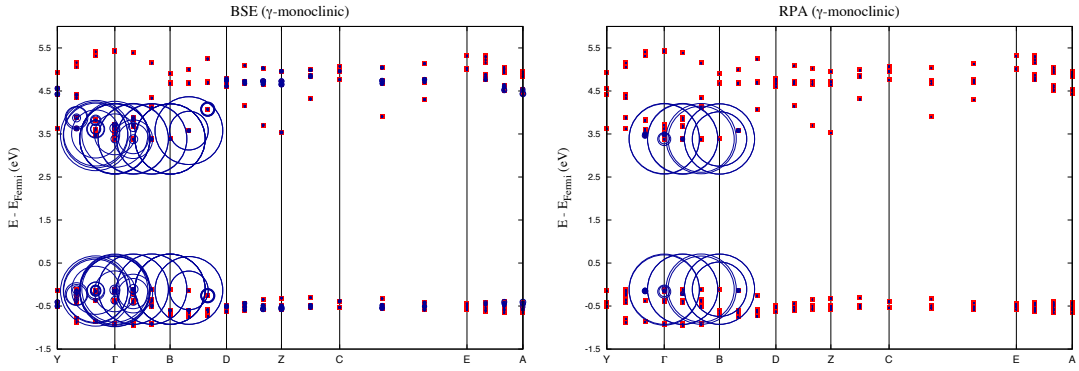

Figure 4.8: GW band structure for the room temperature monoclinic phase of WO_3 considering the eight uppermost occupied bands and the eight bottommost unoccupied bands (red dots). The blue circles represent the contribution of the electron-hole pair at a give k-points and for a given occupied band-unoccupied band pair to the first bright excitation computed at BSE level (left) and at RPA level (right).

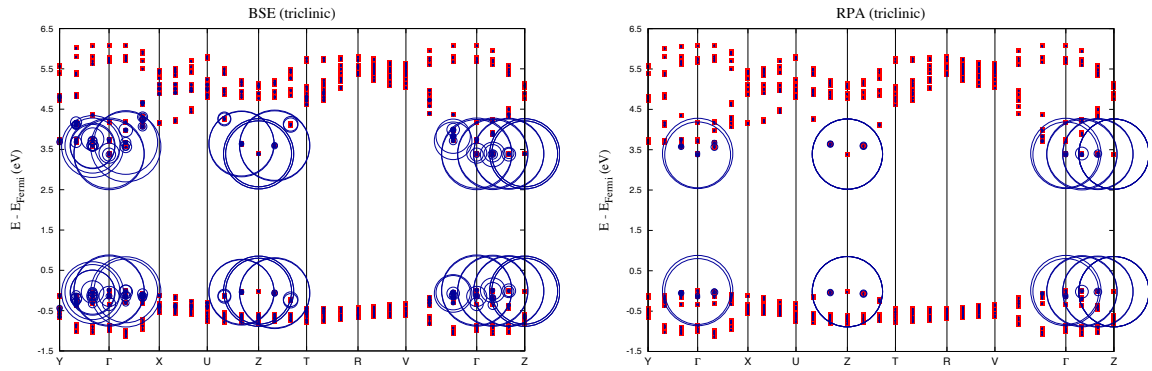

Figure 4.9: GW band structure for the triclinic phase of WO_3 considering the eight uppermost occupied bands and the eight bottommost unoccupied bands (red dots). The blue circles represent the contribution of the electron-hole pair at a give k-points and for a given occupied band-unoccupied band pair to the first bright excitation computed at BSE level (left) and at RPA level (right).

4.4 Exciton effective mass

The exciton effective mass is usually calculated considering the sum of the effective electron and hole masses. The easiest practical way to calculate these effective masses is by means of a parabolic fitting of the VB and the CB, in a narrow range around the VBM and the CBM, to then evaluate the second derivative of such functions. The effective masses for the electron/hole can be indeed calculated by applying the following formula:

$$\frac{1}{m^*_{ij}} = \frac{1}{\hbar^2}\frac{\partial^2 E}{\partial k_i \partial k_j} \tag{4.1}$$

to the second derivative of the function that fits the CB/VB. In equation 4.1, the m^*_{ij} term is the effective mass for the ijth component of the effective mass tensor.

This approach, however, is valid only if the exciton has a Wannier-Mott charachter,[33] namely if it is described in a weakly coupled electron-hole pair regime due to an high electron–hole separation (the exciton radius is of the order of the lattice spacing).[34] In this case, the electron and the hole are bound by Coulombic interactions, largely screened within the crystal lattice, and display a freeparticle-like behaviour.[34–36] In the opposite limit, when the electron and the hole are very close, e.g in molecular crystals characterized of small dielectric constant, they give rise to a tight bound state known as Frenkel exciton, which has a strongly localized character.[33, 36] The Frenkel exciton is characterized by an huge effective mass, which is therefore much greater than the sum of the effective masses of electrons and holes as is the case of Wannier-like excitons.[33] Obviously, between these two opposing models, an infinite range of intermediate cases can occur.

A more refined approach to calculate the effective mass of excitons consists in the calculation of the elements of the effective mass tensor by using the second derivative of exciton bands. These bands can be constructed through q-finite BSE calculations and this approach has been recently applied for the calculation of exciton masses in 2D systems.[35] Following this methodology, we analyzed the exciton dispersion for the γ-WO_3 system. In particular, we evaluated the

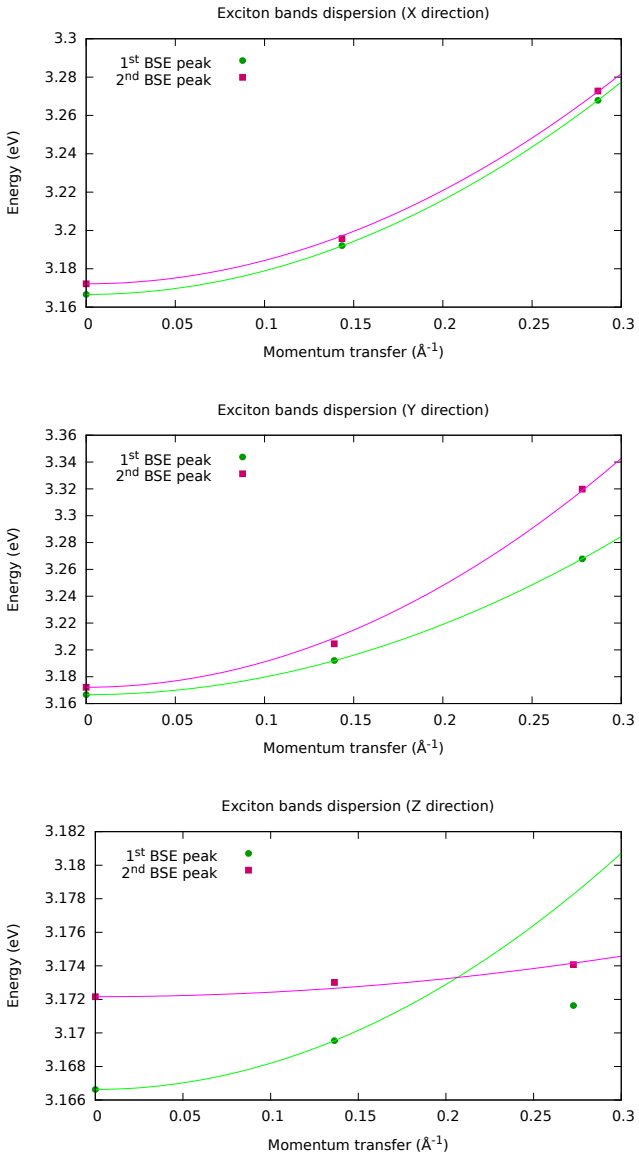

Figure 4.10: Calculated dispersion of the first two bright excitons in γ-WO_3 along X (top panel), Y (central panel) and Z (bottom panel) directions.

exciton band dispersion along the X,Y and Z directions of the reciprocal space, corresponding to the Γ-A, Γ-Z and Γ-B directions, respectively.

At finite temperature, excitons satisfy Bose-Einstein statistics.[37, 38] Thus, as the first two bright excitons are very close in energy (ca. 0.01 eV energy difference

at BSE level) these will have a finite occupation at room temperature.[18, 39, 40] In Figure 4.10 it is reported the exciton band dispersion for the first two bright excitons. For both excitons and for all the considered directions, the dispersion of exciton bands show a parabolic behaviour in a narrow range around Γ, therefore, their curvature can be fitted by a parabolic function. This fitting has been carried out by considering three q points in the range 0-0.3 $Å^{-1}$, except for the first bright exciton along the Z direction, where we considered only two points, since the parabolic behaviour of the exciton band seems to vanish beyond 0.15 $Å^{-1}$. From these functions we calculated the diagonal elements of the effective mass tensor by applying equation 4.1 and the results are displayed in Table 4.4. As expected from the band structure, the ZZ elements of the effective mass tensor are huge for both the bright excitons. On the other hand, the XX and YY elements, which are almost degenerate for the first exciton and differ for about 1 m_0 for the second exciton, are smaller suggesting an higher curvature, for both the VB and the CB, of the band structure along the Γ-A and the Γ-Z directions compared to the Γ-B direction shown in Figure 4.4.

In any case, we found very large exciton effective masses, compared to other Semiconductors,[41] suggesting a limited diffusion for excitons in the γ-WO_3 system. In addition, the anisotropic character of the effective mass tensor suggests an anisotropic behaviour for exciton diffusion. The space-dependent nature of the exciton effective masses should be accounted for when we deal with the calculation of exciton lifetimes. In fact, being the exciton lifetime proportional to the exciton effective mass it will demonstrate different radiative decay in correspondence of different considered directions of the reciprocal space.[18]

In this section, we have discussed an alternative approach for the calculation of exciton effective masses in 3D systems that we plan to validate through experimental measures. In particular, the exciton band structure is experimentally accessible by momentum-resolved Electron Energy Loss Spectroscopy (EELS),[42] hence, a good comparison of our exciton band dispersion will in turn validate our calculated exciton effective masses. However, to obtain a good comparison with experiments we should analyze the dispersion of the exciton bands for a larger number of q points and considering all the possible direction of the k-space. This will allow us to obtain, via curve fitting, a 4-dimensional representation of the

exciton band that, we think, will show a paraboloid-like behaviour in a narrow range around Γ.

	XX	YY	ZZ
1^{st} BSE peak	3.10	2.91	24.35
2^{nd} BSE peak	3.13	2.01	148.82

Table 4.4: Calculated XX, YY and ZZ elements of the effective mass tensor in m_0 units (rest mass of the electron) for both the first two bright excitons.

4.5 Final Remarks

In this chapter we have discussed the description of electronic and optical properties of the room-temperature monoclinic, the triclinic and the cubic phases of WO_3 at MBPT level of theory. In agreement with previous studies, we have shown that the gap opening is promoted by crystal lattice distortions. Moreover, the band structure for all the considered WO_3 phases show poor dispersion along certain directions of the k-space close to both the CBM and the VBM.

Similarly to the fundamental gap, also the optical gap of these phases was shown to be very sensitive to the crystal lattice distortion, showing higher optical excitation energies in monoclinic and triclinic phases compared to the undistorted cubic phase. A similar trend was found for the exciton binding energies that have been calculated considering the difference between the RPA and BSE excitation energies of the lowest bright transition. Furthermore, from the BSE and the RPA eigenvectors corresponding to the first bright exciton we also computed the fatbands. The comparison between the RPA and BSE fatbands disclosed that the lack of exchange terms in the RPA approach entails a less delocalized fatband compared to the BSE one.

Finally, we calculated the exciton effective masses for the first two bright excitons of the monoclinic system. Our calculations have evidenced an anisotropic character of the effective mass tensor which hinders the diffusion of the exciton along Γ-B direction.

Bibliography

[1] S.-H. Lee, R. Deshpande, P. Parilla, K. Jones, B. To, A. Mahan, A. Dillon, *Adv. Mater.* **2006**, *18*, 763–766.

[2] Y. Zhao, Z. C. Feng, Y. Liang, H. W. Sheng, *Appl. Phys. Lett.* **1997**, *71*, 2227–2229.

[3] C. Granqvist, *Sol. Energy Mater. Sol. Cells* **2000**, *60*, 201–262.

[4] S. K. Deb, *Sol. Energy Mater. Sol. Cells* **2008**, *92*, 245–258.

[5] J. M. Berak, M. Sienko, *J. Solid State Chem.* **1970**, *2*, 109–133.

[6] H. Zheng, J. Z. Ou, M. S. Strano, R. B. Kaner, A. Mitchell, K. Kalantar-zadeh, *Adv. Funct. Mater.* **2011**, *21*, 2175–2196.

[7] Y. Ping, D. Rocca, G. Galli, *Phys. Rev. B* **2013**, *87*, 165203.

[8] Y. Ping, G. Galli, *J. Phys. Chem. C* **2014**, *118*, 6019–6028.

[9] F. Wang, C. Di Valentin, G. Pacchioni, *J. Phys. Chem. C* **2011**, *115*, 8345–8353.

[10] Q. Mi, Y. Ping, Y. Li, B. Cao, B. S. Brunschwig, P. G. Khalifah, G. A. Galli, H. B. Gray, N. S. Lewis, *J. Am. Chem. Soc.* **2012**, *134*, 18318–18324.

[11] A. Hjelm, C. G. Granqvist, J. M. Wills, *Phys. Rev. B* **1996**, *54*, 2436–2445.

[12] Q. Zhong, J. R. Dahn, K. Colbow, *Phys. Rev. B* **1992**, *46*, 2554–2560.

[13] H. Höchst, R. D. Bringans, H. R. Shanks, *Phys. Rev. B* **1982**, *26*, 1702–1712.

[14] J. Guo, C. Dong, L. Yang, G. Fu, H. Chen, *Mater. Res. Bull.* **2006**, *41*, 655–661.

[15] W. A. Crichton, P. Bouvier, A. Grzechnik, *Mater. Res. Bull.* **2003**, *38*, 289–296.

[16] M. Gerosa, C. E. Bottani, L. Caramella, G. Onida, C. Di Valentin, G. Pacchioni, *Phys. Rev. B* **2015**, *91*, 155201.

[17] M. B. Johansson, G. Baldissera, I. Valyukh, C. Persson, H. Arwin, G. A. Niklasson, L. Österlund, *J. Phys. Condens. Matter* **2013**, *25*, 205502.

[18] V. A. Jhalani, H.-Y. Chen, M. Palummo, M. Bernardi, *J. Phys. Condens. Matter* **2019**, *32*, 084001.

[19] G. Kresse, J. Furthmüller, *Phys. Rev. B* **1996**, *54*, 11169–11186.

[20] G. Kresse, J. Furthmüller, *Comput. Mater. Sci.* **1996**, *6*, 15–50.

[21] G. Kresse, D. Joubert, *Phys. Rev. B* **1999**, *59*, 1758–1775.

[22] S. Tanisaki, *J. Phys. Soc. Jpn.* **1960**, *15*, 573–581.

[23] R. Diehl, G. Brandt, E. Salje, *Acta Cryst. B* **1978**, *34*, 1105–1111.

[24] M. Shishkin, G. Kresse, *Phys. Rev. B* **2006**, *74*, 035101.

[25] J. Meyer, M. Kröger, S. Hamwi, F. Gnam, T. Riedl, W. Kowalsky, A. Kahn, *Appl. Phys. Lett.* **2010**, *96*, 193302.

[26] L. Weinhardt, M. Blum, M. Bär, C. Heske, B. Cole, B. Marsen, E. L. Miller, *J. Phys. Chem. C* **2008**, *112*, 3078–3082.

[27] J. Kleperis, J. Zubkans, A. R. Lusis in Optical Organic and Semiconductor Inorganic Materials, *Vol. 2968*, (Eds.: E. A. Silinsh, A. Medvids, A. R. Lusis, A. O. Ozols), International Society for Optics and Photonics, SPIE, **1997**, pp. 186–191.

[28] F. Koffyberg, K. Dwight, A. Wold, *Solid State Commun.* **1979**, *30*, 433–437.

[29] E. Salje, *J. Appl. Crystallogr.* **1974**, *7*, 615–617.

[30] E. Salje, S. Rehmann, F. Pobell, D. Morris, K. S. Knight, T. Herrmannsdörfer, M. T. Dove in **1997**.

[31] M. Bokdam, T. Sander, A. Stroppa, S. Picozzi, D. D. Sarma, C. Franchini, G. Kresse, *Sci. Rep.* **2016**, *6*, 28618.

[32] T. Iwai, *J. Phys. Soc. Jpn.* **1960**, *15*, 1596–1600.

[33] D. C. Mattis, J. .-P. Gallinar, *Phys. Rev. Lett.* **1984**, *53*, 1391–1393.

[34] D. F. Blossey, *Phys. Rev. B* **1970**, *2*, 3976–3990.

[35] P. Cudazzo, L. Sponza, C. Giorgetti, L. Reining, F. Sottile, M. Gatti, *Phys. Rev. Lett.* **2016**, *116*, 066803.

[36] B. Zakharchenya, S. Permogorov in Encyclopedia of Condensed Matter Physics, (Eds.: F. Bassani, G. L. Liedl, P. Wyder), Elsevier, Oxford, **2005**, pp. 171–179.

[37] K. E. O'Hara, L. Ó Súilleabháin, J. P. Wolfe, *Phys. Rev. B* **1999**, *60*, 10565–10568.

[38] D. Hulin, A. Mysyrowicz, C. B. à la Guillaume, *Phys. Rev. Lett.* **1980**, *45*, 1970–1973.

[39] M. Palummo, M. Bernardi, J. C. Grossman, *Nano Lett.* **2015**, *15*, 2794–2800.

[40] C. D. Spataru, S. Ismail-Beigi, R. B. Capaz, S. G. Louie, *Phys. Rev. Lett.* **2005**, *95*, 247402.

[41] K. Galkowski, A. Mitioglu, A. Miyata, P. Plochocka, O. Portugall, G. E. Eperon, J. T.-W. Wang, T. Stergiopoulos, S. D. Stranks, H. J. Snaith, R. J. Nicholas, *Energy Environ. Sci.* **2016**, *9*, 962–970.

[42] R. F. Egerton, *Rep. Prog. Phys.* **2008**, *72*, 016502.

Concluding remarks and Perspectives

In this thesis we have addressed the computational modeling of photoactive materials employed in solar energy devices, namely dyes, semiconductors and dye/semiconductor interfaces. The leitmotiv of our investigations was the study of the Ground and Excited State properties of these systems making use of as accurate as possible electronic structure methods combined with molecular dynamics to account for finite temperature and solvation effects. The results presented here nicely demonstrate that the development in computer hardware and algorithms allow to model today large systems in realistic working conditions, making use of accurate computational methods, which, until a few years ago, could only be applied to extremely simple systems.

A detailed overview of the main results achieved during this thesis is reported below:

- Perylene diimide (PDI) aggregates in solution have been investigated by combining Density Functional Theory (DFT) and time-dependent DFT methods with molecular dynamics (MD) simulations. We focused on the description of the dynamical, optical and Excited State properties of PDI aggregates. We have shown that the inclusion of finite temperature effects, even if has a negligible impact on the shape and position of the absorption spectra, is pivotal in dictating the properties of the Excited State manifold of such aggregates. In particular, by using the one-particle transition density matrix (1TDM) analysis computed along the PDI aggregates MD simulation, we have shown that the concerted motion of PDI chunks prevents the formation of largely delocalized Frenkel excitons. Indeed, even in large aggregates (up to seven units) they almost never exceed five PDI units. Although the delocalization of exciton states is not extremely large, we evidenced the presence of dark but low-lying CT Excited States, involving different PDI units, which

can be exploited to optimize charge separation and transport in PDI-based optical devices.

- We have addressed the calculation of the PDI monomer electronic spectrum in solution by taking into account of both dynamical and vibronic effects. In this regard, the MD simulations have been performed making use of a specifically parameterized Quantum-Mechanically Derived Force Field (QMD-FF), while the optical spectra have been simulated by using a Mixed Quantum-Classical (MQC) approach based on an adiabatic separation of soft(CL)/stiff(QM) nuclear degrees of freedom. Regarding PDI, the torsions pertaining to the flexible lateral chains have been handled classically, while all remaining degrees of freedom have been handled at QM level. Firstly, we have validated the QMD-FF through a benchmark of the MD trajectories against those carried out through ab initio molecular dynamics (AIMD), and we have also shown that GAFF is inadequate to accurately describe the PDI conformational space. Secondly, we have calculated the MQC spectra, considering different solvent models, and we have shown that to have a better agreement with the experimental spectra (with an error of less than 0.1 eV) one should include the effect of the mutual solute/solvent polarization by explicitly considering the first solvation shell. Finally, by comparing the MQC spectra with full QM static vibronic spectra we have shown that treating the soft modes of the lateral chains classically induces a limited broadening, which, however, improves agreement with experimental spectra.

- Employing ab initio molecular dynamics (AIMD) and GW calculations, we have studied a dye-sensitized NiO interface (C343@NiO(100)). We have shown that GW calculations, which accurately describe the spatial dependence of correlation effects, predicted a different interfacial energy level alignment than the one predicted from DFT-based calculations. Also, explicitly accounting for solvent polarization and dynamical effects, we were able to obtain a quantitative agreement with the experimental estimated driving force for the C343@NiO interface. Although we have dealt with a specific system, our results are of a more general relevance. Indeed, we have shown the feasibility of accurate large scale GW calculations on simplified, albeit

realistic models, of dye-sensitized metal oxide interfaces by including solvent molecules and finite temperature effects.

- We have studied the electronic and optical properties of WO_3 considering the room temperature monoclinic, the triclinic, and the simple cubic phases at MBPT level. We have shown that, in agreement with previous studies, the crystal lattice distortions present in the monoclinic and the triclinic phases promote a gap opening of both the fundamental and the optical gap. These distortions have also been shown to be responsible for the increase of the exciton binding energy. Then, from the BSE and the RPA eigenvectors we have analyzed the nature of excitons and we have shown that these are, for all the considered WO_3 phases, delocalized in the reciprocal space along the directions where the band structure is rather flat. Finally, for the room temperature monoclinic phase we have also calculated the exciton band dispersion and the exciton effective mass, which have revealed a marked anisotropic character.

This thesis has been fruitful in terms of both collaborations and results attained, even though it is important to underline that all the projects discussed in the manuscript are still ongoing or undergoing further development.

Regarding the PDI project, we are currently working on simulating the self-assembly mechanism through classical MD simulations. Indeed, the optical and dynamical properties of PDI aggregates, which have been discussed in Section 2, concern aggregates that have been simulated by starting from optimized structures. Therefore, the self-assembly process, experimentally observed, has not been addressed yet.

The evident interest of this project is describing the PDI self-assembly mechanism, unraveling the role played by the substituent groups and by the solvent molecules. For this purpose, we will make use of the above-mentioned QMD-FF, which we expect could reliably describe the PDI self-aggregation, given the accuracy shown for the monomer case.

Parallel to the investigation on self-assembled aggregates, we will model the vibronic spectra of PDI aggregates of different sizes. At variance with the monomer case, the calculation of vibronic spectra of PDI aggregates requires to account for

intermolecular vibronic effects and for couplings between quasidegenerate Excited States. The latter will be computed through quantum dynamics calculations based on the wavepacket propagations on the coupled potential surfaces (PESs). This method relies on the use of diabatic states that we are going to define.

The ambitious end of this project is to merge the MD description of self-assembled aggregates with the accurate computation of vibronic spectra and quantum dynamics calculations, and this requires the development of a MQC-like method. With this approach, we will be able to describe the role of thermal fluctuations, introduced by dynamics, on the population of CT states, which promote the separation of the electron-hole pair, and on the shape of the vibronic spectra of large self-assembled aggregates.

Finally, our intent is also to study PDI aggregates adsorbed on SCs surface (e.g. WO_3) in order to have a physical insight into the working mechanism at the basis of PDI-based photoelectrodes.

Concerning the study of the dye-sensitized NiO interface, we are planning to use a machine learning-based approach in order to have a more quantitative and cheaper approach to the estimation of the interfacial energetics. In details, once the machine learning model has been trained on the interfacial energetics calculated at the GW level on a limited number of snapshots, it will be able to reproduce a GW-like interfacial energetics over the whole MD simulation at a negligible computational cost. A similar approach will also be applied to the calculation of the bulk water potential, which usually requires a huge number of snapshots to converge. An accurate evaluation of the bulk water potential is essential to get an absolute reference against which to refer the C343@NiO interface energy levels, and therefore, to evaluate the solvent effects on the electronic properties of the components of the interfacial system. With such an approach, we will move from the "simple" interface in water solution to more realistic and complicated interfaces, such as interfaces immersed in different electrolytic solutions or including doping species or point defects in the NiO substrate. As far as the study of interfaces in electrolytic solutions is concerned, we are currently modeling, through AIMD simulation, the C343@NiO interface in the presence of the LiF electrolytic specie. Following experimental evidence, Li^+, that has a tetrahedral solvation shell, was inserted close to the anchoring group of the Dye and adsorbed on the NiO surface.

The preliminary conformational analysis of a 20 ps MD trajectory revealed that C343 is destabilized by the presence of the Li^+ on the NiO surface. In particular, one of the two bonds between the C343 and the Ni atoms of the NiO slab undergoes a sizeable elongation after 5 ps. To date, what remains is to assess how the electrical double layer, introduced by the LiF electrolyte, influences the alignment and the position of the energy levels of the C343@NiO system.

Finally, as stated in Chapter 4, the results on various WO_3 phases presented in this thesis represent our preliminary results of an ambitious project that aims at disclose the role of the crystal lattice distortions on the exciton lifetime. For the latter, we are developing an analytical model able to take into account the anisotropic charachter of the exciton effective mass as for the room-temperature monoclinic phase of WO_3. Furthermore, we will support this computational and theoretical study with experimental investigations to validate our predictions on the exciton properties, and therefore validate our exciton model. The choice to apply this model on WO_3 systems derives from the fact that the energy gap of WO_3 is very sensitive to crystal lattice distortions, as shown in this thesis, and we expect these difference will also reflect on the exciton properties. Evidently, this computational protocol is very general and therefore, once validated, it can be used to model the optical properties of any photoactive bulk material.

Appendix A
QMD-FF

A.1 Force-Fields

The total FF energy of a solvated molecule (E_{FF}^{tot}) can be expressed as a sum of an intra-molecular term, E_{FF}^{intra} and an inter-molecular term, E_{FF}^{inter}:

$$E_{FF}^{tot} = E_{FF}^{intra} + E_{FF}^{inter} \tag{A.1}$$

In turn, these two contributions can be further partitioned taking into account the solute-solvent nature of the solvated PDI system:

$$E_{FF}^{intra} = E_{PDI}^{intra} + \sum_{k=1}^{N_{solv}} [E_{solv}^{intra}]_k \tag{A.2}$$

and

$$E_{FF}^{inter} = \sum_{i=1}^{N_{at}^{PDI}} \sum_{i=j}^{N_{at}^{solv}} E_{ij}^{PDI-solv} + \sum_{i=1}^{N_{at}^{solv}} \sum_{j=1}^{N_{at}^{solv}} E_{ij}^{solv-solv} \tag{A.3}$$

where N_{solv} is the total number of solvent molecules, N_{at}^{PDI} is the number of atoms of the PDI solute and N_{at}^{solv} the number of atoms of the considered solvent molecules. The FF terms E_{PDI}^{intra} and $[E_{solv}^{intra}]_k$ are the FF terms ruling the internal dynamics of the PDI solute and the k^{th} solvent molecule, whereas $E_{ij}^{PDI-solv}$ and $E_{ij}^{solv-solv}$ respectively govern the interaction between PDI and the k^{th} solvent molecule or between the i^{th} and j^{th} solvent molecules. It is important to stress that the FF energy partitions reported above allow for the separate parameterization of each term. Consequently, any choice made for the inter-molecular parameters or the intra-molecular description of the solvent does not influence the parameterization of the PDI intra-molecular part described below.

Inter-molecular terms The pairwise intermolecular FF terms E_{ij}^{X} ($X = PDI-solv$ or $solv-solv$), appearing in equation A.3, take the standard expression

$$E_{ij}^{X} = \left(4\epsilon_{ij}^{X} \left[\left(\frac{\sigma_{ij}^{X}}{r_{ij}} \right)^{12} - \left(\frac{\sigma_{ij}^{X}}{r_{ij}} \right)^{6} \right] \right) + \left(\frac{[q_i q_j]}{r_{ij}} \right) \tag{A.4}$$

where the first term in square brackets on the right side is the standard 12-6 Lennard-Jones (LJ) potential, while the second accounts for the Coulomb charge-charge interaction.

Intra-molecular terms Both E_{PDI}^{intra} and E_{solv}^{intra} contributions to E_{FF}^{intra} entering equation A.2 can be further partitioned in several contributions, namely

$$E_{X}^{intra} = E_s + E_b + E_{st} + E_{ft} + E_{nb} \ ; \ X = PDI, solv \tag{A.5}$$

The first three terms refer to stiff Internal Coordinates (ICs), in particular, to the stretching, the bending and stiff torsions, respectively. These terms can be approximated through harmonic potentials, *i.e.*

$$E_s = \frac{1}{2} \sum_{s}^{N_s} k_s (r - r^0)^2 \ ; \ E_b = \frac{1}{2} \sum_{b}^{N_b} k_b (\theta - \theta^0)^2 \ ; \ E_{st} = \frac{1}{2} \sum_{st}^{N_{st}} k_{st} (\phi - \phi^0)^2 \tag{A.6}$$

The fourth term of equation A.5 is instead employed for flexible ICs, which are expected to experience larger distortion during simulation, as for instance the PDI dihedrals or the CH_3 rotation in ACN solvent. Concretely, the E_{ft} term reads

$$E_{ft} = \sum_{\mu}^{N_{ft}} \sum_{j}^{N_{cos_\mu}} k_{j\mu}^{ft} \big[1 + cos(n_j^\mu \delta_\mu - \gamma_j^\mu) \big] \tag{A.7}$$

where δ_μ is the μ-th flexible coordinate, $k_{j\mu}^{st}$ its force constant, n_j^μ the multiplicity and γ_j^μ a proper phase. Finally E_{nb}, the last term of equation A.5, accounts for all non-bonded contributions between interacting atom pairs (N_{pairs}) within the

same molecule, and takes an expression similar to equation A.4, i.e.

$$E_{nb} = \sum_{i=1}^{N_{pairs}} \sum_{j=1}^{N_{pairs}} E_{ij}^{intra} \tag{A.8}$$

where

$$E_{ij}^{intra} = \left(4\epsilon_{ij}^{intra} \left[\left(\frac{\sigma_{ij}^{intra}}{r_{ij}} \right)^{12} - \left(\frac{\sigma_{ij}^{intra}}{r_{ij}} \right)^{6} \right] \right) + \left(\frac{[q_i q_j]}{r_{ij}} \right) \tag{A.9}$$

A.2 JOYCE parameterization

The parameterization of E_{PDI}^{intra} has been carried out with the JOYCE code, using the DFT data, i.e. equilibrium geometry and its Hessian matrix, relaxed torsional energy scan along the selected chain dihedrals, displayed in Figure 2.16.

The details of the JOYCE procedure are outlined in following:

- Specific atom types are assigned to all PDIs atom, as detailed in Figure A.1.

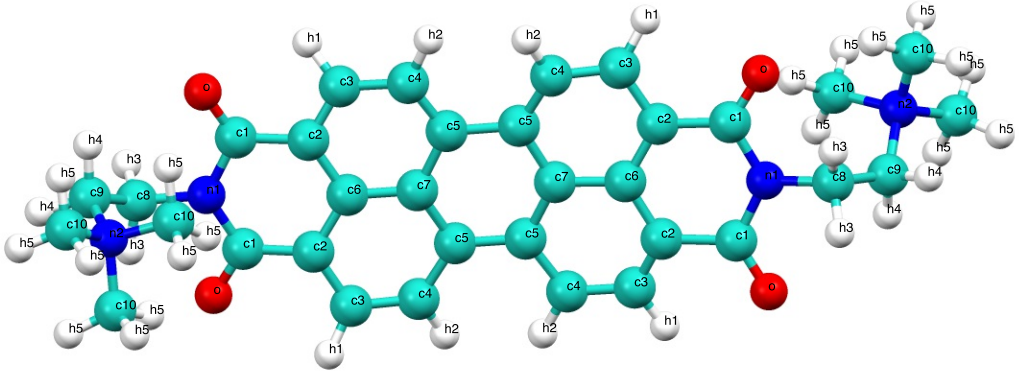

Figure A.1: JOYCE atom types defined for PDI

- As far as the employed ICs are concerned, all possible stretching and bending coordinates were included in the MM description. Moreover, several stiff dihedrals defined by quadruplets of heavy atoms were included in the FF, as the one ruling the planarity of the aromatic core or the out-of-plane vibration of the cores substituents. The more flexible dihedrals (δ_1, δ_2 and δ_3 in Figure 2.16), defined through one quadruplet of connected atoms, are also included in the IC collection, for each of the two lateral pendants. Finally, non-bonded interactions are added for selected atom-pairs, as specified in the following.

- A model potential function is assigned to each IC, following the standard JOYCE criteria: harmonic potentials are employed for all ICs, but the flexible dihedrals, for which the Fourier-like sums reported in equation A.7 are employed, and non-bonded distances described through equation A.8. It might be worth noticing that while the stretching and bending harmonic contributions E_s and E_b, are widely used by popular FFs, the third expression (E_{st}) in equation A.6 is seldom employed for describing torsions of stiff dihedral angles in standard approaches. Yet, it appears to be better suited to account for the internal energy due to small and fast distortions of a dihedral ϕ from its equilibrium position ϕ_i^0, and the JOYCE procedure routinely employs the E_{st} term to mimic the behavior of such stiff dihedrals. Finally, as far as the non bonded intramolecular terms are concerned, it is also important to mention that the flexibility of the JOYCE procedure admits different LJ and charge parameters for either the inter- and intra-molecular terms, thus allowing for the introduction of such interactions only between selected atom pairs, and only through the LJ terms of equation A.9.

- Some additional constraints, other than those dictated by chemical equivalence or symmetry, were imposed on the FF parameter sets, to get rid of numerical fitting inaccuracies introduced by the redundant IC set.

- Finally, All intra-molecular PDI's parameters were obtained with the JOYCE code [1–3] by minimizing the JOYCE objective function I:

$$I^{intra} = \sum_{g}^{N_{geom}} W_g \left[[\Delta U - E^{intra}_{PDI}]_g \right]^2 + \sum_{K \leq L}^{3N-6} W'_{KL} \left[H_{KL} - \left(\frac{\partial^2 E^{intra}_{PDI}}{\partial Q_K \partial Q_L} \right) \right]^2_{g=0} \tag{A.10}$$

where W_g and W'_{KL} terms are the user defined weights, the first sum runs over the PDI g conformations considered in the QM relaxed scans, and ΔU is the QM internal energy. The second sum runs over the QM normal modes, where H_{KL} is the QM Hessian matrix evaluated at the equilibrium geometry ($g = 0$), while Q_K is the K^{th} normal coordinate.

A two-step procedure was adopted: a first JOYCE cycle which fits all harmonic parameters at once and a second cycle, in which the harmonic parameters are fixed according to the Frozen Internal Rotation Approximation, and the parameters for the flexible dihedral are parameterized against the QM torsional relaxed energy scans (Figure 2.16).

Bibliography

[1] I. Cacelli, G. Prampolini, *J. Chem. Theory Comput.* **2007**, *3*, 1803–1817.

[2] V. Barone, I. Cacelli, N. De Mitri, D. Licari, S. Monti, G. Prampolini, *Phys. Chem. Chem. Phys.* **2013**, *15*, 3736–51.

[3] J. Cerezo, G. Prampolini, I. Cacelli, *Theor. Chem. Acc.* **2018**, *137*, 80.

Résumé détaillé sur la Thèse

L'objectif de cette thèse de doctorat était la modélisation computationnelle des matériaux et des systèmes moléculaires utilisés dans les bien-connu cellules solaires à colorant (DSSCs) et les cellules photoélectrosynthétiques à colorant (DSPECs) pour effectuer la réaction de division de l'eau. La caractère hybride organique-inorganique des DSSCs et des DSPECs nécessite l'utilisation de méthodes de physique du état solide et de chimie computationnelle pour leur modélisation. En particulier, dans cette thèse, nous avons étudié les éléments composant ces dispositifs,à savoir les colorants, les semi-conducteurs et les interfaces colorants/semi-conducteurs en accordant une attention particulière à la modélisation de la structure électronique, des propriétés optique et les effets de solvatation et dynamiques introduits par les fluctuations thermiques. La complexité des systèmes et des processus physiques impliqués nécessite la combinaison de différentes méthodologies théoriques, comme détaillé ci-dessous.

Concernant les colorants, nous avons étudié un diimide de pérylène (PDI), largement utilisés comme chromophores grâce à leur remarquable stabilité chimique, thermique et photochimique, une absorption optique large et intense du visible à la fenêtre spectrale proche infrarouge et d'excellentes propriétés de transport de charge (Figure A.1). De plus, les pérylènes sont capables de former spontanément des agrégats H ordonnés qui, par rapport au monomère, présentent un changement dans la structure vibronique du spectre d'absorption et un maximum d'absorption décalé vers le bleu. L'agrégation du colorant sur la surface de l'oxyde métallique est cependant généralement considérée comme étant responsable de faibles rendements et est ainsi empêchée par l'utilisation de coadsorbants antiagrégation. Au contraire, certains exemples d'effets d'agrégation bénéfiques ont été rapportés, y compris des agrégats à base de pérylène-diimides (PDI), qui ont été exploités avec succès comme matériaux photoactifs dans des photoanodes sensibilisés aux colorants pour l'oxydation de l'eau. En particulier, la sensibilisation de surface par des agrégats de PDI hydrophobes, adsorbés en surface par des interactions électrostatiques et de dispersion, ne déclenche pas le clivage hydrolytique

généralement observé pour les groupements d'ancrage classiques (carboxyliques ou phosphoniques).

L'étude des pérylènes en solution a été menée en combinant des méthodes basées sur la théorie de la fonctionnelle de la densité et des simulations de dynamique moléculaire (MD) classiques. Dans la première partie de notre étude, nous avons analysé les propriétés dynamiques et optiques des agrégats PDI, en examinant de près le rôle joué par les fluctuations thermiques et la taille de l'agrégat sur les propriétés de l'état excité. Nous avons démontré la capacité des agrégats PDI H à donner naissance à des fonctions d'ondes excitoniques délocalisées. Les effets du mouvement thermique sur la forme et la position du spectre d'absorption sont cependant négligeables, à la fois dans le cas du monomère et des agrégats. Même s'il n'est pas évident dans les propriétés optiques, l'effet du mouvement thermique est crucial pour dicter les propriétés globales de la variété à état excité de l'agrégat. En particulier, le mouvement particulier à grande échelle observé dans l'agrégat MD et caractérisé par le concerté et la rotation simultanée de morceaux de la colonne PDI empêche la formation d'excitons fortement délocalisés. En fait, même dans le cas d'hélices plus longues, la délocalisation de l'exciton ne dépasse presque jamais cinq unités PDI, confirmant des observations expérimentales récentes. Même si la délocalisation de l'état d'exciton de Frenkel n'est cependant pas extrêmement importante par rapport à des matériaux similaires à auto-agrégat, on devrait mettent en évidence la présence d'états excités CT sombres mais de faible énergie conduisant à la séparation des électron-trou complète entre deux unités qui, par conséquent, peut être efficacement exploitée pour optimiser la séparation et le transport de charge dans les dispositifs optiques à base de PDI.

Suite à l'étude sur les agrégats nous affinons la description classique de l'espace conformationnel PDI, et donc des simulations MD, par la paramétrisation d'un champ de force dérivé de la mécanique quantique (QMD-FF) spécifique au PDI. Nous abordons également le calcul des spectres vibroniques de la molécule PDI en adoptant une approche mixte quantique-classique (MQC) basée sur une séparation adiabatique des degrés de liberté nucléaires souples (CL) / rigides (QM). Dans l'approche MQC, le spectre est obtenu comme une moyenne conformationnelle (sur les coordonnées souples) des spectres vibroniques (pour les coordonnées rigides) qui sont obtenus par l'approche vibronique de Hessian verticale généralisée (gVH).

En particulier, la moyenne a été effectuée sur des instantanés extraits de tests classiques de dynamique moléculaire (MD), réalisés avec le QMD-FF mentionné ci-dessus.

Dans un premier temps, nous avons validé le QMD-FF à travers un benchmark des trajectoires MD par rapport à celles réalisées en dynamique moléculaire ab initio (AIMD), et nous avons également montré que GAFF est insuffisant pour décrire avec précision l'espace conformationnel PDI. Deuxièmement, nous avons calculé les spectres MQC, en considérant différents modèles de solvants, et nous avons montré que pour avoir un meilleur accord avec les spectres expérimentaux (avec une erreur inférieure à 0.1 eV), il faut inclure l'effet de la polarisation mutuelle soluté/solvant en considérant explicitement la première coquille de solvatation. Enfin, en comparant les spectres MQC avec les spectres vibroniques statiques QM complets, nous avons montré que le traitement des modes souples des chaînes latérales induit classiquement un élargissement limité, ce qui améliore cependant l'accord avec les spectres expérimentaux.

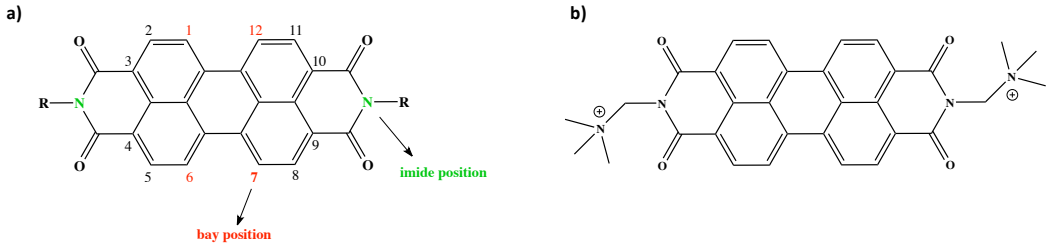

Figure A.1: a) Structure chimique d'un sensibilisateur générique PDI: les positions de la baie et de l'imide sont indiquées respectivement en rouge et en vert. b) Molécule de bis-imide PDI d'acide N,N′-bis(2-(triméthylammonium)-éthylène) -pérylène-3,4,9,10 tétracarboxylique étudiée dans cette thèse.

Concernant l'étude sur les semi-conducteurs, nous décrivons, en considérant différentes phases cristallines, le rôle des distorsions du réseau cristallin sur les propriétés optique et électronique de WO_3. Le WO_3 est un matériau prometteur pour les DSSCs et DSPECs où il pourrait être utilisé comme SC de type n à la place du bien connu Titania (TiO2) car il présente une stabilité contre la photo-corrosion dans les solutions basiques et acides, une photosensibilité élevée et des propriétés de transport d'électrons remarquables. En effet, le WO_3 a un entrefer optique

d'environ 2.6 eV, inférieur à celui du TiO2 (environ 3.2 eV), permettant ainsi une absorption modérée de la lumière visible. Cependant, la bande interdite WO_3 reste trop grande pour une absorption efficace de l'énergie solaire et de nombreuses études visant à réduire son écart ont été signalées. En particulier, le gap optique s'est révélé très sensible à la distorsion de la structure cristalline, favorisée par l'intercalation d'espèces dopantes ou par des modifications structurelles.

En général, les distorsions du réseau cristallin doivent être considérées comme préjudiciables, car elles élargissent la bande interdite par rapport à celle prédite pour les phases hautement symétriques de WO_3. Cependant, le ces derniers, sont instables dans des conditions standard. Par conséquent, une compréhension approfondie des effets des distorsions du réseau cristallin sur les propriétés optoélectroniques de WO_3 pourrait donner des directives claires pour effectuer une distorsion ciblée visant à produire des systèmes WO_3 stables et optimisés.

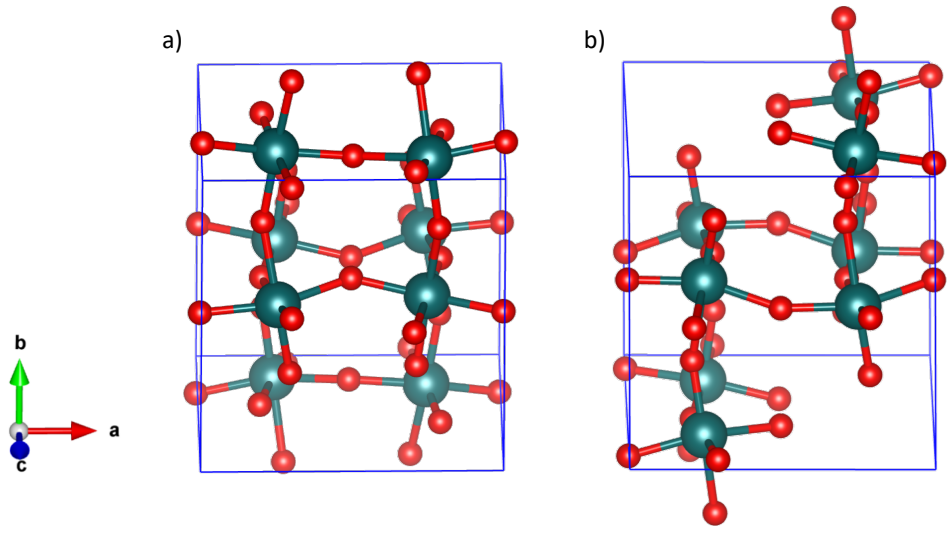

Figure A.2: Structure cristalline relâchée a niveau LDA de la γ monoclinique phase (à gauche) et la phase triclinique (à droite) de WO_3

Dans cette thèse, nous rapportons des calculs ab initio au niveau MBPT du gap fondamental, de la structure de bande et des propriétés optiques de WO3 compte

tenu de sa phase cubique simple et des deux phases les plus stables, à savoir la phase monoclinique à température ambiante et la phase triclinique (Figure A.2). Nous avons montré que, en accord avec les études précédentes, les distorsions du réseau cristallin présentes dans les phases monoclinique et triclinique favorisent une ouverture à la fois de l'intervalle fondamental et optique. Ces distorsions se sont également révélées responsables de l'augmentation de l'énergie de liaison à l'exciton. Ensuite, à partir des vecteurs propres BSE et RPA, nous avons analysé la nature des excitons et nous avons montré que ceux-ci sont, pour toutes les phases WO3 considérées, délocalisées dans l'espace réciproque selon les directions où la structure de bande est plutôt plate. Ensuite, pour la phase monoclinique à température ambiante, nous avons également calculé la dispersion de la bande d'exciton et la masse efficace de l'exciton, qui ont révélé un caractère anisotrope marqué.

Enfin, nous avons étudié un modèle simplifié, quoique réaliste, d'un DSSC de type p, considérant une interface NiO sensibilisée aux colorants.

Les DSSCs de type p offrent la possibilité de convertir directement la lumière du soleil en énergie électrique à faible coût. Cependant, ces dispositifs ont des rendements de conversion de puissance plutôt médiocres (2,5%) par rapport aux DSSCs de type n ($\sim$ 14%) pour des raisons qui ne sont pas encore élucidées (injection de trous lents, voies de recombinaison à retour rapide). Les DSSCs de type p sont basés sur l'injection de trous du HOMO du colorant photoexcité (par exemple C343) dans la bande de valence d'un semi-conducteur (par exemple NiO) et la force motrice (la différence entre l'énergie VB et l'énergie HOMO) a un rôle clé dans l'efficacité globale des DSSCs. En ce qui concerne le NiO sensibilisé aux colorants, relativement peu de travaux de calcul, basés sur des calculs DFT, ont été rapportés. Un résultat commun de ces études est que l'énergétique interfaciale, dictant la force motrice pour l'injection de trous du colorant au NiO VB, s'avère extrêmement sensible au mode d'ancrage du colorant et aux effets de solvatation. Dans ce cadre, nous réalisons une caractérisation théorique de la surface NiO sensibilisée au C343 dans l'eau (Figure A.3), en combinant des simulations de dynamique moléculaire (MD) ab-initio avec des calculs de GW le long de la trajectoire MD, pour décrire de manière fiable la structure et l'énergétique de l'interface lorsque les effets de solvatation explicite et de température finie sont

pris en compte.

Nous avons montré que les calculs de GW, qui décrivent avec précision la dépendance spatiale des effets de corrélation, prédisaient un alignement du niveau d'énergie interfacial différent de celui prédit à partir des calculs basés sur la DFT. De plus, en prenant explicitement en compte la polarisation du solvant et les effets dynamiques, nous avons pu obtenir un accord quantitatif avec le force motrice expérimental estimé pour l'interface C343@NiO. Bien que nous ayons traité d'un système spécifique, nos résultats sont d'une pertinence plus générale. En effet, nous avons montré la faisabilité de calculs précis de GW à grande échelle sur des interfaces métal-oxyde sensibilisées par colorant simplifiées en incluant des molécules

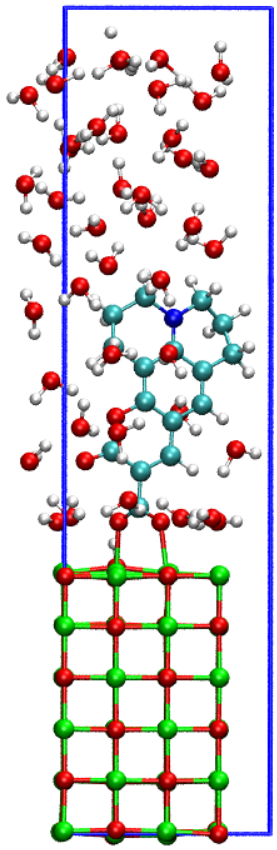

Figure A.3: La géométrie du système C343 @ NiO complet en solution aqueuse explicite

de solvant et des effets de température finis.